1. INTRODUCTION 1

1.1 The Greenhouse Effect and Global Warming 1
1.1.1 Historical Background 2
1.1.2 Greenhouse Gases 2
1.1.3 Ways to Reduce Anthropogenic CO_2 Emissions 6
1.2 Sequestration of CO_2 6
1.2.1 CO_2 Storage Options 7
1.2.2 CO_2 Transportation 8
1.2.3 CO_2 Capture Processes 8
1.2.4 Cost of CO_2 Sequestration 10

2. CHEMICAL-LOOPING COMBUSTION 11

2.1 Process Studies 13
2.2 Chemical-Looping Combustion of Solid Fuels 14
2.3 Oxygen Carriers 14
2.3.1 Thermal Aspects 15
2.3.2 Fate of Sulphur Species 20
2.3.3 Selection of Oxygen Carriers for this Work 22
2.4 Carbon Formation 25
2.5 Objective 26

3. EXPERIMENTAL 29

3.1 Preparation of Oxygen Carriers 29
3.1.1 Freeze-Granulation 30
3.1.2 Spray-Drying 32
3.1.3 Unprocessed Materials 33
3.2 Characterization of Oxygen Carriers 34
3.3 Reactivity Investigation of Oxygen Carriers 35

4. RESULTS 45

4.1 Characterization of Oxygen Carriers 45
4.1.1 Effect of Sintering Temperature 46
4.1.2 Effect of Sintering Time 48
4.2 Reactivity of Oxygen Carriers 49
4.2.1 Ni-Based Particles without Additives 49
4.2.2 Ni-Based Particles with Additives 50
4.2.3 Rate Index 52
4.2.4 Reduction Kinetics with NOV1T1450sd 53
4.2.5 Natural and Synthetic Ilmenites 54
4.2.5 Low-Cost Fe-Based Materials 55
4.3 Effect of Up-Scaling in Particle Production 57
4.4 Defluidization 58
4.5 Carbon Formation 60
4.6 Conversion of Solid Fuels 61

5. DISCUSSION 63

5.1 Ni-Based Oxygen Carriers 63
5.2 Fe-Based Oxygen Carriers 65

6. CONCLUSIONS 69

7. ACKNOWLEDGEMENT 71

8. REFERENCES 73

1

INTRODUCTION

1.1 The Greenhouse Effect and Global Warming

The greenhouse effect is a naturally occurring process by which the Earth's surface and its surrounding atmosphere are heated. It results from the fact that certain atmospheric gases, i.e., greenhouse gases, are able to change the energy balance of the planet.

The Sun is radiating energy at very short wavelengths, predominately in the visible or near-visible part of the energy spectrum. To balance this input of solar radiation, the Earth emits energy back to space. As a result of the relatively low temperature on Earth, the energy emitted is mainly in the long wave infrared part of the energy spectrum. Much of this thermal radiation is absorbed by greenhouse gases in the atmosphere, and is reradiated back to Earth, resulting in the warming of the surface, known as the greenhouse effect.

Without this natural greenhouse effect, the global energy balance would result in an average temperature on Earth of about -18ºC rather than the present average temperature of 15ºC [1]. Figure 1-1 visualizes a simplified energy balance of the Earth's surface.

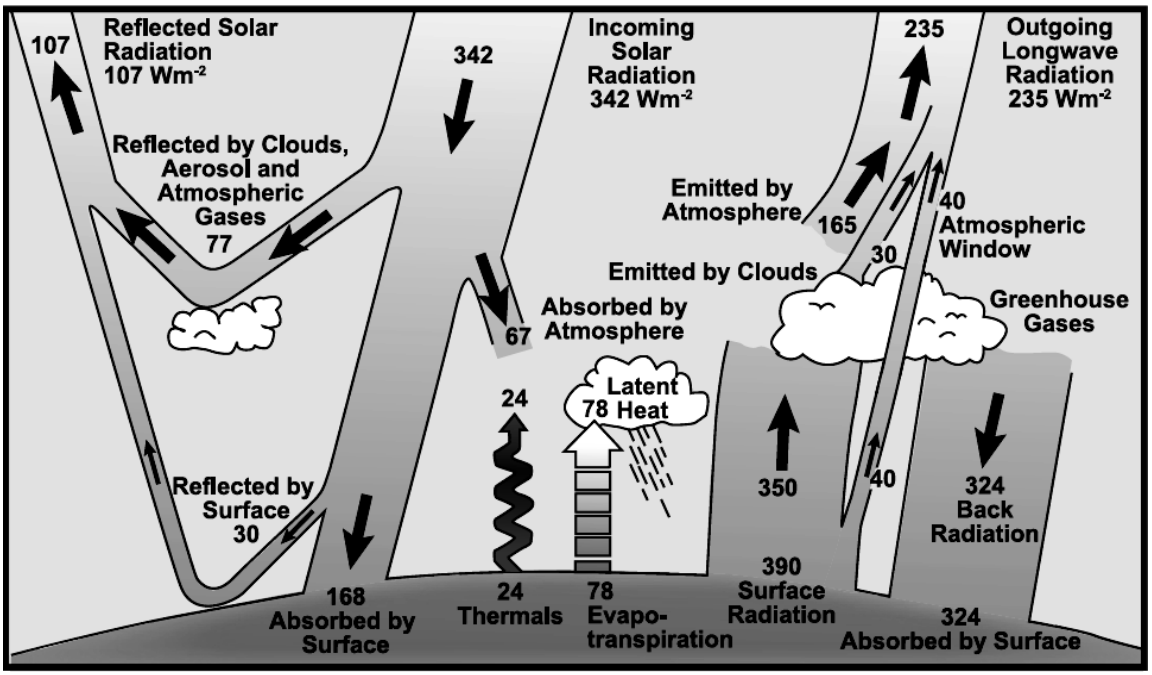

Figure 1-1. The Earth's annual and global mean energy balance [2].

1.1.1 Historical Background

The basic idea of the greenhouse effect was discovered as early as 1681 by the French physicist Edme Marriotte who found that the Sun's light and heat easily passed through glass and other transparent materials while heat from other sources did not [3].

After this discovery it took until 1824 before the French mathematician Joseph Fourier suggested that gases in the atmosphere might absorb heat in a similar way [4]. As Fourier stated, energy in the form of visible light from the Sun easily penetrates the atmosphere to reach the surface and heat it up, but heat cannot so easily escape back into space. Although the equations and data available at that time were far too poor to allow accurate calculations, scientists were able to show that an uncovered, airless rock at the Earth's distance from the Sun should be far colder than the Earth actually was [5].

The British philosopher James Tyndall set out to find whether there was in fact any gas in the atmosphere that could trap the heat released from the Earth. In 1859, his careful laboratory work identified several gases that did just that, the two most important being water vapour and carbon dioxide [6].

In 1896, the Swedish chemist Svante Arrhenius first linked the concentration of CO_2 in the atmosphere to the climate of the Earth [7] and suggested that burning of fossil fuels, and with that release of CO_2, might lead to an increased global temperature. Arrhenius main focus was to understand the cause of the ice ages and he therefore argued in favour of increasing the atmospheric CO_2 concentration, thus avoiding a forthcoming ice age. The German physicist, Walther Nernst, even presented the idea of setting fire to entire coal seams in order to release enough CO_2 to deliberately cause global warming [5].

In later years, concerns about the increasing atmospheric CO_2 concentration, the subsequent global warming and possible effects such as sea level rise and changes in precipitation patterns have increased steadily. The Intergovernmental Panel on Climate Change concludes in their 4^{th} Assessment Report that changes in the atmosphere, the oceans and glaciers and ice caps now show unequivocally that the world is warming due to human activities [8].

1.1.2 Greenhouse Gases

Water vapour (H_2O), is the single most important greenhouse gas, accounting for about 60% of the natural greenhouse effect for clear skies [9]. However, human activities play an insignificant part in influencing the amount of atmospheric water vapour directly. However, indirectly humans have the potential of affecting water vapour concentrations substantially by changing the climate, as a warmer atmosphere would contain more water

vapour. Greenhouse gas concentrations that are directly affected by human activities are the so called anthropogenic greenhouse gases. Human activities result in emissions of four principal greenhouse gases: carbon dioxide (CO_2), methane (CH_4), nitrous oxide (N_2O) and the halocarbons which is a group of hydrocarbon gases containing fluorine, chlorine or bromine. Significant increases in the atmospheric concentrations of all these gases have occurred in the industrial era, at different rates. In 2004, CO_2 represented 77% of the global anthropogenic greenhouse gas emissions [10], when weighted by their global warming potential, and is therefore often given focus of attention when considering how to solve the problem of global warming.

Figure 1-2 displays the atmospheric CO_2 concentration and temperature over the past 420 000 years up until 1950.

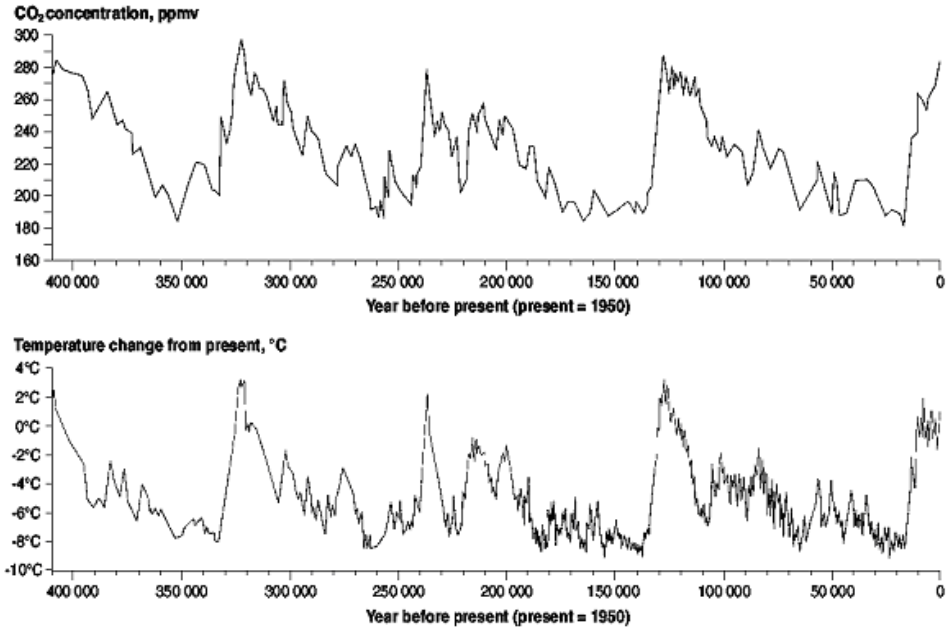

Figure 1-2. Atmospheric CO_2 concentration and temperature change over the last 420 000 years as determined from ice core analysis [11].

From this figure it appears evident that there is a correlation between these two parameters. However, the correlation is complex since the global climate is affected by other parameters beside the atmospheric concentration of greenhouse gases. Examples of such parameters are solar activity, land surface properties and presence of atmospheric aerosols. There are many feedback mechanisms in the climate system that can either intensify or weaken the effects of a change in greenhouse gas concentrations. For example, as rising concentrations of greenhouse gases cause a warming of the Earth's surface, snow and ice begin to melt. This melting exposes land and water surfaces which absorb more of the Sun's heat, causing more warming, which results in further melting, and so on, in a self-reinforcing cycle. Detecting, understanding and quantifying these

feedback systems have been the focus of a great deal of research by scientists exploring the complexity of the Earth's climate [2]. Figure 1-3 displays the changes in contributions to radiative forcing for some of the factors affecting the global energy balance from the start of the industrial era, about 1750, to 2005. As seen, the greenhouse gases, in particular CO_2, have caused the largest change in the global energy balance over this period and the effect of aerosols emitted to the atmosphere comprises the largest uncertainty [12]. Positive forcing leads to warming of the Earth while negative forcing has a cooling effect.

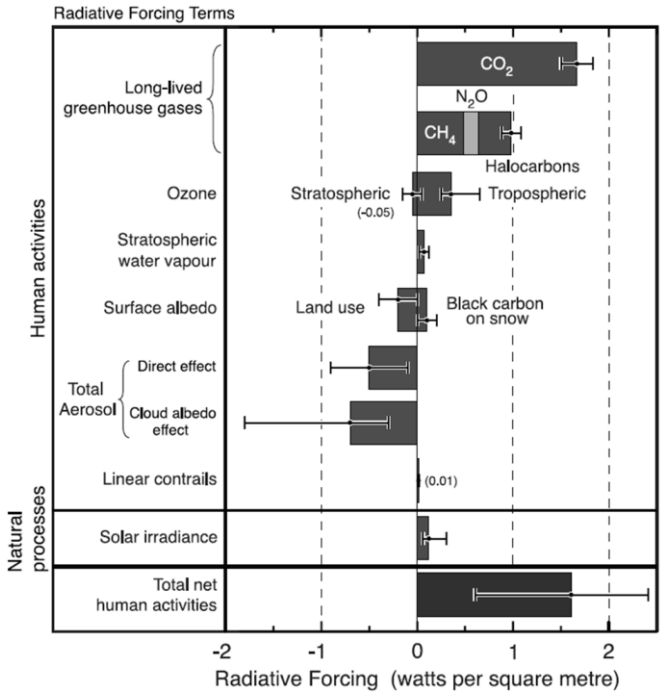

Figure 1-3. Radiative forcing in 2005, relative to 1750. The black line attached to each bar represents the range of uncertainty [12].

A problem with making predictions of the Earth's climate is that scientists are unable to perform controlled experiments on the planet as a whole and then observe the results. However, empirical tests of numerous different hypotheses have built up substantial knowledge in this field. This repeated testing has refined the understanding of the numerous aspects affecting the climate and its inherent feedback systems. The general scientific consensus today is that the ongoing increase in atmospheric CO_2 concentration caused by human activities has a definite and significant effect on the current heating of the Earth.

The global atmospheric concentration of CO_2 has increased from a preindustrial value of about 280 ppm to 379 ppm in 2005 [12], as displayed in Figure 1-4. The current CO_2 concentration exceeds by far the natural values over the last 420 000 years, which has varied between 180 and 300 ppm, and is rapidly increasing.

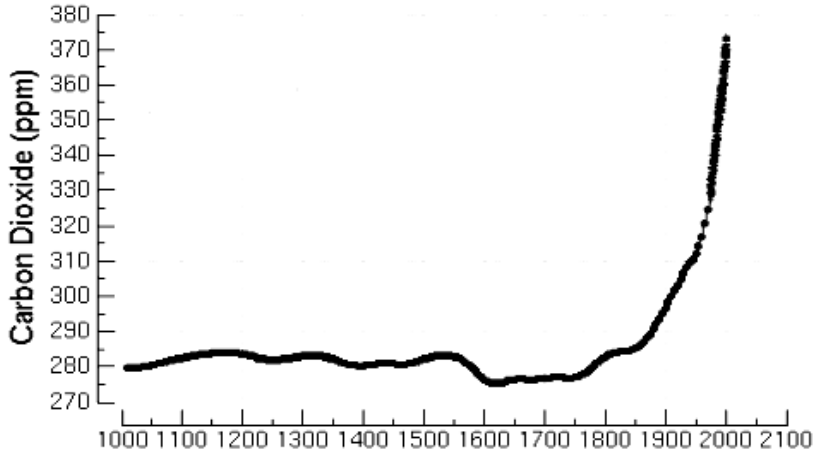

Figure 1-4. Change in atmospheric CO_2 concentration over the last 1000 years. Concentrations from 1958 and onwards are direct measurements from Mauna Loa Observatory, Hawaii. Older data are measured in air bubbles trapped in ice core from Law Dome, Antarctica [13].

The drastic increase in CO_2 concentration is predominantly due to the intensified use of fossil fuels, which in 2004 was the source of 80% of the world's total primary energy supply [14]. Another contributor to the increased CO_2 concentration is deforestation, which releases CO_2 and reduces its uptake by plants. During the past hundred years, 1906-2005, the global average temperature has increased by 0.74±0.18°C [12]. It has been shown that this temperature increase cannot be explained by natural climate variations alone [15]. The increased global mean temperature over the last 150 years is displayed in Figure 1-5.

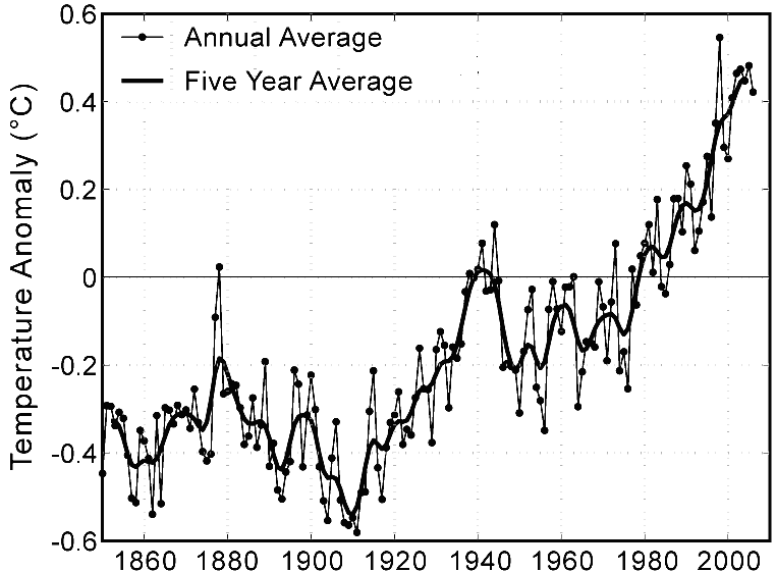

Figure 1-5. The observed change in global mean temperature over the last 150 years. Temperatures are shown as deviation from the 1961 to 1990 average [16].

The anthropogenic climate change is having a significant impact on physical and biological systems globally and temperature related changes in such systems have been observed on all continents from 1970 to 2004 [15].

1.1.3 Ways to Reduce Anthropogenic CO_2 Emissions

There is a wide range of possible ways to reduce emissions of CO_2. The most obvious are reducing the use of energy or implement a transition from carbon intensive fossil fuels to nuclear power or renewable energy sources such as biomass-, hydro-, wind-, or solar power. In addition to this, atmospheric CO_2 can be removed by biomass uptake or by underground carbon sequestration.

The world is presently heavily dependent on the utilization of fossil fuels and known reserves of these, especially coal, are plentiful. Therefore, technological options that will allow for the continued use of fossil fuels without substantial emissions of CO_2 to the atmosphere would be desirable. In this respect, one route forward would be the development and deployment of technologies for capture and storage of the CO_2 produced by combustion of fossil fuels. However, due to the quantities of CO_2 involved, it is likely that a portfolio of measures that include all of the above mentioned options will prove to be necessary in solving the problem of global warming.

1.2 Sequestration of CO_2

Carbon dioxide capture and storage is a process consisting of the separation of CO_2 from an industrial or energy-producing source, transport to a storage location and long-term isolation from the atmosphere. The idea is generally referred to as carbon capture and storage or carbon sequestration and has received an increased interest in recent years [17-20]. Implementation of this process would be feasible on any large stationary point source emitting CO_2. Such sources include large fossil- or biomass fuelled power plants, cement- and steel industries, refineries and natural gas processing facilities and account for about 60% of the global CO_2 emissions [17]. The power production sector itself accounts for about a third of the total CO_2 emissions [21].

The potential contribution of this technology in stabilizing the atmospheric CO_2 concentration will be influenced by factors such as the cost relative to other methods, the possible release of CO_2 stored, the transport infrastructure to storage sites, environmental concerns and the public acceptance of this approach [17].

CO_2 capture and storage from combustion of biomass can yield net removal of CO_2 from the atmosphere, as the CO_2 stored originates from biomass which has absorbed CO_2 from the atmosphere as it grew [22, 23].

1.2.1 CO_2 Storage Options

There are several options for storage of CO_2, e.g., in geologic formations, in deep oceans or by mineral carbonation. At present, geological storage is generally regarded as the preferred alternative. In order to store CO_2 geologically, it must first be compressed to a dense fluid state. Geological storage sites for CO_2 include depleted oil and gas reservoirs, unmineable coal seams and deep saline formations, as presented in Figure 1-6.

Injection of CO_2 into subsurface geological formations has been undertaken since the early 1970s, primarily for the purpose of enhanced oil recovery. In 1996, the world's first large-scale storage project was initiated by Statoil and its partners at the Sleipner gas field in the North Sea, where about 1 Mt CO_2 has been injected annually in the Utsira aquifer [18]. The injected CO_2 is obtained during upgrading of natural gas and stored for environmental reasons.

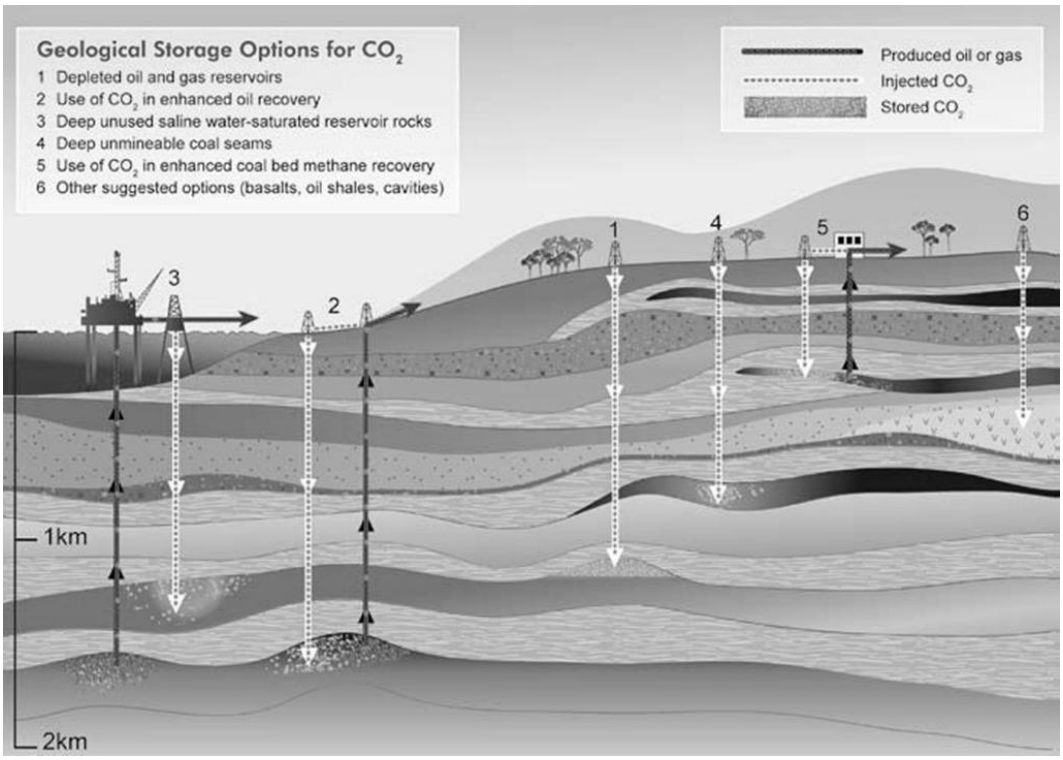

Figure 1-6. Options for storing CO_2 in deep underground geological formations [17].

Apart from geological storage, CO_2 can be injected into oceans at great depth, where most of it would remain isolated from the atmosphere for centuries. This is due to the fact that CO_2 has a higher density than sea water at depths exceeding 3 000 m. Although there have been small-scale field experiments and numerous theoretical-, laboratory-, and modelling studies of ocean storage of CO_2, it has not yet been deployed since local effects on the sea floor environment are inevitable. Potential underground deposit sites for CO_2 are abundant as displayed in Table 1-1.

Table 1-1. The worldwide capacity of potential CO_2 storage reservoirs, orders of magnitude [24].

Sequestration option	*Worldwide capacity [Gt C]*
Ocean	**1 000-10 000+**
Deep saline formations	**100-10 000**
Depleted oil and gas reservoirs	**100-1 000**
Coal seams	**10-1 000**

1 Gt C = 1 billion tonnes of carbon equivalent = 3.7 Gt CO_2.

These values should be compared to the global annual anthropogenic carbon emissions, which are approximately 7 Gt C [24], hence the available storage capacity is huge and should be able to store a large fraction of emitted carbon dioxide.

A third option suggested for storing of CO_2 is mineral carbonation, an industrial imitation of the natural weathering process. Here, gaseous CO_2 is converted into a solid carbonate by reactions with naturally occurring magnesium- or calcium-rich silicates, which are extremely abundant. The products of mineral carbonation reactions are naturally occurring stable solids that would provide storage capacity on a geological time scale [25]. Although these reactions are thermodynamically favoured, they are extremely slow in nature and the process would require huge amounts of minerals. The main challenge associated with mineral carbonation is to speed up the reactions in order to design an economically viable process.

1.2.2 CO_2 Transportation

Transportation of CO_2 from the point of capture to the storage location can be solved by currently existing technologies. Carbon dioxide pipelines already extend over more than 2 500 km in the western USA, where they carry 50 Mt CO_2 annually from natural sources to enhanced oil recovery projects [17].

The infrastructure for natural gas and petroleum gases is well established on a very large scale including transportation in pipelines and marine tankers. Carbon dioxide is currently transported in the same way, but on a smaller scale. The properties of liquefied carbon dioxide are not greatly different from those of liquefied petroleum gases and therefore, the transportation should not involve any major difficulties.

It is generally cheaper to transport CO_2 in pipelines than to transmit electricity. Therefore, it would likely be advantageous to place power stations close to the electricity demand and transport the CO_2 to the storage site [21].

1.2.3 CO_2 Capture Processes

The major part of the flue gas emitted by a power station consists of nitrogen, CO_2 comprise only about 4-14% of the total flue gas volume [21]. The higher value is typical

for a pulverized coal fired power plant and the lower can be expected from a process utilizing natural gas in a combined cycle. Before carbon dioxide can be transported to, and stored at, a suitable location, it has to be obtained in a concentrated stream. Highly concentrated CO_2 is necessary since energy and space requirements for compression, transportation, and storage otherwise would be unbearable.

Most processes for capturing CO_2 from combustion in a power production unit can be divided into three main categories. These are post-combustion, pre-combustion and oxyfuel combustion, as displayed in Figure 1-7. Each of these technologies are associated with an energy, and hence an economic, penalty for separation of gases. A fourth option, where this energy penalty for gas separation is avoided, is chemical-looping combustion which will be comprehensively described in section 2.

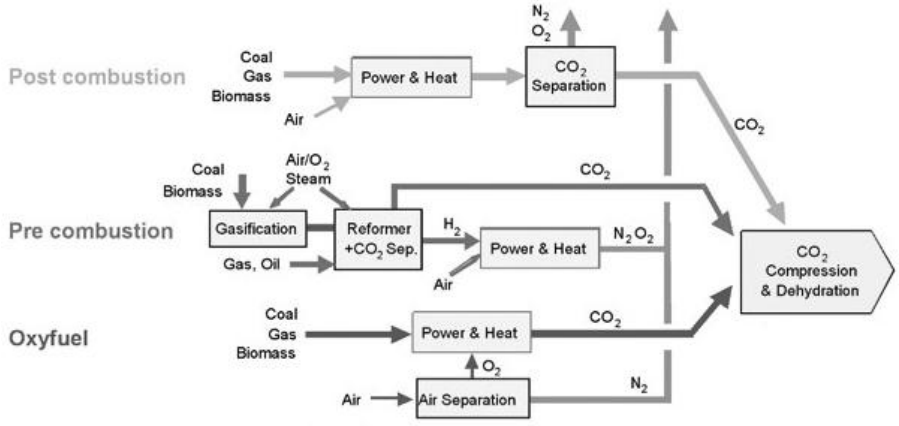

Figure 1-7. Possible CO_2 capture technologies [17].

Post-combustion, or flue gas separation, is accomplished by treating the flue gases in a process which separates most of the CO_2 from the rest of the gases. A chemical sorbent process would normally be used to accomplish this and the main one in use today is scrubbing of the flue gases, using an amine solution [24]. After leaving the scrubber, the amine is heated to release high purity CO_2; whereafter the amine can be reused. In many respects, post-combustion capture of CO_2 is analogous to flue gas desulphurization, which is widely used on coal- and oil fired power stations to reduce emissions of SO_2 [21].

Pre-combustion is a process for manufacturing hydrogen from a fossil fuel. In a first step, the fuel is gasified with oxygen or air and/or steam to give mainly a synthesis gas of carbon monoxide and hydrogen. The carbon monoxide is then reacted with steam in a catalytic reactor, to give CO_2 and more hydrogen. Hereafter, CO_2 is separated, usually by a physical or chemical absorption process, resulting in a hydrogen-rich fuel which can be used in many applications, such as boilers, furnaces, gas turbines, engines and fuel cells [17]. Although pre-combustion capture involves a more radical change to the power

station design than post-combustion, most of the technology is already well proven in ammonia production and other industrial processes [21].

The third option, oxyfuel combustion, is based on a combustion process using pure oxygen instead of air to obtain a flue gas stream containing mostly CO_2 and H_2O, where the water can easily be condensed. A part of the flue gas needs to be recycled into the combustion chamber, in order to control the flame temperature [24]. The energy demanding step in this process is to separate oxygen from nitrogen in the air, prior to combustion. The most efficient technology for producing large quantities of oxygen is cryogenic air separation [26].

For pre- and post-combustion systems the capture efficiency is expected to be 85-95% whereas the capture efficiency in an oxyfuel based power production unit is expected to be very close to 100% [17]. The capture efficiency is defined as the fraction of CO_2 separated from the gas stream. Another advantage with oxyfuel combustion is that NO_x formation is suppressed.

1.2.4 Cost of CO_2 Sequestration

The cost of capturing CO_2 is the largest contributor to the overall cost of CO_2 capture, transportation and storage. The capture cost for a new pulverized coal fired power plant or a natural gas combined cycle power plant, based on current technology, is expected to be in the range of 30-90 US$/t CO_2 avoided [17]. This cost should be compared to the cost of transportation, which is typically 1–8 US$/t CO_2/250 km, and the geological storage cost which is believed to range from 0.6–8.3 US$/t CO_2 [17]. It should be noted that the transportation cost depends strongly on the quantity transported. The storage cost also includes cost of monitoring the storage site and is estimated without potential benefits from enhanced oil or gas production, which can actually yield a negative storage cost. The main determinants of storage costs are reservoir and injection characteristics such as permeability, thickness and reservoir depth [17].

The high capture cost is associated with the highly energy consuming gas separation processes. It would be beneficial if CO_2 could be obtained separated from nitrogen without such a gas separation process. An option to achieve this is by using chemical-looping combustion.

2

Chemical-Looping Combustion

Chemical-looping combustion is a novel combustion technology where fossil fuels can be utilized while CO_2 is separated from the rest of the flue gases, without an energy consuming gas separation process. This is accomplished by performing the combustion in two interconnected reactors, one with a continuous inlet of air and one with a continuous feed of fuel gas. The technology requires an oxygen carrier, generally in the form of metal oxide particles, with the purpose of transferring oxygen from the combustion air to the fuel, as presented in Figure 2-1. Since the combustion is accomplished by a gas-solid reaction between the fuel and the metal oxide, direct contact between fuel and air is avoided and a high-purity CO_2 stream is obtained from the fuel reactor after water vapour condensation. The outlet stream from the air reactor will contain nothing but oxygen depleted air. The oxygen carriers are circulated between the two reactors, constantly providing new oxygen for the combustion process.

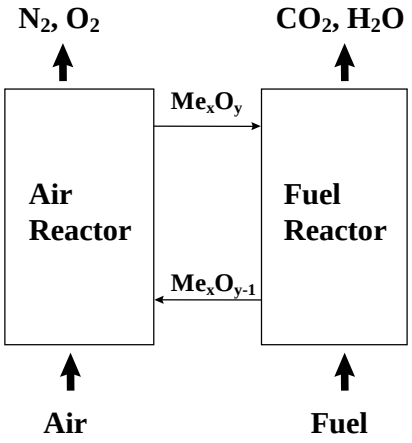

Figure 2-1. Schematic representation of the chemical-looping combustion process.

In the air reactor, the reduced metal oxide, denoted Me_xO_{y-1}, is oxidized by air according to reaction (1) and in the fuel reactor it is reduced back to its initial state by a fuel, according to reaction (2).

$$O_2 + 2Me_xO_{y-1} \leftrightarrow 2Me_xO_y \quad (1)$$

$$C_nH_{2m} + (2n+m)Me_xO_y \leftrightarrow nCO_2 + mH_2O + (2n+m)Me_xO_{y-1} \quad (2)$$

Reaction (1) is strongly exothermic while reaction (2) could be either exothermic or endothermic depending on the fuel used and the characteristics of the oxygen carrier. However, the sum of the energy released in these two reactions is always the same as the heat released in conventional combustion, where the air and the fuel are in direct contact; hence no extra energy is needed in the CO_2 separation process. In addition to this, chemical-looping combustion minimizes formation of NO_x as the fuel conversion occurs in absence of air and the temperature in the air reactor is generally too low to generate any thermal NO_x [27].

The basic ideas of chemical-looping combustion can be found in a patent from 1954 where it is presented as a technique to produce pure CO_2 from fossil fuels [28]. A similar concept was proposed as a power production technique in 1983 by Richter and Knoche [29], with the purpose of increasing the thermal efficiency. In 1994, Ishida and Jin suggested that chemical-looping combustion could be used as a technology to separate CO_2 from the rest of the flue gases in a power plant in order to reduce climate impact [30] and in 2001, Lyngfelt et al. proposed a reactor design of two interconnected fluidized beds for the process as shown in Figure 2-2 [31].

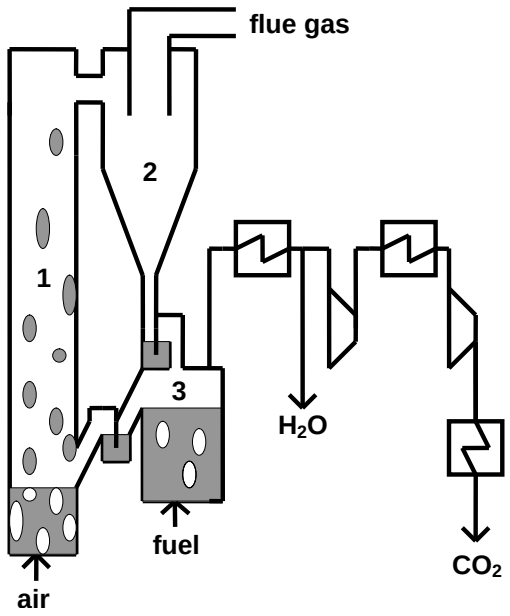

Figure 2-2. Propsed design of chemical-looping combustion. 1) Air reactor and riser, 2) Cyclone and 3) Fuel reactor [31].

The design of a reactor system with two fluidized beds gives the advantage of a good contact between the oxygen carrier and the reacting gas. In this design, the air reactor is a riser where the flow is high enough to entrain the oxygen carriers which are separated from the oxygen-depleted air in a cyclone. Hereafter, the oxygen carriers fall down into the fuel reactor. The fuel reactor could be designed as a bubbling fluidized bed from

where the oxygen carriers are allowed to fall down into the air reactor using for instance an overflow exit. To prevent mixing of the gas streams from the air reactor and the fuel reactor, two loop seals are installed between the reactors. This design has significant similarities to a circulating fluidized bed boiler for solid fuels, thus using well proven technology and components [31].

Fluidization occurs when a bed of solid particles is exposed to an upward moving gas flow exceeding the minimum fluidization velocity, u_{mf}. The minimum fluidization velocity is dependent on both the characteristics of the gas and of the particles and is reached when the drag force from the upward moving gas equals the weight of the bed particles. The terminal velocity, u_t, is reached when the drag force from the ascending gas on a single particle equals the weight of that particle. At gas velocities exceeding the terminal velocity, particles are entrained and carried away from the fluidization vessel [32]. Thus, in the air reactor, a gas velocity exceeding the terminal velocity should be used and in the fuel reactor, assuming a bubbling bed reactor, a gas velocity between the minimum fluidization velocity and the terminal velocity is required.

Although the fuel reactor is generally designed as a bubbling bed in small-scale prototype units, the gas-solids contact is expected to be improved by designing the fuel reactor as a circulating fluidized bed, thus using a gas velocity exceeding the terminal velocity. Kolbitsch et al. have designed and successfully operated a 120 kW_{th} reactor system where both reactors are circulating fluidized beds [33].

2.1 Process Studies

Several simulations, investigating power processes and their thermal efficiencies, using both natural gas and synthesis gas and different oxygen carriers, have been performed. Reviews of these and relating literature can be found in doctoral theses of Anheden [34], Wolf [35], Brandvoll [36] and Naqvi [37].

These theoretic studies indicate that the thermal efficiencies are generally high and the overall efficiencies are higher compared to conventional systems with CO_2 capture. To reach these high efficiencies for gaseous fuels, combined cycle processes involving pressurized fluidized beds should be developed. However, the temperatures used in such combined cycles are higher than those at which oxygen carriers have normally been tested and therefore, further oxygen carrier development is crucial.

2.2 Chemical-Looping Combustion of Solid Fuels

Most research and development of chemical-looping combustion up to date has focused on gaseous fuels. However, as solid fuels like coal are considerably more abundant, less expensive, account for a larger share of global power generation sector and releases more CO_2 per unit of energy produced than natural gas [38], it would be highly advantageous if the chemical-looping combustion process could be adapted to convert solid fuels. This adaptation could be accomplished in three different ways; by introducing the solid fuel directly to the fuel reactor where it is gasified and reacted with the circulating oxygen carrier [39, 40], by introducing synthesis gas, produced in a prior gasification step, to the fuel reactor [41] or by chemical-looping with oxygen uncoupling, CLOU, which is a novel technology using an oxygen carrier which releases gas-phase O_2 in the fuel reactor [42].

When the solid fuel is introduced directly to the fuel reactor, the solid-solid reaction rate between the fuel and the oxygen carrier is inadequate and a gasifying agent, such as H_2O, is generally used [43, 44]. Apart from gasifying the fuel to an intermediate synthesis gas, according to reaction (3), this agent also acts to fluidize the solid material in the fuel reactor.

$$C + H_2O \leftrightarrow CO + H_2 \tag{3}$$

2.3 Oxygen Carriers

One of the keys to successfully implement chemical-looping combustion is the development of suitable oxygen carriers [45]. Some of the most important criteria for the oxygen carriers to be used in a circulating system of interconnected fluidized beds have been identified as:

- High conversion of the fuel to CO_2 and H_2O, i.e., no major thermodynamic constraints
- High reactivity with fuel and oxygen
- Low fragmentation and attrition
- Low tendency for agglomeration
- Low cost
- Low environmental impact

Several transition state metal oxides, primarily based on Ni, Cu, Mn and Fe, have been used as oxygen carriers in chemical-looping combustion since they fulfil the above mentioned criteria to varying extents [46, 47].

To increase the performance of the active oxygen carrier material, it is generally supported by an inert material [48]. This material acts as a porous support and contributes to improve some important properties of the oxygen carrier. It increases the surface area and hence the reactivity of the active material. It also helps maintaining the particle structure during the reactions.

A comprehensive review of the different oxygen carrier systems tested can be found in a doctoral thesis of Johansson [49]. Most of the research has been performed in laboratory batch reactors, often by exposing the particles to repeated oxidizing and reducing conditions and thereby simulating the chemical-looping combustion process. However, several prototype units ranging from 0.3-120 kW_{th} [50-56] have also been operated and in one case, the same particles have been used for more than 1000 h [57]. These oxygen carrier particles were based on NiO, supported by $NiAl_2O_4$, and developed in the present work. The total operational experience of chemical-looping combustion exceeds 4000 h in 12 different units with totally 29 oxygen carrier materials [58].

In addition to the primarily used metal oxides, i.e., oxides based on Ni, Cu, Mn and Fe, other materials have potential for serving as oxygen carriers. These include sulphates, such as $CaSO_4$ [59] and combined oxides, such as the mineral ilmenite, $FeTiO_3$ [55, 60, 61]. Combining Mn oxides with a number of other oxides have also been shown to be highly interesting as these materials have the ability to release gas-phase oxygen in the fuel reactor [62-64].

2.3.1 Thermal Aspects

In Paper I, the feasibility to use 27 different oxygen carrier systems for chemical-looping combustion were analyzed theoretically with respect to parameters important for oxygen carriers in chemical-looping combustion. To simulate chemical reactions and perform equilibrium calculations of these oxygen carrier systems, the HSC Chemistry 5.0 software was used and details of the method are described in Paper I. Most of the oxygen carrier systems were based on metal oxides of Ni, Cu, Fe, Cd, Mn, Co, Zn, Ce, W and Mo. Furthermore, two of the systems were based on the transition between metal sulphate and metal sulphide, i.e., Ba and Sr. $CaSO_4$/CaS was not included in Paper I but has been added here since it has been suggested as a highly promising oxygen carrier system for chemical-looping combustion [59].

To determine the degree of fuel conversion to carbon dioxide and water, gas yields for three different fuels were defined as the fraction of the fuel which is oxidized to CO_2 or H_2O, as presented in Paper I. Table 2-1 shows the gas yields, at thermodynamic equilibrium, for all these oxygen carrier systems at 800°C and 1000°C at atmospheric pressure. Of the 28 systems presented, only 8 have complete fuel conversion although roughly half of them have conversions above 0.98.

The results presented for CH_4 are highly relevant for common gaseous fuels such as natural gas and refinery gas because of their high fraction of CH_4. CO and H_2 are relevant when syngas is used in the process.

Table 2-1. The gas yield for different oxygen carrier systems. Systems with yields below 0.92 are indicated with *.

	γ_{CH_4}		γ_{CO}		γ_{H_2}	
	800°C	**1000°C**	**800°C**	**1000°C**	**800°C**	**1000°C**
NiO/Ni	**0.9949**	**0.9883**	**0.9949**	**0.9883**	**0.9946**	**0.9931**
CuO/Cu	**1.0000**	**1.0000**	**1.0000**	**1.0000**	**1.0000**	**1.0000**
Cu_2O/Cu	**1.0000**	**0.9999**	**1.0000**	**0.9999**	**1.0000**	**0.9999**
Fe_2O_3/Fe_3O_4	**1.0000**	**1.0000**	**1.0000**	**1.0000**	**1.0000**	**1.0000**
Fe_3O_4/$Fe_{0.945}O$*	**0.5406**	**0.6820**	**0.5408**	**0.6820**	**0.5264**	**0.7841**
$Fe_{0.945}O$/Fe*	**0.3676**	**0.2898**	**0.3681**	**0.2898**	**0.3548**	**0.4086**
CdO/Cd	**0.9880**	**0.9827**	**0.9880**	**0.9827**	**0.9873**	**0.9897**
Mn_2O_3/Mn_3O_4	**1.0000**	**1.0000**	**1.0000**	**1.0000**	**1.0000**	**1.0000**
Mn_3O_4/MnO	**1.0000**	**0.9999**	**1.0000**	**0.9999**	**1.0000**	**0.9999**
MnO/Mn*	**0.0000**	**0.0000**	**0.0000**	**0.0000**	**0.0000**	**0.0000**
Co_3O_4/CoO	**1.0000**	**1.0000**	**1.0000**	**1.0000**	**1.0000**	**1.0000**
CoO/Co	**0.9691**	**0.9299**	**0.9691**	**0.9299**	**0.9674**	**0.9574**
ZnO/Zn*	**0.0022**	**0.0124**	**0.0035**	**0.0124**	**0.0033**	**0.0209**
CeO_2/$CeO_{1.83}$*	**0.4426**	**0.6917**	**0.4429**	**0.6917**	**0.4288**	**0.7916**
$CeO_{1.83}$/$CeO_{1.72}$*	**0.0167**	**0.0516**	**0.0190**	**0.0517**	**0.0179**	**0.0844**
$CeO_{1.72}$/Ce_2O_3*	**0.0001**	**0.0040**	**0.0004**	**0.0040**	**0.0003**	**0.0068**
Ce_2O_3/Ce*	**0.0000**	**0.0000**	**0.0000**	**0.0000**	**0.0000**	**0.0000**
WO_3/$WO_{2.96}$	**0.9998**	**0.9984**	**0.9998**	**0.9984**	**0.9998**	**0.9991**
$WO_{2.96}$/$WO_{2.722}$	**0.9957**	**0.9858**	**0.9957**	**0.9858**	**0.9954**	**0.9916**
$WO_{2.722}$/WO_2*	**0.5647**	**0.4804**	**0.5649**	**0.4804**	**0.5506**	**0.6102**
WO_2/W*	**0.2819**	**0.3095**	**0.2827**	**0.3095**	**0.2711**	**0.4316**
MoO_3/$MoO_{2.889}$	**1.0000**	**0.9646**	**1.0000**	**0.9646**	**1.0000**	**0.9788**
$MoO_{2.889}$/$MoO_{2.75}$	**1.0000**	**1.0000**	**1.0000**	**1.0000**	**1.0000**	**1.0000**
$MoO_{2.75}$/MoO_2	**1.0000**	**0.9999**	**1.0000**	**0.9999**	**1.0000**	**1.0000**
MoO_2/MoO*	**0.2821**	**0.3060**	**0.2829**	**0.3060**	**0.2713**	**0.4275**
$BaSO_4$/BaS	**0.9822**	**0.9648**	**0.9822**	**0.9648**	**0.9812**	**0.9789**
$SrSO_4$/SrS	**0.9875**	**0.9738**	**0.9875**	**0.9738**	**0.9868**	**0.9844**
$CaSO_4$/CaS	**0.9925**	**0.9835**	**0.9925**	**0.9835**	**0.9921**	**0.9902**

Calculations in Paper I showed that when introducing Ni, Fe, Cd, Zn, Ce, W, Mo, BaS, SrS or CaS, or any partially oxidized form of these into the air reactor, they will be oxidized to NiO, Fe_2O_3, CdO, ZnO, CeO_2, WO_3, MoO_3, $BaSO_4$, $SrSO_4$ and $CaSO_4$ respectively at all temperatures and oxygen partial pressures realistic for the process. However, Cu, Mn and Co can be oxidized to CuO or Cu_2O, Mn_2O_3 or Mn_3O_4 and Co_3O_4 or CoO respectively, depending on partial pressure of oxygen and temperature, as shown in Figure 2-3.

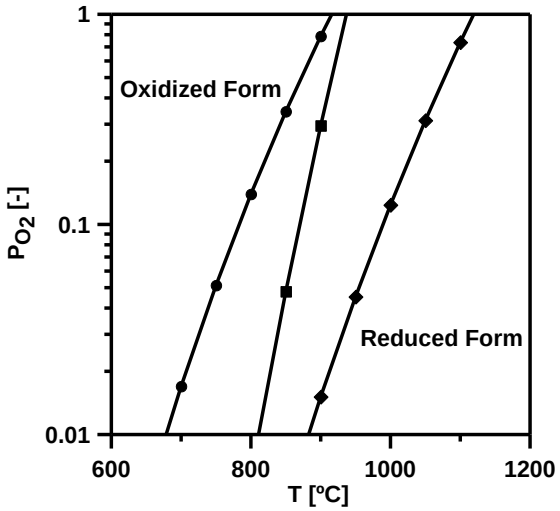

Figure 2-3. The partial pressure of oxygen at which the metal oxides decompose to their more reduced form as a function of temperature for Mn_2O_3/Mn_3O_4 (●), Co_3O_4/CoO (■) and CuO/Cu_2O (◆).

The more oxidized form is favoured at low temperatures and high oxygen partial pressures. The oxygen released and captured during transition between the two oxidation states can actually be used in the CLOU-process, especially suitable for solid fuels [42].

Other aspects of the oxygen carriers that need consideration include melting temperatures, oxygen ratios, heat balances of the reactors and possible side reactions in the fuel reactor where different sulphur containing compounds may form.

In a fluidized bed, it is important to avoid melting and agglomeration of the fluidizing particles. Agglomerations may form as the materials become soft at temperatures approaching their melting points and therefore, it would be advantageous to operate the process far below this temperature. Table 2-2 shows the melting temperatures of the investigated metals and metal oxides. Since the chemical-looping combustion process needs a temperature between 600°C and 1200°C, some of the suggested metals and metal oxides are unsuitable.

Table 2-2. Melting temperatures of the metals and metal oxides.

Melting Temperature (°C)							
Ni	1455	Mn	1246	$CeO_{1.72}$	-	$MoO_{2.889}$	-
NiO	1955	MnO	1842	$CeO_{1.83}$	-	MoO_3	802
Cu	1085	Mn_3O_4	1562	CeO_2	2400	BaS	2230
Cu_2O	1235	Mn_2O_3	1347	W	3407	$BaSO_4$	1580
CuO	1446	Co	1495	WO_2	1724	SrS	2227
Fe	1538	CoO	1830	$WO_{2.722}$	-	$SrSO_4$	1607
$Fe_{0.945}O$	-	Co_3O_4	-	$WO_{2.96}$	-	CaS	2525
Fe_3O_4	1597	Zn	420	WO_3	1472	$CaSO_4$	1460
Fe_2O_3	1565	ZnO	1975	Mo	2623		
Cd	321	Ce	798	MoO_2	1927		
CdO	-	Ce_2O_3	2230	$MoO_{2.75}$	-		

Copper has the disadvantage of a comparably low melting temperature of 1085º. Therefore, agglomeration and defluidization may occur when the particles are exposed to high temperatures. Cho et al. noticed agglomeration of freeze-granulated Cu-based oxygen carriers [65], but de Diego et al. have developed Cu-based oxygen carriers by impregnation that did not present agglomeration problems in a batch fluidized-bed reactor [66]. Furthermore, Adánez et al. tested a Cu-based oxygen carrier based on these results in a 10 kW_{th} chemical-looping combustor without defluidization or agglomeration problems [67].

From the analysis of the fuel conversion, formation of oxides in the air reactor and melting temperatures, several oxygen carrier systems are not suitable, as described in Paper I. Thus, the oxide systems indicated with * in Table 2-1 can be excluded as a result of their low ability to oxidize the fuel and Cd cannot be used because of its low melting temperature. Also, Mo is excluded because MoO_3, the oxide formed in the air reactor, has too low melting temperature.

The oxygen ratio shows the maximum mass flow of oxygen that can be transferred between the air and the fuel reactor for a given mass flow of circulating oxygen carrier particles, and is defined as:

$$R_0 = \frac{(m_{ox} - m_{red})}{m_{ox}} \tag{4}$$

where m_{ox} is the mass of oxygen carrier when fully oxidized and m_{red} is the mass of the fully reduced state. A high oxygen ratio is an advantage for the process since more oxygen can be transported per mass unit of added material. Table 2-3 displays the oxygen ratio of the investigated oxygen carrier systems. It should be noted that these oxygen ratios will decrease when an inert material is used together with the active oxygen carrier.

Table 2-3. Oxygen ratio, R_0, for the different oxygen carrier systems.

Oxygen ratio, R_0 (-)							
NiO/Ni	**0.214**	**Fe_2O_3/Fe_3O_4**	**0.033**	**Co_3O_4/Co**	**0.266**	**$BaSO_4/BaS$**	**0.274**
CuO/Cu	**0.201**	**Mn_2O_3/MnO**	**0.101**	**CoO/Co**	**0.214**	**$SrSO_4/SrS$**	**0.348**
Cu_2O/Cu	**0.112**	**Mn_3O_4/MnO**	**0.070**	**$WO_3/WO_{2.722}$**	**0.019**	**$CaSO_4/CaS$**	**0.470**

For oxygen carrier systems with a high reactivity, in combination with a high oxygen ratio, e.g., NiO/Ni, a comparatively small amount of material, and thus smaller reactor sizes, are needed.

The reaction enthalpies for the reaction between the various metals or reduced metal oxides and oxygen at 1000°C can be found in Table 2-4. The ratio of the reaction enthalpy of the oxidation to that of conventional combustion for the three fuels is also

shown. Because the overall heat released from chemical-looping combustion is the same as that from normal combustion, it is possible to determine whether the reactions in the fuel reactor are endothermic or exothermic from this ratio. A ratio above 1 means that the reaction in the fuel reactor is endothermic and a ratio below 1 indicates an exothermic fuel reactor reaction. As seen in Table 2-4, the reaction in the fuel reactor is always exothermic when H_2 or CO is used. An exothermic fuel reactor reaction is advantageous as a high particle circulation is not needed to maintain the fuel reactor temperature.

Table 2-4. Reaction enthalpies at 1000ºC.

	ΔH (kJ/mol O_2)	$\Delta H/\Delta H_{dir\ comb\ CH4}$	$\Delta H/\Delta H_{dir\ comb\ H2}$	$\Delta H/\Delta H_{dir\ comb\ CO}$
$O_2 + 1/2CH_4 \rightarrow 1/2CO_2 + H_2O$	-401.7	1.00		
$O_2 + 2H_2 \rightarrow 2H_2O$	-498.5		1.00	
$O_2 + 2CO \rightarrow 2CO_2$	-562.8			1.00
$O_2 + 2Ni \rightarrow 2NiO$	-468.5	1.17	0.94	0.83
$O_2 + 2Cu \rightarrow 2CuO$	-295.9	0.74	0.59	0.53
$O_2 + 4Cu \rightarrow 2Cu_2O$	-331.7	0.83	0.67	0.59
$O_2 + 4Fe_3O_4 \rightarrow 6Fe_2O_3$	-478.8	1.19	0.96	0.85
$O_2 + 4MnO \rightarrow 2Mn_2O_3$	-359.1	0.89	0.72	0.64
$O_2 + 6MnO \rightarrow 2Mn_3O_4$	-449.4	1.12	0.90	0.80
$O_2 + 3/2Co \rightarrow 1/2Co_3O_4$	-446.8	1.11	0.90	0.79
$O_2 + 2Co \rightarrow 2CoO$	-466.9	1.16	0.94	0.83
$O_2 + 2/0.278WO_{2.722} \rightarrow 2/0.278WO_3$	-419.6	1.04	0.84	0.75
$O_2 + 1/2BaS \rightarrow 1/2BaSO_4$	-481.7	1.20	0.97	0.86
$O_2 + 1/2SrS \rightarrow 1/2SrSO_4$	-475.7	1.18	0.95	0.85
$O_2 + 1/2CaS \rightarrow 1/2CaSO_4$	-471.0	1.17	0.94	0.84

When methane is used as fuel, the reactions in the fuel reactor are endothermic for most oxygen carriers and the fuel reactor temperature will be decreased. The temperature drop in the fuel reactor was calculated in Paper I as a function of the mass-based conversion of the oxygen carrier, ω, defined as the ratio of the actual mass and the mass in its fully oxidized state:

$$\omega = \frac{m}{m_{ox}} \tag{5}$$

The temperature difference between the reactors depends on the oxygen carrier circulation. A high mass flow gives a small difference in the mass conversion between the two reactors and results in a small temperature difference between the reactors, as displayed in Figure 2-4. Further details of the calculations are presented in Paper I. As seen, the temperature decrease for highly reduced metal oxide/sulphates is in many cases large. The implication of this is that the change in solid conversion, $\Delta\omega$, between the fuel and air reactor should be kept low by maintaining a sufficient circulation of solids.

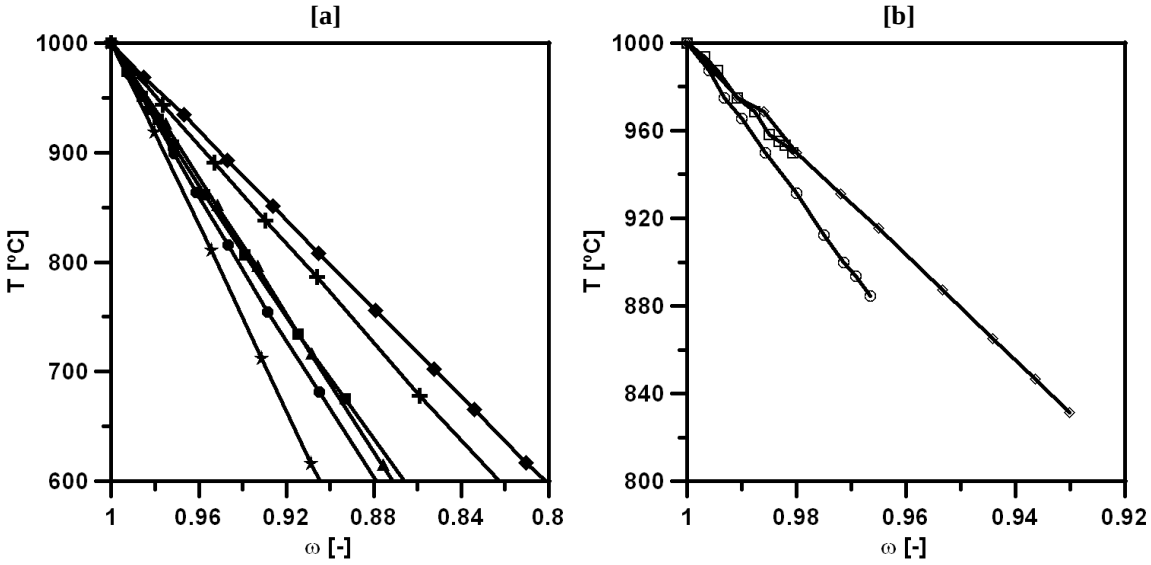

Figure 2-4. Temperature in the fuel reactor for [a] NiO/Ni (●), CoO/Co (■), Co_3O_4/Co (◆), $SrSO_4$/SrS (▲), $BaSO_4$/BaS (★), $CaSO_4$/CaS (✚) and [b] Fe_2O_3/Fe_3O_4 (○), $WO_3/WO_{2.722}$ (□), Mn_3O_4/MnO (◇) as a function of oxygen carrier conversion.

The results of the thermal analysis in Paper I for the different oxygen carrier systems feasible for the process are summarized in Table 2-5 below. Since the results are calculated from a theoretical thermodynamic analysis of the process, it should be noted that all the results refer to equilibrium. However, in a real application the rates of reaction are also very important and have implications with respect to the size of a chemical-looping combustion system. The results for conversion of H_2S to SO_2 and formation of sulphides/sulphates will be described in section 2.3.2.

Table 2-5. Comparison of different oxygen carrier systems.

	Fuel conversion	*Decomposition temp. for P_{O2}=0.04*	*Melting temp.*	*Conversion of H_2S to SO_2*	*Sulphide/ Sulphate formed*
NiO/Ni	**I**			**I**	**Ni_3S_2**
CuO/Cu		**944°C**	**1085°C**		
Cu_2O/Cu			**1085°C**		
Fe_2O_3/Fe_3O_4					
Mn_2O_3/MnO		**738°C**			**$MnSO_4$***
Mn_3O_4/MnO					
Co_3O_4/Co	**L**	**845°C**		**I**	**$CoS_{0.89}$**
CoO/Co	**L**			**L**	**$CoS_{0.89}$**
$WO_3/WO_{2.722}$	**I**			**I**	
$BaSO_4$/BaS	**I**				
$SrSO_4$/SrS	**I**				
$CaSO_4$/CaS	**I**				

*Only at lower temperatures; I=incomplete; L=low

2.3.2 Fate of Sulphur Species

Refinery gas and natural gas may contain small amounts of sulphur-containing species, primarily H_2S. The fate of H_2S in the fuel reactor is highly dependent on the oxygen

carrier used; it may be oxidized to SO_2 by oxidants such as H_2O, CO_2 or the metal oxide. Further, solid sulphur compounds may form by reactions with the oxygen carrier.

For CuO/Cu, Cu_2O/Cu, Fe_2O_3/Fe_3O_4, Mn_2O_3/MnO and Mn_3O_4/MnO, H_2S in the fuel will be converted to SO_2 to somewhere between 99.3 and 100%, for every temperature between 600°C and 1200°C, as calculated in Paper I. For the NiO/Ni, $WO_3/WO_{2.722}$ and the two systems including cobalt oxides, i.e., Co_3O_4/Co and CoO/Co, the conversion of H_2S is somewhat lower, as displayed in Figure 2-5. As seen, the oxidation of H_2S is enhanced at high temperatures and low pressures.

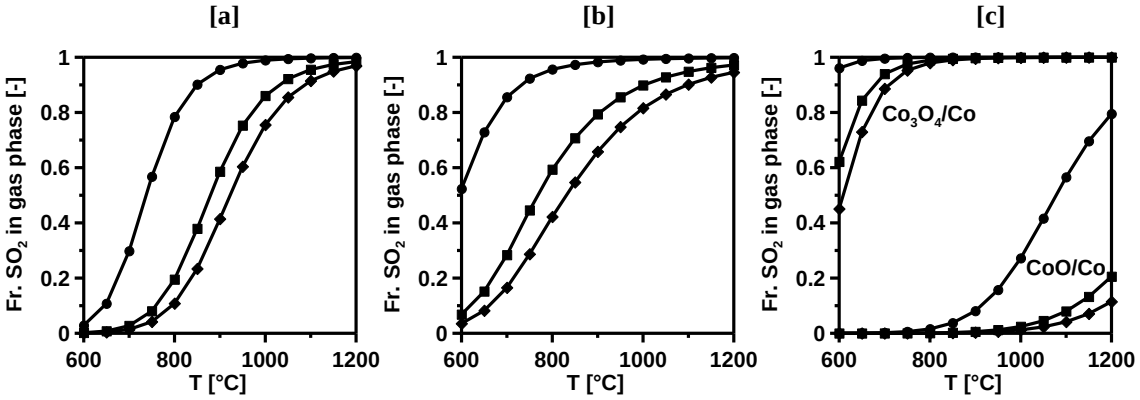

Figure 2-5. Degree of conversion from H_2S in the fuel to SO_2 at 1 bar (●), 15 bar (■) and 30 bar (◆) for [a] NiO/Ni, [b] $WO_3/WO_{2.722}$ and [c] CoO/Co and Co_3O_4/Co.

Formation of metal sulphides or sulphates could result in oxygen carrier deactivation. Thus, calculations were performed in Paper I to find out at what partial pressure of sulphur-containing gases formation could occur. In summary, the risk of sulphide formation is significant if Ni or Co is used and for the Mn_2O_3/MnO system, formation of $MnSO_4$ may occur at low temperatures, as shown in Figure 2-6. The sulphur concentration needed for formation of these compounds increases with temperature and decreases with total pressure.

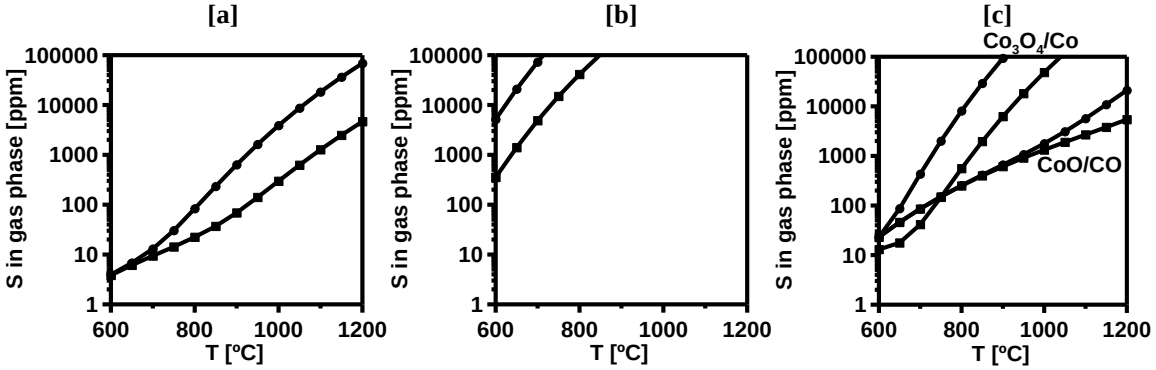

Figure 2-6. Concentration of sulphur containing gases needed at 1 bar (●) and 15 bar (■) for formation of [a] Ni_3S_2 with Ni/NiO, [b] $MnSO_4$ with Mn_2O_3/MnO and [d] $CoS_{0.89}$ with Co_3O_4/Co and CoO/Co.

For systems containing $BaSO_4$/BaS, $SrSO_4$/SrS and $CaSO_4$/CaS, SO_2 may form by decomposition of the sulphate, predominantly at high temperatures and low total pressures, as shown in Figure 2-7. Decomposition results in formation of sulphur-containing gases and the metal oxides BaO, SrO and CaO, respectively. Thus, to avoid loss of oxygen carrier by decomposition, the sulphur content of the added fuel must not be too low and the temperature should not be too high.

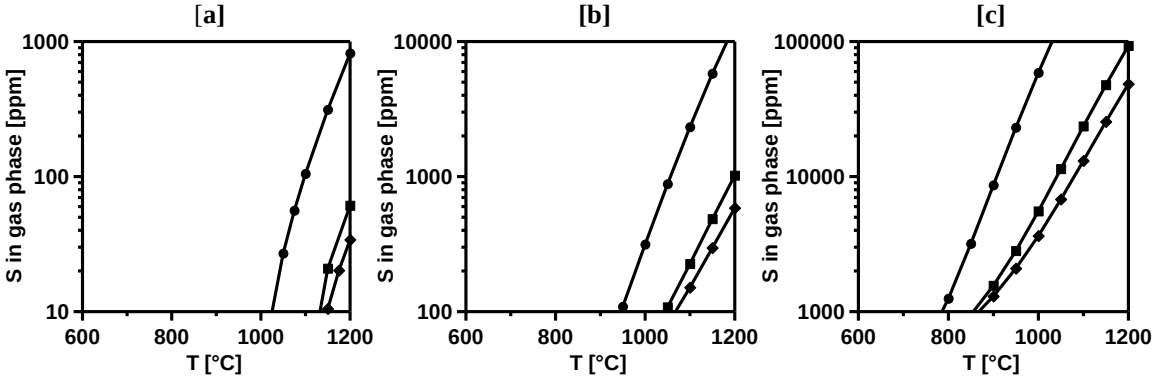

Figure 2-7. Decomposition temperature at different concentrations of sulphur containing gases at 1 bar (●), 15 bar (■) and 30 bar (◆) for [a] $BaSO_4$, [b] $SrSO_4$ and [c] $CaSO_4$.

2.3.3 Selection of Oxygen Carriers for this Work

The most frequently investigated oxygen carrier systems for chemical-looping combustion are; NiO/Ni, CuO/Cu, Mn_3O_4/MnO and Fe_2O_3/Fe_3O_4. Most of these oxygen carrier materials have been prepared by combining the active material to an inert support material such as SiO_2, TiO_2, ZrO_2, Al_2O_3, YSZ or bentonite [45, 49, 68]. The oxygen carriers can be prepared under different conditions by numerous production methods such as; freeze-granulation [69], impregnation [70] mechanical mixing [71], co-precipitation [72], spray-drying [73] or spin-flash drying [74]. The choice of oxygen carrier materials is highly dependent on the intended application and the large number of materials and preparation methods gives rise to an infinite number of possible oxygen carriers with varying properties.

Considerable work has been performed on investigating the reactivity of different oxygen carriers. However, it is difficult to compare the reactivity directly as it varies significantly with parameters such as fuel; preparation method, inert material and size of oxygen carrier particles; type and size of the reactor and experimental conditions such as gas velocities and reaction temperature. Still, from reactivity investigations comparing different oxygen carriers with CH_4 as fuel, it can be concluded that NiO and CuO are generally far more reactive than Mn_3O_4 and Fe_2O_3 [47, 65, 69, 75, 76]. The price of these metals follows the opposite order as the reactivity, with Fe being the cheapest and Ni the

most expensive [45]. Further, Ni has the disadvantages of a higher toxicity compared to the other proposed oxygen carrier materials and a restricted fuel conversion due to limitations from thermodynamic equilibria. However, as a high reaction temperature is needed when chemical-looping combustion is integrated in a natural gas combined cycle, the low melting temperature of Cu may cause problems and Ni is believed to be the primary option in such applications [35]. With NiO as oxygen carrier, the overall reaction in the fuel reactor is:

$$4NiO + CH_4 \leftrightarrow 4Ni + CO_2 + 2H_2O \quad (6)$$

and in the air reactor:

$$4Ni + 2O_2 \leftrightarrow 4NiO \quad (7)$$

For Ni-based oxygen carriers, Al_2O_3 and $NiAl_2O_4$ have received the most attention as support materials because of their favourable fluidization properties and thermal stability [68]. The first results with NiO supported by $NiAl_2O_4$ were presented by Ishida et al. in 1998 [77] and in the following year, Jin et al. stated that this material combination may play a vital role in developing chemical-looping combustion [78]. NiO/$NiAl_2O_4$ has displayed a high reactivity with CH_4, CO, H_2 and O_2 [68, 73, 78-80], its chemical composition, structure and reactivity seems fairly unchanged after continuous operation in a 10 kW_{th} chemical-looping combustor [81], as well as at reduction and oxidation temperatures up to 1200ºC [73, 82]. Further, this material combination has been tested in fluidized beds without agglomeration problems [51, 74, 83]. Linderholm et al. obtained a fuel conversion of above 99% with carriers based on these materials, in a 10 kW_{th} unit [74], and the reactions of NiO/$NiAl_2O_4$, with alternating methane and oxygen, have been studied in detail by Mattisson et al. [84]. Here, it was found that although $NiAl_2O_4$ can release oxygen to the fuel, this reaction is extremely slow compared to the reaction of NiO with CH_4. Hence, $NiAl_2O_4$ is considered as an inert material. Further, there is a thermodynamic limitation of the $NiAl_2O_4$ in converting CH_4 to CO_2 and H_2O. Another support material, for Ni-based oxygen carriers, which has gained an increased interest is $MgAl_2O_4$ [72]. Selection of $MgAl_2O_4$ instead of $NiAl_2O_4$ has been found to give an improved methane conversion, higher selectivity to reforming and a lower tendency for carbon formation [85]. NiO supported by $MgAl_2O_4$ has also been successfully tested in continuous operation [86, 87].

When adapting chemical-looping combustion to convert solid fuels, the requirements of the oxygen carriers are somewhat different as compared to the case of using gaseous

fuels. If direct introduction of the solid fuel to the fuel reactor is used, the lifetime of the oxygen carriers is expected to be shorter as compared to when gaseous fuels are being used. The reason for this is possible ash deactivation of the oxygen carriers and loss of oxygen carrier particles during ash separation. For this reason, the use of low-cost and environmentally friendly oxygen carriers is important. Further, as the gasification products from solid fuels are mainly CO and H_2, as displayed in reaction (3), expensive oxygen carriers with high reaction rates with CH_4 may not be useful to employ in a solid fuel application. Fe-based oxygen carriers have the advantage of being comparatively cheap, environmentally sound and accessible in large quantities [88, 89]. Generally, these materials display higher reactivity towards CO and H_2 than towards CH_4 [90, 91]. Therefore, Fe-based oxygen carriers could be suitable for solid fuel applications. Most studies regarding Fe-based oxygen carriers have focused on particles manufactured from pure chemicals and stabilized by supporting materials [90, 92]. However, to further decrease the oxygen carrier cost when utilizing solid fuels, an option is to use natural minerals, such as iron ores [93], or by-products from other processes, such as oxide scales from the steel industry [91]. Leion et al. have concluded that such materials are good candidates for converting solid fuels in chemical-looping combustion [94] and Xiao et al. have reported promising results using an iron ore to convert solid fuels in a fixed bed reactor under pressurized conditions [89]. The overall reaction in the fuel reactor, for Fe-based oxygen carriers, with syngas as fuel is:

$$3Fe_2O_3 + CO/H_2 \leftrightarrow 2Fe_3O_4 + CO_2/H_2O \quad (8)$$

and in the air reactor:

$$2Fe_3O_4 + \frac{1}{2}O_2 \leftrightarrow 3Fe_2O_3 \quad (9)$$

Moldenhauer has investigated the natural mineral ilmenite and an iron based oxide scale in a 300 W_{th} circulating chemical-looping combustion unit, fuelled by syngas, to improve the understanding of the lifetime behaviour and other basic characteristics of these oxygen carrier materials [95].

Ilmenite has been suggested as a capable oxygen carrier material for combustion of solid fuels and investigated extensively. The reduced form of ilmenite is $FeTiO_3$ and the completely oxidized state is pseudobrookite, Fe_2TiO_5 and rutile, TiO_2 [60, 61]. Ilmenite has been used in a 10 kW_{th} chemical-looping combustor [55] with solid fuels, its properties have been studied experimentally in a laboratory setup, where reactivity

towards CH_4 and CO/H_2 as well as fluidization behaviour were investigated [60]. Furthermore, ilmenite has been tested in a 120 kW_{th} chemical-looping combustor fuelled by H_2 [54] and structural changes of the material after successive reduction and oxidation periods have been analyzed [61]. The overall reaction in the fuel reactor with ilmenite as oxygen carrier is:

$$Fe_2TiO_5 + TiO_2 + CO/H_2 \leftrightarrow 2FeTiO_3 + CO_2/H_2O \quad (10)$$

and in the air reactor:

$$2FeTiO_3 + \frac{1}{2}O_2 \leftrightarrow Fe_2TiO_5 + TiO_2 \quad (11)$$

2.4 Carbon Formation

Under certain conditions solid carbon deposition on the oxygen carrier particles may occur if a carbon-containing fuel is used. Carbon formed can be transported back to the air reactor, causing CO_2 formation, and hence lower the separation efficiency of CO_2 [96]. Solid carbon may form through methane decomposition:

$$CH_4 \rightarrow C + 2H_2 \quad (12)$$

or through the Boudouard reaction:

$$2CO \rightarrow C + CO_2 \quad (13)$$

The oxygen added ratio, ς, is defined as the actual amount of O added to the gas, over the stoichiometric amount needed for full conversion of the fuel gas:

$$\varsigma = \frac{n_{O,added}}{n_{O,stoich}} \quad (14)$$

Normally, low temperatures and small amounts of added oxygen benefit the formation, as calculated in Paper I and shown in Figure 2-8. Here, the oxygen added ratio, equation (14), below which carbon formation is thermodynamically feasible, is shown as a function of temperature. With CH_4 as fuel, an increased pressure will favour carbon formation at low temperatures while an increased pressure counteracts carbon formation at high temperatures. This is due to the fact that carbon is formed by two reactions, the

methane decomposition reaction (12), dominating at high temperatures and the Boudouard reaction (13), dominating at lower temperatures. By methane decomposition, less carbon is formed at higher pressures while by the Boudouard reaction, more carbon is formed at higher pressures.

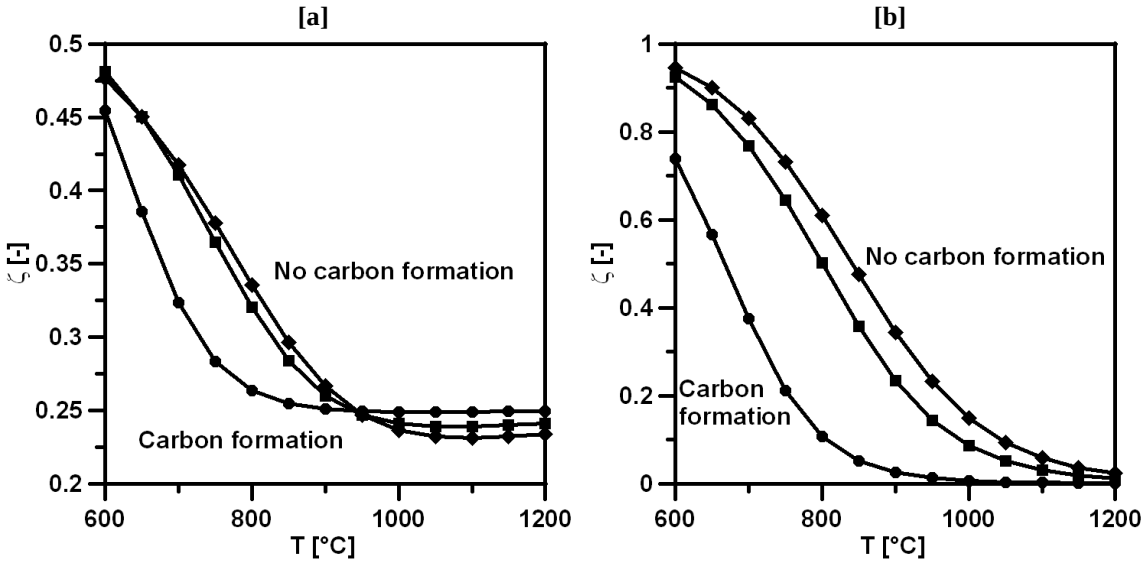

Figure 2-8. The oxygen added ratio, ς, needed to avoid carbon formation at 1 bar (●), 15 bar (■) and 30 bar (♦) with [a] CH_4 and [b] CO as fuel.

When CO is used as fuel, the Boudouard reaction is the only reaction accounting for carbon formation. Therefore, formation is favoured at low temperatures, small amounts of added oxygen and high pressures.

Since the fuel conversion in a chemical-looping combustion process always should be high, the amount of added oxygen is well over the amount where carbon formation is possible. Therefore, problems with carbon formation are not expected in a well-mixed fluidized fuel reactor.

2.5 Objective

The purpose of the present work can be divided into three parts. Paper I is a comprehensive thermodynamic investigation, intended to evaluate the feasibility of 27 different oxygen carrier systems for chemical-looping combustion with gaseous fuels. In this theoretic work, important parameters for each system such as restrictions in fuel conversion, reoxidation in the air reactor, oxygen transport capacity, heat balances in the fuel reactor, melting temperatures and conditions in the fuel reactor at which undesired side products like sulphur containing compounds and carbon might form are analyzed for each system. Paper I acts as opening to the experimental work performed in later

publications and therefore, the results of Paper I are summarized in section 2.3.1, 2.3.2 and 2.4 of this thesis.

Paper II-V presents experimental results for oxygen carriers of NiO, mostly supported by $NiAl_2O_4$. The main reason for using Ni-based oxygen carriers to convert gaseous fuels is the high reaction rate with methane, the main component in natural- and refinery gas, in combination with a high melting temperature, which reduces the risk of agglomeration when exposed to high temperatures. Previously, the oxygen carrier materials developed for chemical-looping combustion have mainly been prepared using very fine and pure materials. In order for this system to be viable for use in a power plant, it is important that the raw materials are both commercial and can be obtained in large quantities at a reasonable cost. Thus, the aim of Paper II is to verify that commercially available raw or semi-finished materials can be used to produce high performing oxygen carriers of $NiO/NiAl_2O_4$. Paper III investigates if these oxygen carriers could be prepared with a method well suited for large-scale particle production, i.e., spray-drying. In Paper IV, it is investigated if $MgAl_2O_4$ or MgO and/or $Ca(OH)_2$ can be used as additives to increase the performance of the spray-dried oxygen carriers, prepared by commercially available raw materials. In Paper V, one of the more promising Ni-based oxygen carriers found in the prior screening investigation is examined more closely, and a comparison of the reactivity data from the small fluidized bed reactor with actual reactivity data from a 10 and 120 kW_{th} circulating chemical-looping combustion reactor is made. All oxygen carriers produced in Paper II-V are analyzed with respect to parameters important for a process utilizing gaseous fuels with a high CH_4 content, regarding both chemical and physical properties as well as reactivity and gas conversion.

In Paper VI-VII, iron-based oxygen carriers are investigated experimentally. In Paper VI, the main purpose is to improve the understanding of ilmenite, the most frequently investigated oxygen carrier in solid fuel applications. To achieve this, both synthetically produced ilmenites with varying Fe:Ti ratios and ilmenite minerals are investigated with syngas as fuel, the main gasification product when solid fuels are utilized. In Paper VII, several industrial iron-based materials and an iron ore are studied with respect to parameters important for oxygen carriers in chemical-looping combustion with solid fuels. Here, natural Norwegian ilmenite is used as a reference material. Further, one oxygen carrier in Paper VII is tested with three different solid fuels and compared to this reference sample.

3

EXPERIMENTAL

3.1 Preparation of Oxygen Carriers

There is considerable experience in producing high performing oxygen carrier particles for chemical-looping combustion by freeze-granulation at laboratory scale. However, in an industrial application of chemical-looping combustion, a production method better suited for large scale particle preparation is necessary. Spray-drying is a well established industrial method for production of dry solid particles in large quantities. The technology has been applied in many areas, including the food-, pharmaceutical-, ceramic-, polymer-, and chemical industries [97]. The spray-dried oxygen carriers are investigated in Paper III-V.

The oxygen carriers investigated in Paper II-V are based on 6 different NiO materials, obtained from 4 different commercial suppliers. Physical properties of the commercially available raw materials, including the $MgAl_2O_4$ investigated in Paper IV and the MgO and $Ca(OH)_2$ investigated in Paper II and IV, are displayed in Table 3-1.

Table 3-1. Commercial raw materials used in oxygen carrier production.

	Density (kg/m^3)*	***BET-Surface (m^2/g)*****
Raw Material, NiO		
Novamet Refractory grade	**6600**	**3.5**
Novamet Green grade F	**6810**	**3.6**
OMG Standard grade	**6210**	**46.5**
OMG HSA grade	**5790**	**130**
Umicore	**6800**	**58.5**
Vogler Brown grade	**6100**	**1.3**
Raw Material, α-Al_2O_3		
Almatis CT3000SG	**3960**	**7.0**
Almatis CT800FG	**3960**	**1.0**
Raw Material, $MgAl_2O_4$		
Almatis CTC55	**2500**	**3.5-4.7**
Almatis E-SY2000	**3400**	**2.1-2.8**
Almatis AR78	**3300**	**<0.5**
Additive, MgO		
MagChem30	**3590**	**24.2**
Additive, $Ca(OH)_2$		
Nordkalk SL	**2330**	**16.0**

*Measured by a Helium pycnometer, Micromeretics, AccuPyc 1330 or GeoPyc 1360
**Measured by Nitrogen adsorption, Micromeritics, Flowsorb II 2300 or Gemini 2360

3.1.1 Freeze-Granulation

A fine powder of the raw materials was combined with polyacrylic acid as dispersant. Water-based slurries of the mixtures were prepared by ball milling for about 24 h. After milling, polyethylene glycol was added as a binder to keep the particles intact during freeze-drying and sintering. Spherical particles were produced by pumping the slurry to a spray nozzle where passing atomizing-air produced drops, which were sprayed into liquid nitrogen where they froze instantaneously. The frozen water in the resulting particles was then removed by sublimation in a freeze-drier. After drying, the Ni-based particles were sintered at three different temperatures, 1400, 1500 and 1600°C for 6 h. During heat treatment, the α-Al_2O_3 reacted completely with part of the NiO to form the supporting spinel $NiAl_2O_4$. An excess of NiO was used in the preparation to achieve a mass ratio between NiO and $NiAl_2O_4$ of 4/6.

In an initial screening, 30 oxygen carriers were prepared by combining the different NiO and α-Al_2O_3 materials from various suppliers, shown in Table 3-1. These particles are presented in Table 3-2, where the sintering temperature is given in the abbreviation for each oxygen carrier.

Table 3-2. Physical properties of particles produced by freeze-granulation, investigated in Paper II. Oxygen carriers in italic typeface defluidized during reactivity testing.

NiO	***α-Al_2O_3***							
	Almatis CT3000SG				**Almatis CT800FG**			
	Oxygen Carrier Abbr.	**BET-Surface (m^2/g)***	**Crushing Strength (N)****	**Apparent Density (kg/m^3)*****	**Oxygen Carrier Abbr.**	**BET-Surface (m^2/g)***	**Crushing Strength (N)****	**Apparent Density (kg/m^3)*****
Novamet Refractory grade	**NOV1T1400**	**0.91**	**1.4**	**2400**	**Was not Prepared**			
	NOV1T1500	*0.52*	*4.1*	*3400*				
	NOV1T1600	*0.04*	*11.7*	*4460*				
Novamet Green grade F	**NOV2T1400**	**1.85**	**1.6**	**2490**				
	NOV2T1500	*0.97*	*3.8*	*3180*				
	NOV2T1600	*0.18*	*9.2*	*4380*				
OMG Standard grade	**OMG1T1400**	-	**S**	**1770**	*OMG2T1400*	**No Spherical Particles**		
	OMG1T1500	**1.43**	**0.4**	**2060**	*OMG2T1500*			
	OMG1T1600	*0.55*	*1.3*	*2810*	*OMG2T1600*			
OMG HSA grade	**OMG3T1400**	-	**S**	**1440**	*OMG4T1400*	**No Spherical Particles**		
	OMG3T1500	**1.28**	**0.5**	**1790**	*OMG4T1500*			
	OMG3T1600	*0.48*	*1.6*	*2920*	*OMG4T1600*			
Umicore	**UMI1T1400**	**2.38**	**0.2**	**1470**	*UMI2T1400*	*1.14*	*0.2*	*2070*
	UMI1T1500	**1.53**	**0.4**	**1940**	*UMI2T1500*	*0.61*	*0.4*	*2290*
	UMI1T1600	*0.47*	*1.2*	*3140*	*UMI2T1600*	*0.41*	*0.7*	*2410*
Vogler Brown grade	**VOG1T1400**	-	**S**	**1290**	*VOG2T1400*	**No Spherical Particles**		
	VOG1T1500	-	**S**	**1690**	*VOG2T1500*	-	*S*	*1350*
	VOG1T1600	*0.48*	*0.6*	*2410*	*VOG2T1600*	-	*S*	*1550*

*Measured by Micromeritics, Flowsorb II 2300; **Average force needed to fracture individual particle; ***Assuming a void factor of 0.37; S - Too soft to measure crushing strength

Of the oxygen carriers prepared, seven failed in the production phase, i.e., no spherical particles were obtained, and six formed too soft granules to give a distinct crushing strength value. These problems occurred mainly with the cheaper and coarser α-Al_2O_3 material, i.e., Almatis CT800FG. The reason for this is likely the larger size of the

particles in the raw material of this α-Al_2O_3, which limits the contact area for reaction with the nickel oxides. For this reason, some material combinations were not prepared using Almatis CT800FG.

To study the effect of additions of MgO and $Ca(OH)_2$ to oxygen carriers based on NiO, six oxygen carriers using OMG HSA grade NiO and Almatis CT3000SG α-Al_2O_3 were prepared. The ratio of 4/6 between the active NiO and the supporting material was maintained. However, 1% MgO, 5% MgO or 1% $Ca(OH)_2$, based on weight, was added during particle production, as shown in Table 3-3. It is believed that these additions result in formation of the inert spinel $MgAl_2O_4$ or $CaAl_2O_4$. Results for all Ni-based oxygen carriers prepared by freeze-granulation are presented in Paper II.

Table 3-3. Physical properties of NiO-based particles produced by freeze-granulation with additives, investgated in Paper II. Oxygen carriers in italic typeface defluidized during reactivity testing.

Additive	***NiO/α-Al_2O_3*** **OMG HSA grade/Almatis CT3000SG**			
	Oxygen Carrier Abbreviation	**BET-Surface (m^2/g)***	**Crushing Strength (N)****	**Apparent Density (kg/m^3)*****
1% MgO MagChem30	**OMG5T1500**	**-**	**S**	**1680**
	OMG5T1600	*0.69*	*0.6*	*2380*
5% MgO MagChem30	**OMG6T1500**	**-**	**S**	**1770**
	OMG6T1600	**0.37**	**0.9**	**2780**
1% $Ca(OH)_2$ Nordkalk SL	*OMG7T1500*	*0.19*	*4.2*	*3730*
	OMG7T1600	*0.056*	*7.0*	*4330*

*Measured by Micromeritics, Flowsorb II 2300; **Average force needed to fracture individual particle; ***Assuming a void factor of 0.37; S - Too soft to measure crushing strength

The ten Fe/Ti-based oxygen carriers were sintered at 1100°C for 6 h. During the sintering process, the mixtures containing pure Fe_2O_3 and TiO_2 powders at different ratios formed pseudobrookite, Fe_2TiO_5, the most oxidized level of ilmenite in a chemical-looping combustion process. Details of these oxygen carriers are presented in Table 3-4 and investigated in Paper VI. Here, the materials are compared to a natural Norwegian ilmenite, supplied by Titania A/S and a South African ilmenite, supplied by IFP.

Table 3-4. Properties of particles produced by freeze-granulation from Fe_2O_3/TiO_2, investigated in Paper VI.

Oxygen Carrier Abbreviation	***Fe:Ti ratio (% molar based)***	***Crushing strength (N)****	***Phases indicated by XRD***
sample 1-1	**50:50**	**2.67**	**Fe_2TiO_5, TiO_2**
sample 1-2	**52.4:47.6**	**2.80**	**Fe_2TiO_5, TiO_2**
sample 1-3	**47.6:52.4**	**2.80**	**Fe_2TiO_5, TiO_2**
sample 2-1	**45:55**	**2.46**	**Fe_2TiO_5, TiO_2**
sample 2-2	**55:45**	**1.95**	**Fe_2TiO_5, TiO_2**
sample 2-3	**40:60**	**2.27**	**Fe_2TiO_5, TiO_2**
sample 2-4	**60:40**	**1.70**	**Fe_2TiO_5, TiO_2**
sample 2-5	**25:75**	**3.50**	**Fe_2TiO_5, TiO_2**
sample 2-6	**75:25**	**1.47**	**Fe_2TiO_5, Fe_2O_3**
sample 2-7	**100:0**	**1.62**	**Fe_2O_3**

*Average force needed to fracture individual particle

3.1.2 Spray-Drying

A powder mixture of NiO and α-Al_2O_3 was dispersed in deionized water containing the necessary organic additives. Polyethyleneoxide and/or polyvinylalcohol and/or polyethyleneglycol were used as organic binder. Darvan C or Dolapix were used as dispersants. The suspension was homogenized either by milling in a planetary ball mill for small quantities or by means of a horizontal attrition mill for larger amounts. The water-based suspension was continuously stirred with a propeller blade mixer while being pumped to a 2-fluid spray-dry nozzle. Sintering was performed in air at top temperatures in the range of 1400°C to 1600°C, generally for 4 hours but two batches were sintered for 8 and 16 hours respectively. Further details on the production procedure can be found in Paper III.

A total of 17 oxygen carrier materials were produced in this manner and investigated in Paper III. All of the oxygen carriers were prepared with the α-Al_2O_3 Almatis CT3000SG while the NiO raw material was varied. Nine of the materials were prepared with the NiO Novamet Refractory grade, at five different sintering temperatures, NOV1T1400sd-NOV1T1500sd, and three different sintering times, NOV1T1450t4sd-NOV1T1450t16sd, as indicated in the oxygen carrier abbreviation in Table 3-5. One of the materials, NOV1T1450m30sd, was prepared in a larger batch of 30 kg to investigate up-scaling of the particle production. Three materials were prepared with the NiO Novamet Green grade F, NOV2T1400sd-NOV2T1500sd, each prepared at a different sintering temperature. Further, five materials were prepared with the nickel oxides OMG HSA grade, Vogler Brown grade and Umicore at varying sintering temperatures and times.

Table 3-5. Physical properties of particles produced by spray-drying, investigated in Paper III.

NiO	***α-Al_2O_3*** *Almatis CT3000SG*		
	Oxygen Carrier Abbreviation	**Crushing Strength (N)***	**Apparent Density (kg/m^3)****
Novamet Refractory grade	**NOV1T1400sd**	**1.6**	**2900**
	NOV1T1425sd	**1.8**	**2990**
	NOV1T1450sd	**1.8**	**3190**
	NOV1T1475sd	**2.7**	**3470**
	NOV1T1500sd	**3.0**	**3550**
	NOV1T1450t4sd	**2.3**	**3190**
	NOV1T1450t8sd	**2.7**	**3500**
	NOV1T1450t16sd	**3.6**	**3750**
	NOV1T1450m30sd	**2.3**	**3210**
Novamet Green grade F	**NOV2T1400sd**	**1.2**	**2830**
	NOV2T1450sd	**1.5**	**3030**
	NOV2T1475sd	**1.9**	**3350**
OMG HSA grade	**OMG3T1600t16sd**	**0.4**	**2920**
Vogler Brown grade	**VOG1T1475sd**	**0.6**	**2850**
	VOG1T1600t16sd	**0.8**	**3600**
Umicore	**UMI1T1475sd**	**0.3**	**2230**
	UMI1T1600t16sd	**0.6**	**3220**

*Average force needed to fracture individual particle; **Assuming a void factor of 0.37

To further increase the performance of the spray-dried particles, 24 oxygen carriers with varying support materials were prepared and investigated in Paper IV. The NiO and support materials used are presented in Table 3-6. All materials were prepared to give an active NiO content of 40 wt%. The additions of MgO and $Ca(OH)_2$ presented in Table 3-6 are mass fractions based on the total mass of raw material.

Table 3-6. Raw materials used in oxygen carrier optimization by spray-drying in Paper IV.

Oxygen Carrier Abbreviation	*NiO*	*Support 1*	*Support 2*	*Support 3*
S1	Novamet Refractory grade	α-Al_2O_3, CTC3000sg	5% MgO, Magchem30	
S2	OMG Standard grade	α-Al_2O_3, CTC3000sg	5% MgO, Magchem30	1% $Ca(OH)_2$, Nordkalk
S3	Novamet Refractory grade	$MgAl_2O_4$, CTC55		
S4	OMG Standard grade	$MgAl_2O_4$, CTC55		
S5	Novamet Refractory grade	α-Al_2O_3, CTC3000sg	1% MgO, Magchem30	
S6	Novamet Refractory grade	$MgAl_2O_4$, E-SY2000		
S7	Novamet Refractory grade	$MgAl_2O_4$, AR78		
S8	Novamet Refractory grade	α-Al_2O_3, CTC3000sg	10% MgO, Magchem30	
S9	OMG Standard grade	α-Al_2O_3, CTC3000sg	1% $Ca(OH)_2$, Nordkalk	

Sintering of these oxygen carriers was performed in air at top temperatures in the range of 1300°C to 1600°C, for 4 hours. This sintering temperature is displayed in the abbreviation for each oxygen carrier in Table 3-7.

Table 3-7. Physical properties of particles produced with varying support material by spray-drying, investigated in Paper IV.

Oxygen Carrier Abbreviation	*Crushing Strength [N]**	*Apparent Density [kg/m^3]***	*Oxygen Carrier Abbreviation*	*Crushing Strength [N]**	*Apparent Density [kg/m^3]***
S1T1400	2.0	2850	S6T1400	1.6	2990
S1T1450	3.4	3360	S6T1450	2.5	3200
S2T1400	0.5	2040	S6T1500	3.5	3470
S2T1500	1.6	3360	S7T1400	2.1	2920
S2T1600	2.8	3950	S7T1450	3.1	3060
S3T1400	1.3	2850	S7T1500	3.5	3230
S4T1400	S	2070	S8T1400	2.5	2910
S4T1500	0.1	2220	S8T1450	3.9	3480
S4T1600	0.3	2530	S8T1500	5.0	3740
S5T1400	1.6	2970	S9T1300	S	1800
S5T1500	2.7	3290	S9T1400	0.2	2070
S5T1600	3.6	3660	S9T1500	1.1	3180

*Average force needed to fracture individual particle; **Assuming a void factor of 0.37; S - Too soft to measure crushing strength

3.1.3 Unprocessed Materials

In Paper VII, the oxygen carriers are not manufactured by any particle preparation method. Instead, seven of these were oxide scales, a by-product from the steel industry,

four from Scana, two from Sandvik and one from ESAB. Further, an industrial iron material from Höganäs, an unprocessed iron ore from LKAB and a magnetic material obtained from vehicle recycling from Stena Metall were tested. Before the reactivity experiments, each of these oxygen carrier material was heated in air at 950°C for about 24 h to obtain a high degree of oxidation and then sieved into narrow size fractions. These materials, and their physical strength, are presented in Table 3-8.

Table 3-8. Unprocessed oxygen carriers, investgated in Paper VII.

Oxygen Carrier Material	*Crushing Strength (N)**
Scana 1	**12.2**
Scana 2	**11.0**
Scana 3	**11.4**
Scana 8	**8.7**
Sandvik 1	**11.0**
Sandvik 2	**9.6**
ESAB	**F**
Stena Metall	**3.6**
Höganäs	**3.9**
LKAB	**5.9**
Ilmenite	**4.0**

*Average force needed to fracture individual particle; F - Flake-like geometry, crushing strength could not be measured.

3.2 Characterization of Oxygen Carriers

The oxygen carriers in chemical-looping combustion will be exposed to harsh conditions such as high temperatures and high gas velocities. To avoid major fragmentation and attrition, it is expected that oxygen carriers need to possess certain strength. Thus, the crushing strength, or the force needed to fracture the particles, was measured as an average of 30 particles, sized 180-250 μm for the freeze-granulated and unprocessed particles and 180-212 μm for the spray-dried particles, using a Shimpo FGN-5 device. Although these crushing strength tests give information about the strength of single particles, their resistance to fragmentation and attrition in a circulating system is also dependent on properties of their environment such as interactions with surrounding particles, chemical-reactions, time, velocity, pressure and temperature [98]. Therefore, the crushing strength can only be regarded as an indicative value that needs to be complemented by experiments in circulating units.

To study the chemical composition and investigate possible phase transitions of the oxygen carriers, both after the sintering process and the reactivity tests, the particles were analyzed using X-ray powder diffraction by a Siemens D5000 powder diffractometer, utilizing Cu Kα radiation. The shape and morphology of fresh and tested oxygen carriers were studied using a FEI, Quanta 200 Environmental Scanning Electron Microscope FEG. The Environmental Scanning Electron Microscope was equipped with an Oxford

Inca Energy dispersive X-ray system, by which information on the elemental surface composition was obtained for some of the oxygen carriers.

Further, the industrial iron-based materials and the natural iron ore presented in Paper VII were analyzed by Inductively Coupled Plasma – Optical Emission Spectrometry (ICP-OES). The analysis was performed prior to the reactivity investigation to determine the chemical composition of each oxygen carrier material.

Also, the apparent density of all synthetically produced oxygen carriers, sized 125-180 µm, was determined. The apparent density was calculated by weighing 5 ml of particles filled in a cylinder and assuming a void factor of 0.37, which is the theoretical voidage of a normally packed bed with uniformly sized spherical particles [32].

3.3 Reactivity Investigation of Oxygen Carriers

The reactivity investigations were conducted in a fluidized bed reactor of quartz, with a length of 870 mm and an inner diameter of 22 mm. The reactor had a porous quartz plate placed 370 mm from the bottom, and the temperature was measured 5 mm under and 25 mm above this plate, using Pentronic CrAl/NiAl thermocouples enclosed in inconel-600 alloys, inside quartz shells. The pressure drop over the bed was measured by Honeywell pressure transducers at a frequency of 20 Hz. From the pressure fluctuations obtained, it was possible to establish if the particles defluidized during the experiment, and if so, at what point the defluidization occurred.

The bed material of size 125-180 µm was placed on the porous plate and heated in an electric oven while being exposed to an inert atmosphere of N_2, until reaching a desired reaction temperature of 950ºC. When the experimental temperature was reached, the particles were exposed alternatingly to oxidizing and reducing gases, thus simulating the cyclic conditions of a chemical-looping combustion system. The standard gas concentration used during oxidation was 5% O_2 in N_2. This low O_2 concentration was selected to avoid a large temperature increase, caused by the highly exothermic oxidation reaction. For reduction, 100% CH_4 was used for Ni-based oxygen carriers and synthesis gas containing 50% CO and 50% H_2 was used for Fe-based oxygen carriers. CH_4 was used since it is the major constituent of natural gas, and simplifies the experimental evaluation compared to using natural gas. The synthesis gas concentration was chosen to resemble the gas formed by steam gasification of a solid fuel, as presented in reaction (3). The experiments for the reactivity study of a Ni-based oxygen carrier in Paper V were conducted with 50% H_2O in the reducing gas to avoid defluidization. Further details on those experiments are presented in Paper V. To avoid mixing of oxidizing and reducing

gases during the transition, inert N_2 was introduced for 180 s after each period in all experiments.

The standard bed mass used during reactivity experiments was 15 g and most experiments with Ni-based oxygen carriers were conducted with 15 g of active material. However, some Ni-based materials were also investigated using a 1 g active bed mass mixed in inert quartz, still with a total bed mass of 15 g, and one material was investigated with a bed mass of 3 g. These small active bed masses were used in order to obtain an incomplete fuel conversion and thereby provide the possibility to calculate an oxygen carrier reactivity, which was not limited by the amount of incoming methane. Further, a few experiments with Ni-based oxygen carriers were conducted with higher bed masses of up to 40 g to study fluidization behaviour. In these cases, the reduction flow was increased in order to keep the ratio of the bed mass to reduction flow constant.

All experiments with Fe-based oxygen carriers were conducted with the standard bed mass of 15 g. However, the active oxygen carriers were diluted with inert quartz to obtain an incomplete fuel conversion and thereby enable comparison of different materials. Here, the mass-fraction of oxygen carriers in the bed was 20 or 40%.

The inlet CH_4 and N_2 flows with Ni-based oxygen carriers were varied between 450 mL_N/min and 1200 mL_N/min during reduction and inert periods with most experiments conducted at the lower flow. The flow during the oxidizing period was kept constant at 1000 mL_N/min for Ni-based oxygen carriers. A reduction flow of 450 mL_N/min corresponds to 2.5-8.7u_{mf}, where u_{mf} is the minimum fluidization velocity, i.e., the gas velocity at which the oxygen carriers would start to fluidize theoretically [32]. An oxidation flow of 1000 mL_N/min corresponds to 8.1-28u_{mf}. The experiments with Fe-based oxygen carriers were conducted with an inlet flow of 900 mL_N/min for all periods. This flow corresponds to 5.9–7.9u_{mf} for the reduction period and 8.5–11.3u_{mf} for the oxidation period, for the synthetically produced materials. All flows were normalized to 1 bar and 0ºC.

All oxygen carriers were tested for several reduction and oxidation periods and normally, the time in reduction was gradually increased until full oxygen carrier conversion was reached or until defluidization occurred. The time under oxidizing conditions was adjusted to give complete oxygen carrier oxidation.

The gas from the reactor was led to an electric cooler, where the water produced in the reduction was condensed and removed, and then on to a Rosemount NGA-2000 gas analyzer where the concentrations of CO_2, CO, CH_4 and O_2 as well as the flow were measured. During the experiments with Fe-based oxygen carriers, an updated version of

the analyzer with the ability to measure the concentration of H_2 was used. The experimental set-up of the reactivity analysis equipment is presented in Figure 3-1.

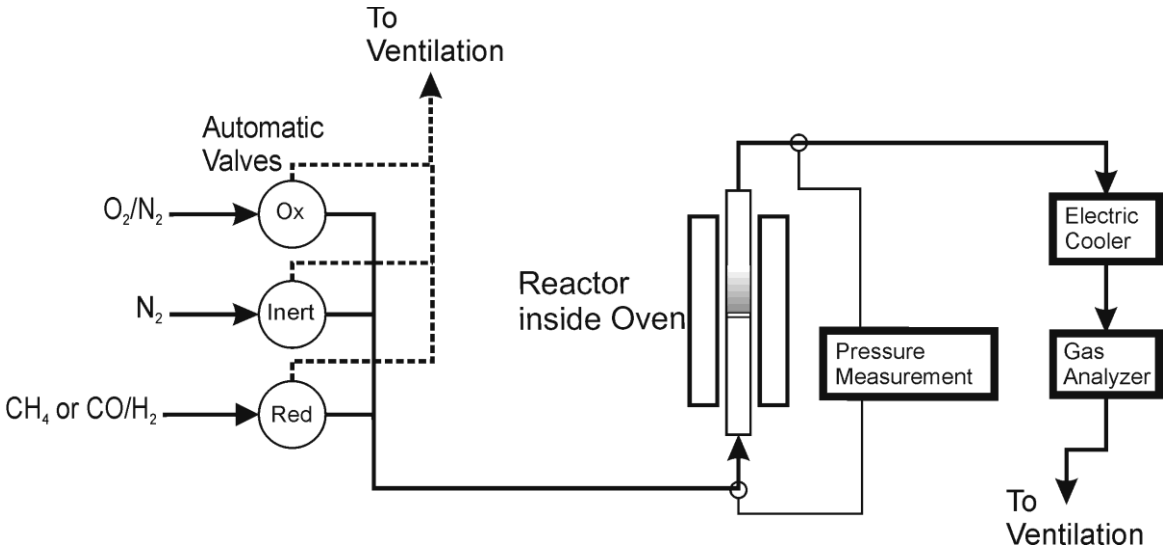

Figure 3-1. Schematic arrangement of the experimental set-up.

The basic set-up for the solid fuel experiments in Paper VII was similar to the set-up of the gaseous fuel experiments. However, the shape of the reactor, the amount of oxygen carriers, the feed of fuel, the temperature and the gas flows used during the experiments were different. Further details of these experiments are presented in Paper VII.

Examples of the outlet gas concentrations, after water condensation and removal, for a reduction and an oxidation period are presented for a Ni-based oxygen carrier in Figure 3-2 and for an Fe-based oxygen carrier in Figure 3-3.

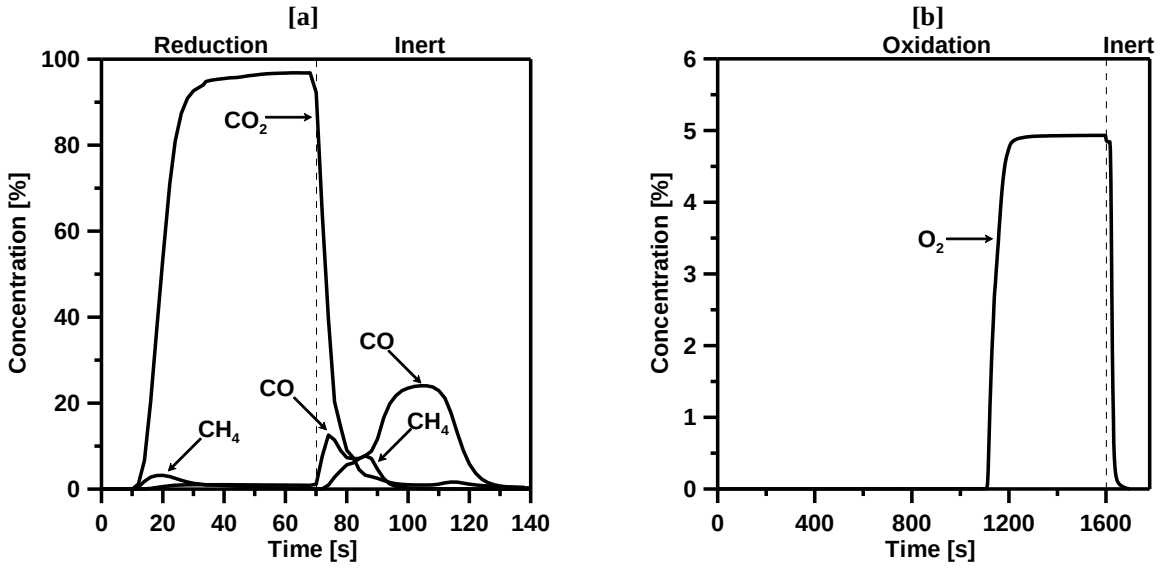

Figure 3-2. Outlet gas concentrations during [a] reducing and [b] oxidizing conditions with 15 g of NOV1T1400. Vertical dashed lines indicate the end of the reacting period and transition to inert gas.

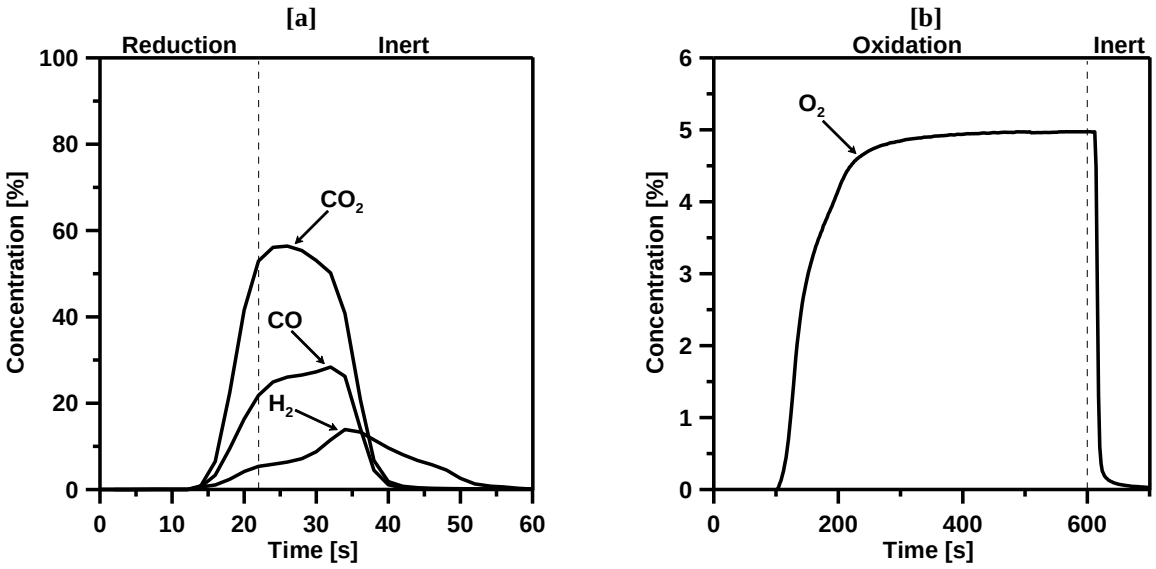

Figure 3-3. Outlet gas concentrations during [a] reducing and [b] oxidizing conditions with 3 g of Sandvik 2. Vertical dashed lines indicate the end of the reacting period and transition to inert gas.

A peak of unconverted methane appears early in the reduction period for Ni-based oxygen carriers, but disappears as the oxygen in the particles is gradually consumed. This can be explained by the formation of metallic Ni-sites on the surface, which acts as catalyst for converting methane through steam reforming:

$$CH_4 + H_2O \leftrightarrow CO + 3H_2 \tag{15}$$

and/or through methane pyrolysis:

$$CH_4 \leftrightarrow C + 2H_2 \tag{16}$$

The thermodynamic limitation when using nickel as an oxygen carrier can be seen from the small amount of CO always present during reduction. The CO released from the reactor had two peaks. The first is connected with the decrease of CO_2 and is caused by the lack of oxygen to fully convert the fuel. The second is caused by a solid-solid reaction of carbon formed with some remainders of oxygen in the oxygen carriers and will be discussed in the Carbon Formation section.

For Fe-based oxygen carriers, the incoming CO and H_2 are partially converted to CO_2 and H_2O, as seen in Figure 3-3a. However, as a result of the insufficient oxygen carrier bed mass, there is always unreacted CO and H_2 passing through the bed.

During the oxidations, presented in Figure 3-2b and 3-3b, complete conversion of the incoming O_2 occurs initially. This implies good contact between gas and oxygen carrier and indicates a high oxidation rate, which is limited by the amount of oxygen supplied.

As seen in Figure 3-2a and 3-3a, the retention time between the introduction of reacting gases and detection of product gases in the analyzer is 10-15 s. To obtain a more accurate concentration profile of the gases leaving the reaction zone, where this residence time and back-mixing in the system are considered, a method of deconvolution [90, 99] was used to correct the gas concentrations. Figure 3-4 shows the corrected gas concentrations, for the reduction of a Ni-based oxygen carrier, when dispersion in the system was accounted for. The calculations show that most of the dispersion takes place in the electric cooler after the reactor. Since steam is condensed before reaching the gas analyzer, the H_2O concentration is calculated by estimating equilibrium between the reacting gases in the water-gas shift reaction. The major H_2 peak in the end of the reduction period is not measured in the gas analyzer but estimated to make up a total gas concentration of 100%.

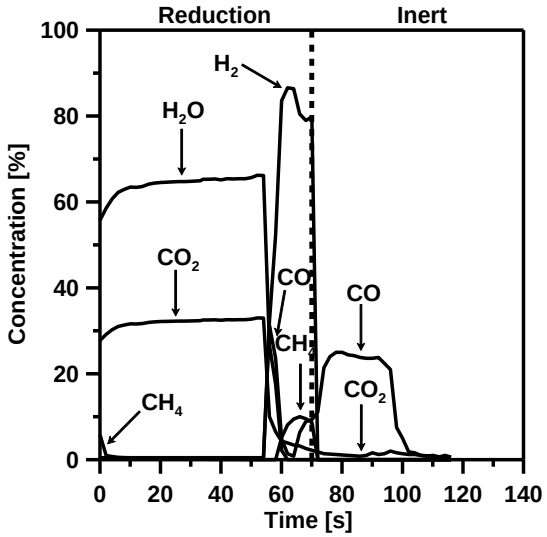

Figure 3-4. Concentration profiles during reduction of NOV1T1400 after correction for dispersion in the system. Vertical dashed lines indicate the end of the reduction period and transition to inert gas.

From the measured outlet gas concentrations, together with flow measurements, the reactivity of the Ni-based particles could be calculated. The degree of oxidation of the oxygen carriers, or the conversion, was defined as:

$$X = \frac{m - m_{red}}{m_{ox} - m_{red}} \tag{17}$$

where m is the actual mass of sample, m_{ox} is the mass of the sample when fully oxidized, and m_{red} the mass of the sample in its fully reduced form. The degree of conversion, during reduction of Ni-based oxygen carriers, was calculated as a function of time, as:

$$X_i = X_{i-1} - \int_{t_0}^{t_1} \frac{1}{n_o P_{tot}} \dot{n}_{out}(4p_{CO_2,out} + 3p_{CO,out} - p_{H_2,out})dt \quad (18)$$

Here, X_i is the conversion as a function of time for period i, X_{i-1} is the conversion after the preceding period, t_0 and t_1 are the times for the start and the finish of the period, n_o is the number of moles of active oxygen in the unreacted oxygen carrier, $\dot{n}_{out}$ is the molar flow of the gas leaving the reactor after water has been condensed and removed, P_{tot} is the total pressure and $p_{i,out}$ is the outlet partial pressure of component i after H_2O removal. As $p_{H_2,out}$ was not measured online in the experiments with Ni-based oxygen carriers, it was assumed to be related to the outlet partial pressure of CO and CO_2 through a relation based on the equilibrium of the gas shift reaction:

$$CO + H_2O \leftrightarrow CO_2 + H_2 \quad (19)$$

In order to enable a comparison of the Fe-based oxygen carriers, which were containing varying amounts of active oxygen, the mass-based conversion, ω, defined in equation (5) was used. The degree of mass-based conversion, with syngas as fuel, was calculated as a function of time as:

$$\omega_i = \omega_{i-1} - \int_{t_0}^{t_1} \frac{M_O}{m_{ox} P_{tot}} \dot{n}_{out}(2p_{CO_2,out} + p_{CO,out} - p_{H_2,out})dt \quad (20)$$

Here, ω_i is the mass-based conversion as a function of time for period i, ω_{i-1} is the mass-based conversion after the preceding period and M_O is the molar mass of oxygen. The degree of conversion or the degree of mass based conversion was also calculated during the oxidation period to verify that the oxygen carriers were completely oxidized.

Gas yields, for the three different fuel gases, were defined in accordance with the gas yields presented in Table 2-1 as:

$$\gamma_{CH_4} = \frac{p_{CO_2,out}}{p_{CH_4,out} + p_{CO_2,out} + p_{CO,out}} \quad (21)$$

$$\gamma_{CO} = \frac{p_{CO_2,out}}{p_{CO_2,out} + p_{CO,out}} \quad (22)$$

$$\gamma_{H_2} = \frac{y_{H_2O,out}}{y_{H_2O,out} + y_{H_2,out}} \tag{23}$$

Here, $y_{i,out}$ is the partial pressure of component *i* in the outgoing gas stream before H_2O condensation. The condensed H_2O is separated in the electric cooler before the gases reach the analyzer, and therefore not measured. However, since the incoming concentrations of H_2 and CO are equal in these tests, equation (23) can be rewritten as:

$$\gamma_{H_2} = 1 - \frac{p_{H_2,out}}{p_{CO_2,out} + p_{CO,out}} \tag{24}$$

To quantify the total conversion of CO for the Fe-based oxygen carriers, the yield for CO during a complete reduction period was defined as:

$$\gamma_{CO,tot} = \frac{\int_{t_0}^{t_1} \dot{n}_{out} p_{CO_2,out} dt}{\int_{t_0}^{t_1} \dot{n}_{out} (p_{CO_2,out} + p_{CO,out}) dt} \tag{25}$$

In order to facilitate comparison of different synthetically produced oxygen carriers with varying fractions of Fe:Ti, an average CO conversion at high degrees of oxygen carrier conversion was introduced. The boundary values of mass-based conversion, ω, were chosen as the gas conversion was fairly high in this interval for all materials tested. The average CO conversion was defined as:

$$\gamma_{CO,avg} = \frac{\int_{\omega=0.99}^{\omega=0.999} p_{CO_2,out} d\omega}{\int_{\omega=0.99}^{X=0.999} (p_{CO_2,out} + p_{CO,out}) d\omega} \tag{26}$$

To quantify the amount of unreacted methane leaving the reactor, when using Ni-based oxygen carriers, a ratio of methane in the outlet gas stream was defined as:

$$fr_{CH_4} = \frac{p_{CH_4,out}}{p_{CH_4,out} + p_{CO_2,out} + p_{CO,out}} \tag{27}$$

To facilitate comparison of different Ni-based oxygen carriers, a Methane index was introduced, defined as the fraction of methane leaving the reactor when *X* was between

0.95 and 0.99. These values of conversion, *X*, were chosen since the initial methane peak appeared somewhere in this interval for all oxygen carriers studied. The Methane index was defined as:

$$CH_{4,index} = \frac{\int_{X=0.95}^{X=0.99} p_{CH_4,out} dX}{\int_{X=0.95}^{X=0.99} (p_{CH_4,out} + p_{CO_2,out} + p_{CO,out}) dX} \quad (28)$$

As is evident from Figure 3-2a and 3-4, the conversion rate of oxygen carrier was limited by the methane supplied for most of the reduction with Ni-based oxygen carriers. However, the fuel conversion was incomplete in the tests with 1 g oxygen carriers diluted in quartz and with 3 g oxygen carriers. Hence, the conversion rate of oxygen carrier was not limited by the amount of CH_4 supplied. Therefore, the experiments with 1 g oxygen carriers were used to determine the reactivity by calculating a Rate index, using the same method as has been described in detail by Cho [100] and Mattisson et al. [101]. The definitions used to calculate the Rate index is also explained in Paper II and III. The Rate index obtained can be used to estimate the needed bed mass in the fuel reactor, also shown in Paper II and III. The experiments with 3 g oxygen carriers were used to obtain kinetic data and to determine the solids inventory in an ideal fuel reactor without gas solid-phase mass transfer limitations, as shown in Paper V.

Carbon formation can be calculated by integrating the total amounts of CO_2 and CO produced during the inert period following a reduction period. The carbon formation ratio, C_{dep}/C_{added}, is the amount of carbon formed during the reduction period over the total amount of carbon introduced during the reduction period and is defined as:

$$\frac{C_{dep}}{C_{added}} = \frac{\int_{t_1}^{t_3} \dot{n}_{out} (p_{CO_2,out} + p_{CO,out}) dt}{\int_{t_0}^{t_3} \dot{n}_{out} (p_{CH_4,out} + p_{CO_2,out} + p_{CO,out}) dt} \quad (29)$$

Here, t_0 is the time when the reduction started, t_1 is when the inert period started, and t_3 is a point of time when no more CO_2 or CO was registered. Because of the time delay caused by gas residence time in the system, t_1 is defined as the point of time in the inert period when no more CH_4 is detected in the outlet flow.

The degree of carbon conversion for solid fuels, as calculated in Paper VII, was defined as:

$$X_C = \frac{m_t}{m_{tot}} \tag{30}$$

where m_t is the mass of carbon converted until time t and m_{tot} is the total mass of carbon converted during the reduction period. To facilitate comparison of the amount of CO and H_2 leaving the reactor during solid fuel experiments, two indices were defined as:

$$CO,_{index} = \frac{\int_{t_{X_C=0.3}}^{t_{X_C=0.7}} \dot{n}_{out} p_{CO,out} dt}{\int_{t_{X_C=0.3}}^{t_{X_C=0.7}} \dot{n}_{out} (p_{CO_2,out} + p_{CO,out} + p_{CH_4,out}) dt} \tag{31}$$

$$H_2,_{index} = \frac{\int_{t_{X_C=0.3}}^{t_{X_C=0.7}} \dot{n}_{out} p_{H_2,out} dt}{\int_{t_{X_C=0.3}}^{t_{X_C=0.7}} \dot{n}_{out} (p_{CO_2,out} + p_{CO,out} + p_{CH_4,out}) dt} \tag{32}$$

where t_{X_C} is the time needed to reach a certain degree of carbon conversion, X_C. The boundary values of the degree of carbon conversion $X_C=0.3$ and $X_C=0.7$ were chosen as the rate of conversion is high and fairly stable in this region.

4

RESULTS

4.1 Characterization of Oxygen Carriers

The X-ray powder diffraction investigation revealed no differences in phase composition between the Ni-based materials sintered at different temperatures and for different times. The NiO raw materials used contain some impurities, although the amounts are too small to be detected by X-ray powder diffraction. As specified by each NiO supplier, most materials contain impurities of primarily Co, Cu, and Fe. The amounts of these are highest for the nickel oxides Novamet Refractory grade and Vogler Brown grade, where the fraction of Co is up to 1.5 wt%, while the fractions of Cu and Fe are somewhat lower.

From the Inductively Coupled Plasma – Optical Emission Spectrometry (ICP-OES) analysis of the iron-based materials presented in Paper VII, it was seen that all materials contained varying fractions of non-iron elements. The oxide scales from Scana and ESAB, the ore from LKAB and the industrial material from Höganäs are fairly pure iron oxides while the oxide scales from Sandvik contain significant amounts of Cr and Ni and the material from Stena Metall contains a wide variety of elements, including Al, Ca, Cu, K, Mg, Na, Si and Zn.

The Scanning Electron Microscopy, SEM, analysis, confirmed that the manufactured particles were spherical and that this sphericity was maintained during the reactivity analysis. A difference noticed between the freeze-granulated and spray-dried oxygen carriers was that some of the spray-dried particles had a hollow interior, as seen in Figure 4-1. This hollow interior was not seen in any particles produced by freeze-granulation and is therefore believed to be a result of the preparation procedure. A difference between the Ni-based oxygen carriers and the synthetically produced ilmenites was the cracks found on the surface of many of synthetically produced ilmenites after the reactivity investigation. Despite these cracks, no particle breakage was observed. Minor cracks were also found on the surface of the natural ilmenites investigated in Paper VI. No such cracks were seen on any Ni-based oxygen carrier, likely as a result of the inert material, which helps maintaining the particle structure during the reactions.

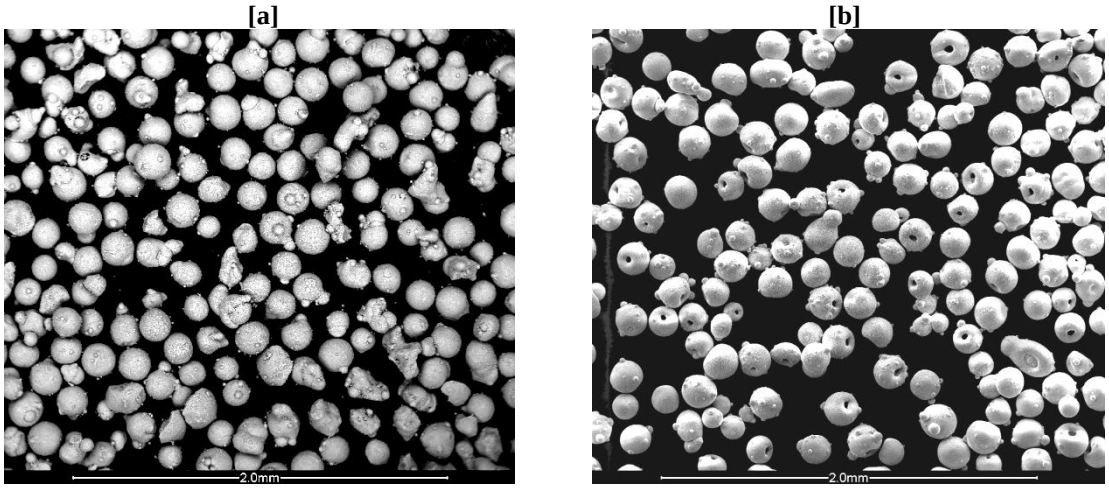

Figure 4-1. SEM-images of [a] freeze-granulated NOV1T1400 and [b] spray-dried NOV1T1400sd prior to reactivity testing. The bar at bottom is 2 mm.

For Fe-based materials, the tested oxygen carriers were generally hard and none of them could be excluded due to low mechanical strength, as displayed in Table 3-4 and 3-8. Natural ilmenites were generally somewhat harder, with a crushing strength of 3.5-4 N, as compared to synthetically produced ilmenites. For synthetically produced ilmenites, the strength generally decreased as the Fe:Ti ratio was increased.

4.1.1 Effect of Sintering Temperature

Figure 4-2a shows the apparent density of the Ni-based oxygen carriers without additives, as a function of sintering temperature. In Figure 4-2b, the crushing strength for the particles that were hard enough to give a distinct value is displayed as a function of sintering temperature.

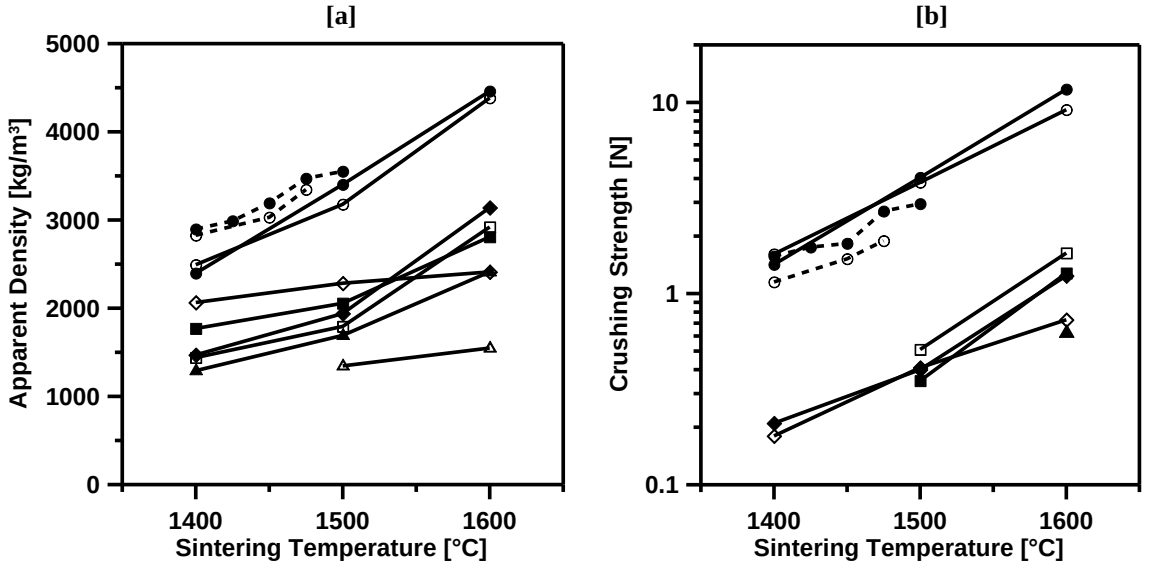

Figure 4-2. [a] apparent density and [b] crushing strength as a function of sintering temperature for NOV1 (●), NOV2 (○), OMG1 (■), OMG3 (□), UMI1 (◆), UMI2 (◇), VOG1 (▲) and VOG2 (△). Dashed line indicates particles prepared by spray-drying.

Both the apparent density and the crushing strength increased with an increased sintering temperature and were highly dependent on the starting material. Particles with low apparent density have generally also low crushing strength and run the risk of fragmentation or attrition, when exposed to circulation in a large-scale unit. As seen, the production method does not seem to affect the physical properties of these particles considerably as the two hardest and densest materials; NOV1 and NOV2, display similar properties when produced by spray-drying as when produced by freeze-granulation.

Ni-based oxygen carriers with a low apparent density and crushing strength, e.g., UMI1T1400, have a more rough surface structure of fine granules while particles with high apparent density and crushing strength, e.g., NOV1T1600, have a smoother surface made up of coarser granules, as displayed in Figure 4-3. Further, the harder and denser particles have generally a lower BET-surface, as seen in Table 3-2.

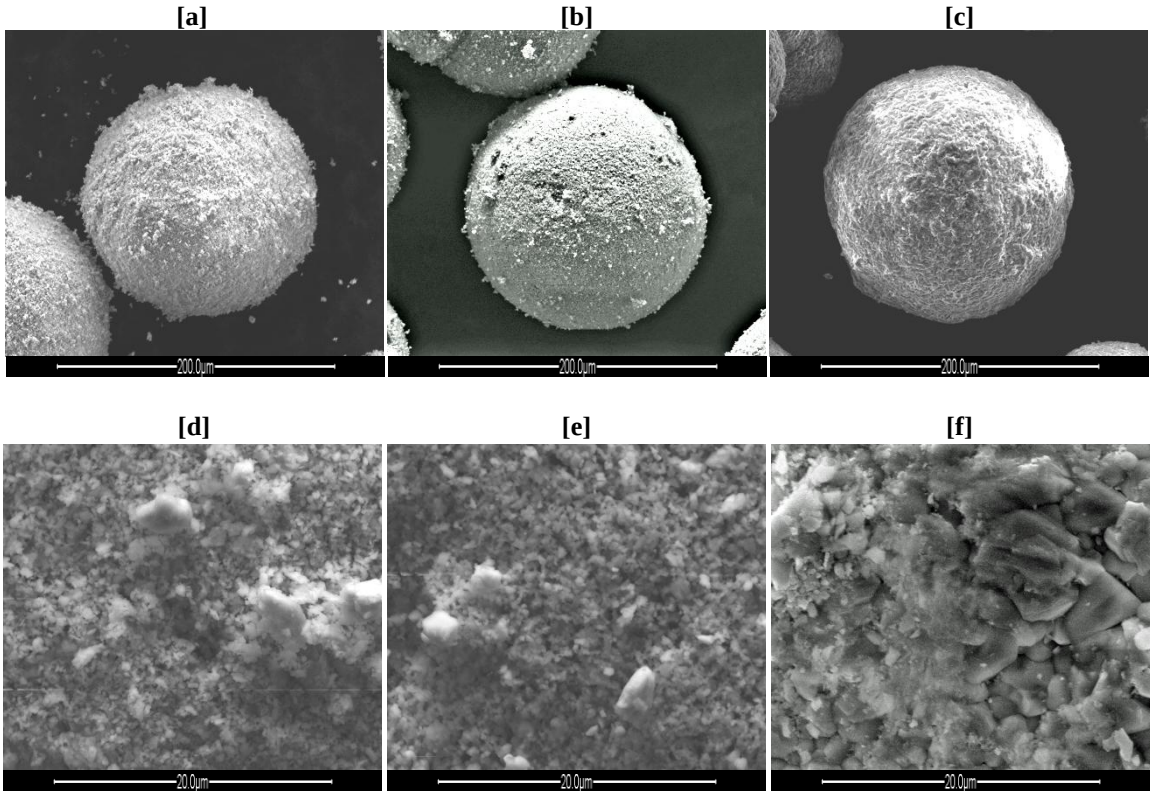

Figure 4-3. SEM-images of particles and their surfaces prior to reactivity testing. [a] and [d] UMI1T1400, [b] and [e] NOV1T1400 and [c] and [f] NOV1T1600. The bar at bottom is 200 µm and 20 µm respectively.

Apart from increasing the sintering temperature, the density and crushing strength of Ni-based oxygen carriers can be increased by an addition of $Ca(OH)_2$ during particle preparation, which is displayed in Figure 4-4. The figure shows the apparent density and crushing strength as a function of sintering temperature for Ni-based particles with additions of $MgAl_2O_4$ or MgO and/or $Ca(OH)_2$.

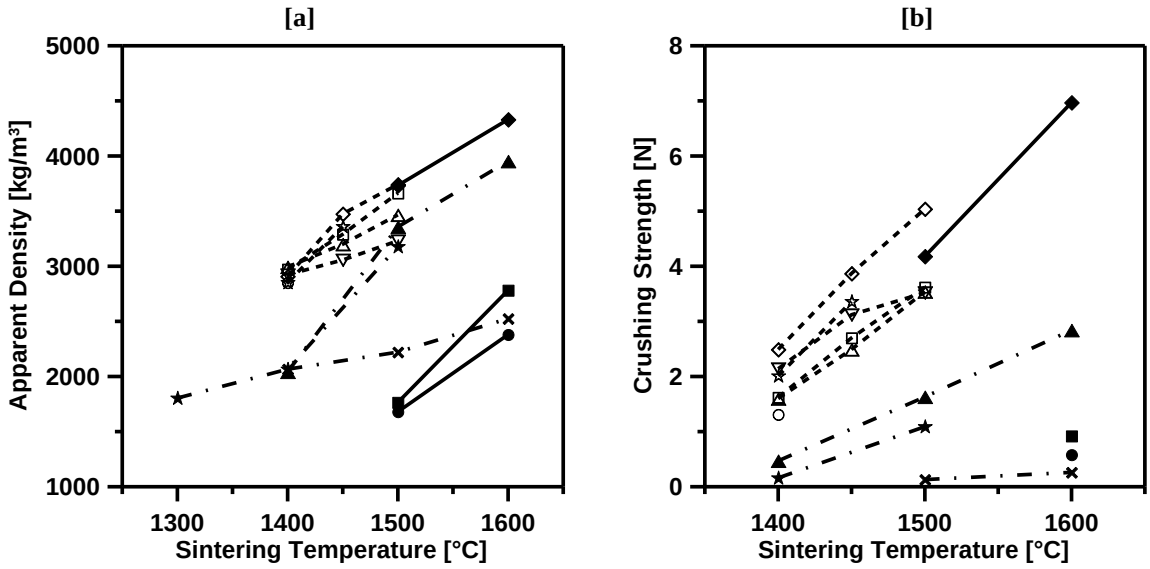

Figure 4-4. [a] apparent density and [b] crushing strength as a function of sintering temperature for OMG5 (●), OMG6 (■), OMG7 (◆), S1 (⋆), S2 (▲), S3 (○), S4 (×), S5 (□), S6 (△), S7 (▽), S8 (◇) and S9 (★). Solid line indicates particles based on OMG HSA grade prepared by freeze-granulation with additives. Dashed line indicates particles based on Novamet Refractory grade prepared by spray-drying with additives. Dashed and dotted line indicates particles based on OMG Standard grade prepared by spray-drying with additives.

OMG5 and OMG6 are prepared with an addition of MgO, see Table 3-3, and display similar physical properties as OMG3 prepared without additives and shown in Figure 4-2. OMG7 is prepared with an addition of $Ca(OH)_2$ and its apparent density and crushing strength is considerably higher than OMG3. The oxygen carriers S1, S3, S5, S6, S7 and S8 are all prepared by spray-drying and based on Novamet Refractory grade, supported by different magnesium-containing support materials, see Table 3-6. These oxygen carriers display similar physical properties as NOV1sd in Figure 4-2, which is produced without additives. The particles S2, S4 and S9 are based on OMG Standard grade and as shown, the strength is highest for S2 and S9, which are prepared with an addition of $Ca(OH)_2$.

4.1.2 Effect of Sintering Time

Harder Ni-based oxygen carriers of higher density can also be obtained by increasing the time period during which they are exposed to high temperatures during sintering, as displayed in Figure 4-5. This result suggests that durable particles can be prepared at moderate sintering temperatures, thus avoiding the need of using ultra high temperature furnaces.

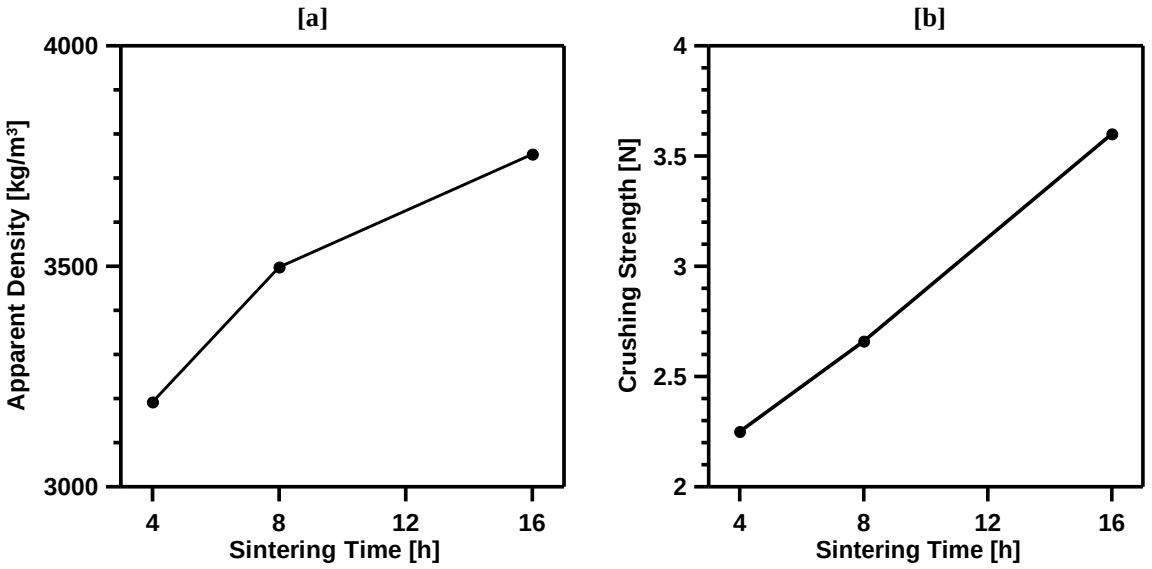

Figure 4-5. [a] apparent density and [b] crushing strength as a function of sintering time for NOV1T1450sd (●).

4.2 Reactivity of Oxygen Carriers

4.2.1 Ni-Based Particles without Additives

Figure 4-6 shows examples of the gas yield and outlet methane fraction as a function of oxygen carrier conversion for some of the materials investigated in the batch fluidized bed reactor. In general, the gas conversion was high for all materials which were fluidizing properly.

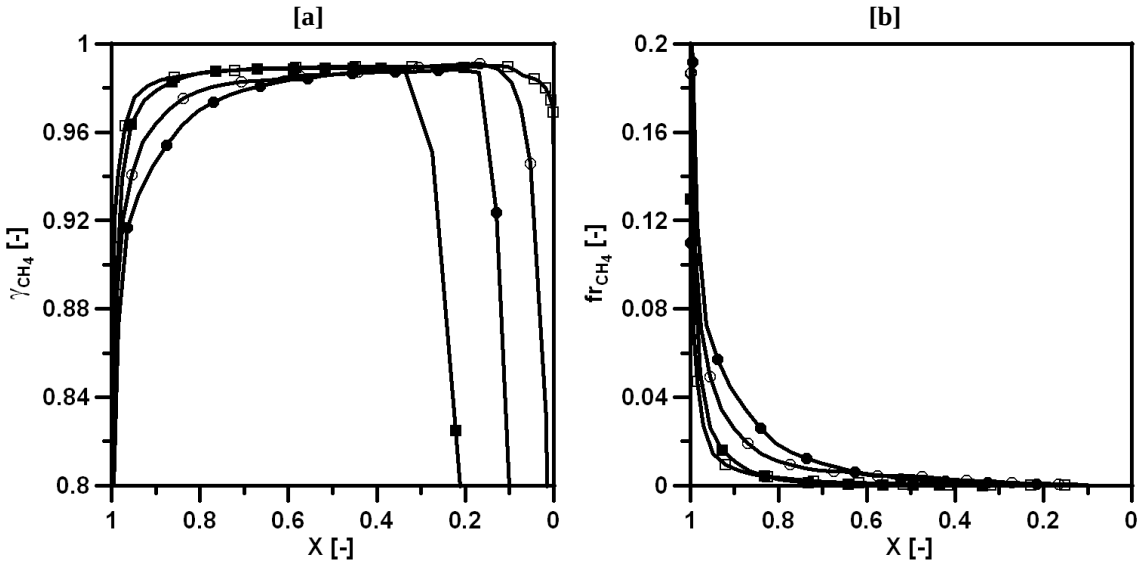

Figure 4-6. [a] gas yield, γ_{CH_4}, and [b] fraction of unreacted CH_4 as a function of the conversion, X, for NOV1T1400sd (●), NOV2T1400sd (■), NOV1T1400 (○) and NOV2T1400 (□).

The main difference seen between the oxygen carriers was the fraction of unreacted CH_4 released early in reduction. This amount was a function of the raw materials used during preparation, but fairly independent of the preparation method, i.e., freeze-granulation or spray-drying, as displayed in Figure 4-6.

During the initial screening of the oxygen carriers prepared by freeze-granulation without additives, ten of the oxygen carriers displayed a high gas conversion in combination with excellent fluidization behaviour. Two of these materials, NOV1T1400 and NOV2T1400, also displayed a high strength. Therefore, focus was set on oxygen carriers based on the same raw materials as NOV1T1400 and NOV2T1400 when the spray-dried oxygen carriers were investigated. Table 4-1 shows the $CH_{4,index}$ for the freeze-granulated and spray-dried oxygen carriers. As seen from the initial screening of freeze-granulated oxygen carriers, the materials based on Vogler NiO have the highest fraction of unconverted CH_4 while materials based on Novamet green grade F and Umicore NiO have the lowest. As shown from the reactivity investigation of the spray-dried oxygen carriers, the fraction of unreacted CH_4 cannot be significantly lowered by changing the sintering temperature. This was true for both the oxygen carriers based on Novamet Refractory grade, NOV1T1400sd-NOV1T11475sd, and for the oxygen carriers based on Novamet Green grade F, NOV2T1400sd-NOV2T1475sd. However, by increasing the sintering time, the fraction of unreacted CH_4 is considerably lowered, as seen by comparing the methane index for NOV1T1450t4sd-NOV1T1450t16sd.

Table 4-1. Methane index for particles without additives.

Freeze-Granulated Oxygen Carriers	*$CH_{4,index}$ (%)*	*Spray-Dried Oxygen Carriers*	*$CH_{4,index}$ (%)*
OMG1T1400	**7.3**	**NOV1T1400sd**	**8.2**
OMG1T1500	**4.6**	**NOV1T1425sd**	**6.9**
OMG3T1400	**3.1**	**NOV1T1450sd**	**10.2**
OMG3T1500	**3.8**	**NOV1T1475sd**	**7.9**
NOV1T1400	**6.4**	**NOV2T400sd**	**4.0**
NOV2T1400	**2.6**	**NOV2T1450sd**	**3.4**
VOG1T1400	**17.8**	**NOV2T1475sd**	**3.3**
VOG1T1500	**8.4**	**NOV1T1450t4sd**	**10.5**
UMI1T1400	**2.8**	**NOV1T1450t8sd**	**7.5**
UMI2T1500	**2.8**	**NOV1T1450t16sd**	**3.9**

4.2.2 Ni-Based Particles with Additives

The main reason for preparing oxygen carriers based on NiO with magnesium-containing support materials was to improve the fuel conversion early in reduction. Generally, the amount of unconverted CH_4 is higher with $NiAl_2O_4$ as support material as compared to with $MgAl_2O_4$ for Ni-based oxygen carriers [72, 85, 87, 102]. The improved fuel conversion, and hence lowered $CH_{4,index}$, when adding MgO during particle

preparation was confirmed in the screening of the freeze-granulated oxygen carriers. Here, the $CH_{4,index}$ for oxygen carriers based on OMG HSA grade was decreased from 3.8% for an oxygen carrier without MgO to 2.8% with an addition of 1 wt% MgO and 0.3% with an addition of 5 wt% MgO as shown in Paper II. The improvement in methane conversion has been explained by an improved dispersion of nickel, which increases the catalytic performance of the oxygen carriers [103].

The fraction of unreacted methane detected in the outlet of the reactor for seven of the oxygen carriers prepared by spray-drying, supported by $MgAl_2O_4$ or with an addition of MgO, is displayed in Figure 4-7. Also included for comparison is NOV1T1450sd which was produced without magnesium. S4 and S9 are not included in the figure since their crushing strength was believed to be too low to withstand fragmentation and attrition in a large-scale application. As is evident, all materials studied displayed a significant improvement in methane conversion when compared to NOV1T1450sd. A quantification of this improvement is displayed in the $CH_{4,index}$ for each oxygen carrier.

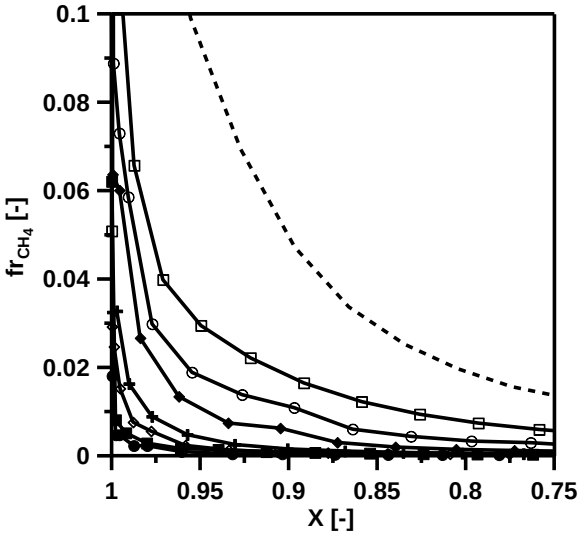

Oxygen Carrier	*$CH_{4,index}$ [%]*
NOV1T1450sd	**10.2**
S5T1400	**3.9**
S3T1400	**2.5**
S6T1400	**1.6**
S1T1400	**0.69**
S2T1500	**0.36**
S8T1400	**0.21**
S7T1400	**0.13**

Figure 4-7. Fraction of unreacted CH_4 as a function of oxygen carrier conversion, X, and $CH_{4,index}$ for NOV1T1450sd (---), S5T1400 (□), S3T1400 (○), S6T1400 (◆), S1T1400 (+), S2T1500 (◇), S8T1400 (■) and S7T1400 (●).

The fraction of unreacted CH_4 was fairly unchanged as a function of reduction cycle for all these materials although the conversion to CO_2 was not, as displayed in Figures 4-8 and 4-9. All materials displayed the same trend of increasing their oxygen carrier conversion span with high gas yield as a function of cycle number. Interestingly, oxygen carriers with a high $CH_{4,index}$ also have a high gas yield for a large oxygen carrier conversion span. In fact, a rank of the oxygen carrier's $CH_{4,index}$ and conversion span with high gas yield follows exactly the same order. However, it should be pointed out that the improved gas yield as a function of cycle number showed no tendencies of slowing down

and therefore even the oxygen carriers with a low $CH_{4,index}$ may give high gas yields at low degrees of oxygen carrier oxidation eventually.

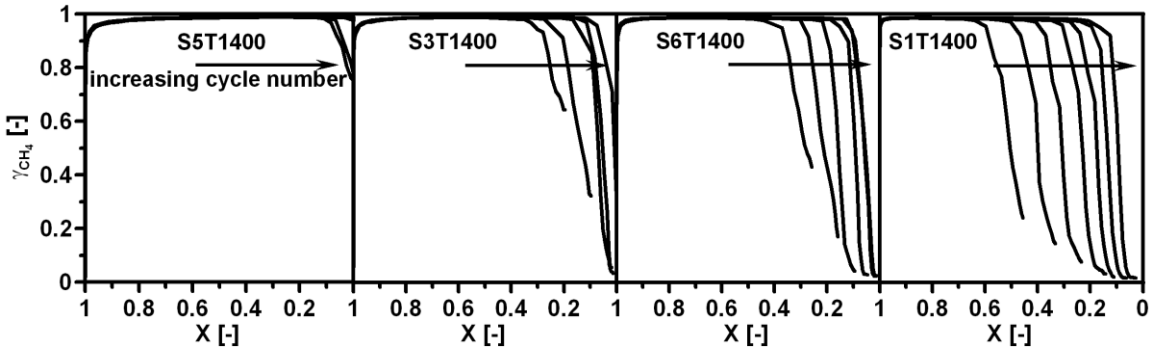

Figure 4-8. Gas yield, γ_{CH_4}, as a function of oxygen carrier conversion, X, for S5T1400, S3T1400, S6T1400 and S1T1400.

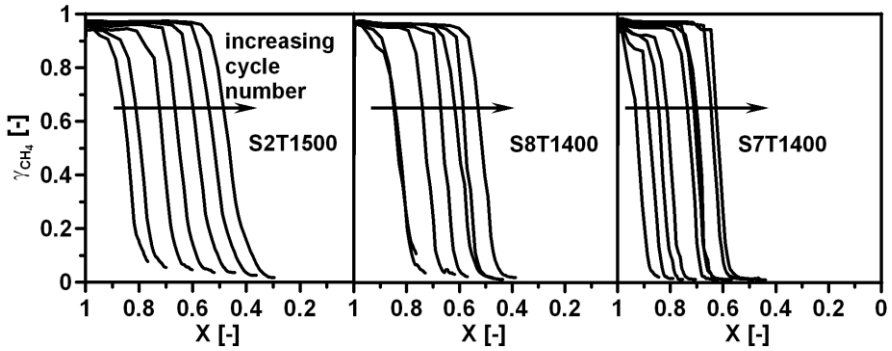

Figure 4-9. Gas yield, γ_{CH_4}, as a function of oxygen carrier conversion, X, for S2T1500, S8T1400 and S7T1400.

4.2.3 Rate Index

The tests with 1 g of Ni-based oxygen carriers diluted in inert quartz resulted in a maximum gas yield of approximately 90-95%. In these experiments, the active material corresponded to only 4 kg/MW fuel. Hence, the reactivity was not restricted by the amount of methane supplied and a reduction rate could be calculated, see Table 4-2.

Table 4-2. Rate index of Ni-based oxygen carrier particles.

Freeze-Gran.	*Rate index [%/min]*	*Freeze-Gran. with MgO*	*Rate index [%/min]*	*Spray-Dried*	*Rate index [%/min]*
OMG1T1400	78	OMG5T1500	84	NOV1T1400sd	75
OMG1T1500	87	OMG6T1500	78	NOV1T1450sd	63
OMG3T1400	74	OMG6T1600	62	NOV2T1400sd	83
OMG3T1500	88			NOV2T1450sd	83
NOV1T1400	72				
NOV2T1400	82				
VOG1T1400	83				
VOG1T1500	84				
UMI1T1400	77				
UMI2T1500	85				

The Rate index is defined as a normalized conversion rate, expressed in terms of percentage mass change per minute [101]. Calculations assume a first-order reaction and

a negligible mass-transfer resistance between the bubble phase and the dense phase in the bed. Details of the calculations are presented in Paper II and III. A comparison using Rate index showed that the reactivity was similar for most materials tested, with a Rate index varying between 62 and 88%/min, as seen in Table 4-2.

4.2.4 Reduction Kinetics with NOV1T1450sd

In Paper V, a more detailed analysis of the reactivity of NOV1T1450sd was conducted and experiments were made at temperatures between 750°C and 950°C using bed masses of 3 g and 30 g, corresponding to 6 and 57 kg/MW. The particles clearly showed high reactivity, with a maximum gas yield between 86% and 93% in the investigated temperature interval using only 6 kg/MW, as displayed in Figure 4-10.

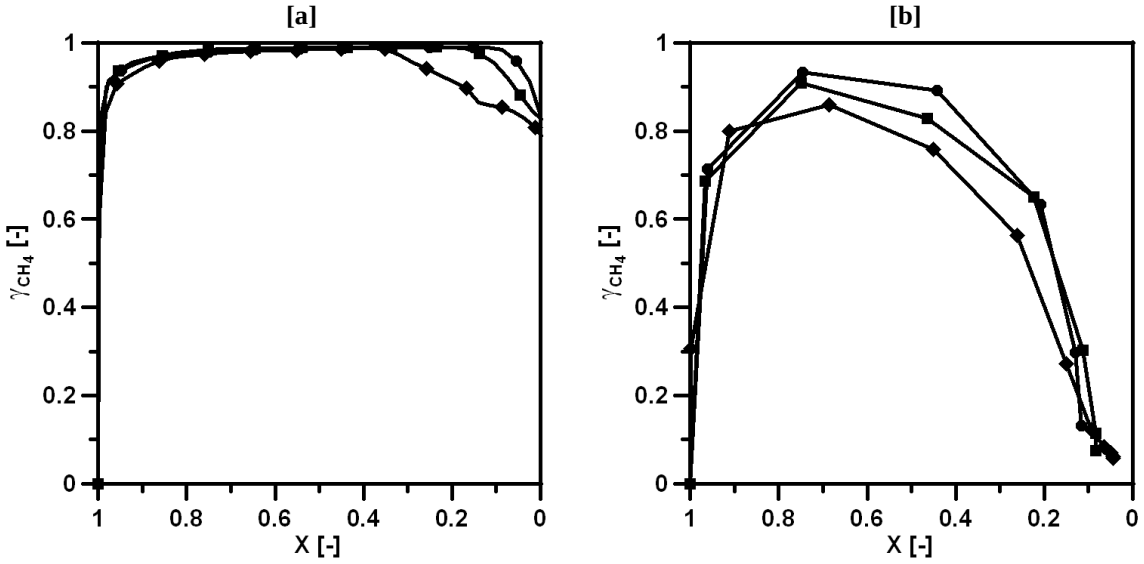

Figure 4-10. Gas yield, γ_{CH_4}, as a function of the conversion, X, for NOV1T1450sd, using a bed mass corresponding to [a] 57 kg/MW and [b] 6 kg/MW at 950ºC (●), 850ºC (■) and 750ºC (◆).

A comparison of the reactivity with data from TGA experiments conducted at CSIC in Zaragoza showed that the reactivity generally was higher in the batch fluidized bed. A simple reactor model using kinetic data from the batch fluidized bed reactor and the TGA was used to predict the mass of oxygen carrier particles necessary for full gas yield of methane to carbon dioxide in the fuel reactor. Results from this study showed that less than 10 kg/MW would be sufficient for complete conversion assuming a 0.6^{th} order of reaction with respect to methane, or 10-20 kg/MW for a reaction order of 1 or using TGA data. Comparison with experiments performed in a 10 and a 120 kW_{th} chemical-looping combustion reactor with the same type of oxygen carrier showed that even when employing 13 to 50 times the amount of oxygen carrier theoretically needed for complete gas conversion, full gas yield was not obtained in the circulating systems.

4.2.5 Natural and Synthetic Ilmenites

For ilmenite particles, the fuel conversion was increased as a function of number of cycles. This increase was clearly seen in the conversion of CO whereas the conversion of H_2 was generally high and stable throughout the experiments. The conversion of H_2 was always higher than the conversion of CO.

Figure 4-11 shows the fuel conversion for three of the synthetically produced materials and the two natural ilmenite minerals, after reaching a fairly stable conversion.

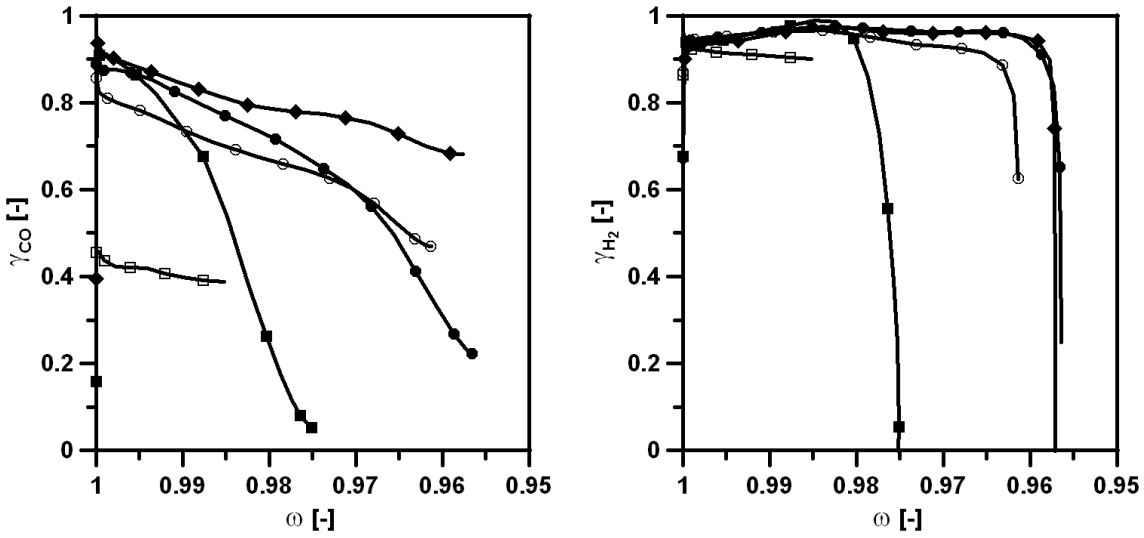

Figure 4-11. [a] gas yield of CO, γ_{CO}, and [b] gas yield of H_2, γ_{H_2}, as a function of mass-based conversion, ω, for sample 1-1 (●), sample 2-5 (■), sample 2-7 (♦), Norwegian ilmenite (○) and South African Ilmenite (□).

As seen in Figure 4-11a, all synthetically produced materials display a high conversion of CO early in the reduction period. However, for the material containing pure Fe_2O_3 (sample 2-7) in its oxidized state, the conversion was maintained fairly high throughout the reduction while the material with a Fe:Ti ratio of 25:75 (sample 2-5) showed a rapidly decreasing conversion of CO. The material containing equal amounts of Fe and Ti (sample 1-1) showed a conversion between these two. The CO conversion of natural Norwegian ilmenite was fairly similar to the synthetically produced ilmenite containing 50% Fe although the initial conversion was somewhat lower. The South African ilmenite agglomerated when the reduction time was increased and the conversion displayed in Figure 4-11 is from a reduction period before this agglomeration occurred. As seen, the CO conversion with the South African ilmenite was poor, as compared to the other materials. As displayed in Figure 4-11b, the conversion of H_2 was high and fairly stable as a function of mass-based oxygen carrier conversion, ω, for all materials. The H_2 conversion with South African ilmenite was somewhat lower, as compared to the other materials.

Figure 4-12 displays the total conversion of CO, as defined in equation 25, and the average conversion of CO at high degrees of oxygen carrier conversion, as defined in equation 26, for all ten synthetically produced materials with varying Fe:Ti ratios. For two of them, agglomerations of the active material were seen in the bed after the experiment, indicated with an A in Figure 4-12. From the total conversion, there seems to be a trend that materials with a higher Fe:Ti ratio display a higher degree of CO conversion. As pure Fe_2O_3 displays the highest total conversion of CO, Fe_2O_3 appears to be more reactive towards CO than Fe_2TiO_5. However, from the average conversion at high degrees of oxygen carrier conversion, no correlation with the Fe:Ti ratio can be observed. The explanation of this is that high conversion of CO is generally maintained for a longer period of time for oxygen carriers containing an excess of Fe, as shown in Figure 4-11.

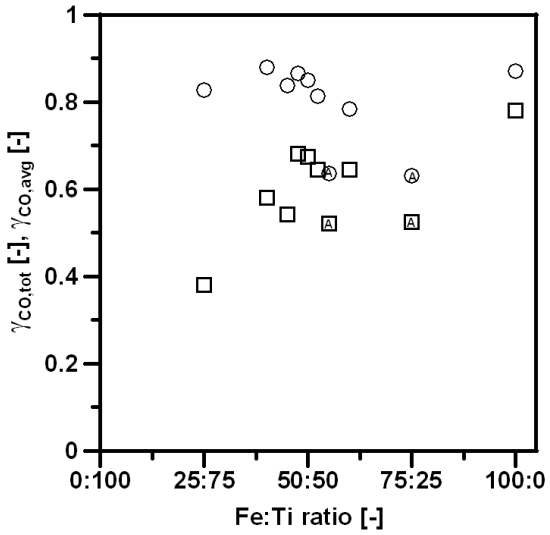

Figure 4-12. Total conversion of CO, $\gamma_{CO,tot}$, (□) and average conversion of CO at high degrees of oxygen carrier conversion, $\gamma_{CO,avg}$, (○), as a function of Fe:Ti ratio. An A inside a symbol indicates particle agglomeration.

4.2.5 Low-Cost Fe-Based Materials

In order to investigate the effect of cycle number, the total conversion of CO, for each reduction, is shown as a function of cycle number for the unprocessed iron-based materials in Figure 4-13. For these tests, the length of the reducing period was chosen to achieve a decrease in the mass-based conversion, ω, of about 1%, i.e., oxygen corresponding to 1% of the total oxygen carrier mass was used to oxidize the fuel. Generally, the conversion of CO increased as a function of cycle number, although the oxide scales from Sandvik showed a decrease. Most materials displayed good fluidization properties with the exception being the material from Höganäs where significant

agglomeration was formed. All of the investigated materials displayed a higher conversion of CO than the reference sample, ilmenite.

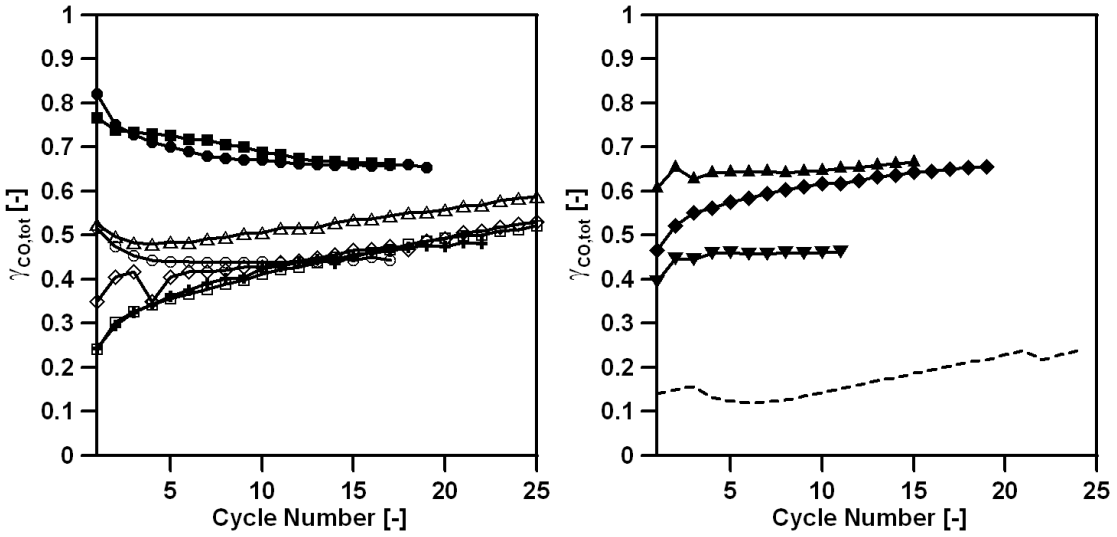

Figure 4-13. Total conversion of CO, $\gamma_{CO,tot}$, as a function of cycle number for Sandvik 1 (●), Sandvik 2 (■), Scana 1 (○), Scana 2 (□), Scana 3 (◇), Scana 8 (△), ESAB (+), LKAB (▲), Höganäs (◆), Stena Metall (▼) and the reference sample, ilmenite (---).

The conversion of H_2 was considerably higher than the conversion of CO. All materials converted between 90 and 96% of the incoming H_2, independent of reduction number. The difference in H_2 conversion between the different oxygen carrier materials was insignificant.

Figure 4-14 shows a comparison of the fuel conversion between three of the iron-based materials selected after an initial screening, and the reference sample, ilmenite. Here, the experiments were performed with longer reduction periods, as compared to the results presented in Figure 4-13, and the results represent a reduction where fairly stable fuel conversion has been reached. The dashed lines represent conversion of H_2 and the solid lines the CO conversion. It should be noted that the amount of active oxygen carrier is lower than in the experiments with natural and synthetically produced ilmenites presented in Figure 4-11, hence the lower fuel conversion in Figure 4-14. As seen, the oxide scale from Sandvik displays the highest conversion of CO and together with the oxide scale from Scana, the highest conversion of H_2. Ilmenite displays the lowest conversion with respect to both these gases. The reason why the oxide scale from Sandvik is the most reactive may be due to higher levels of non-iron metals. As shown in Paper VII, Sandvik 2 contains 8.0 wt% of Ni, 1.0 wt% of Mn and 0.22 wt% of Cu. All these elements have shown high reactivity with syngas in TGA experiments [104, 105].

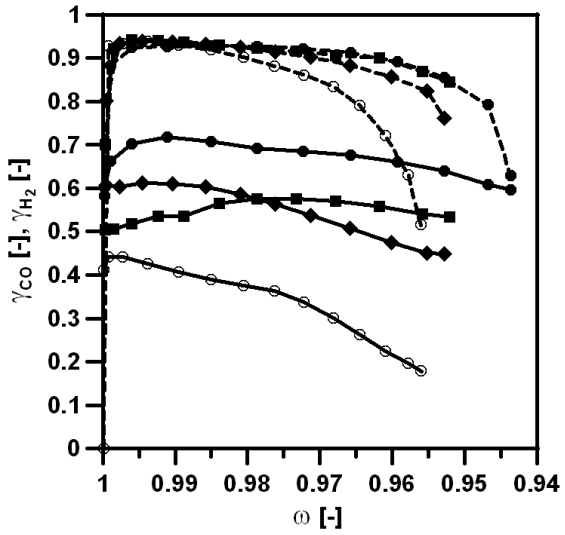

Figure 4-14. gas yield of H_2, γ_{H_2}, dashed lines and gas yield of CO, γ_{CO}, solid lines, as a function of mass-based oxygen carrier conversion, ω, for Sandvik 2 (●), Scana 8 (■), LKAB (◆) and the reference sample, ilmenite (○).

4.3 Effect of Up-Scaling in Particle Production

In order to investigate the effect of up-scaling in particle production of NOV1T1450sd, and to produce Ni-based oxygen carriers to be used in a 10 kW_{th} circulating chemical-looping combustion system, a batch of 30 kg was produced, in contrast to the typical amount of 100-200 g, needed for laboratory testing. When comparing these two batches, it was seen that the gas yield and fraction of unreacted methane was practically identical, thus no difficulties should be expected during scale-up in particle production, as displayed in Figure 4-15.

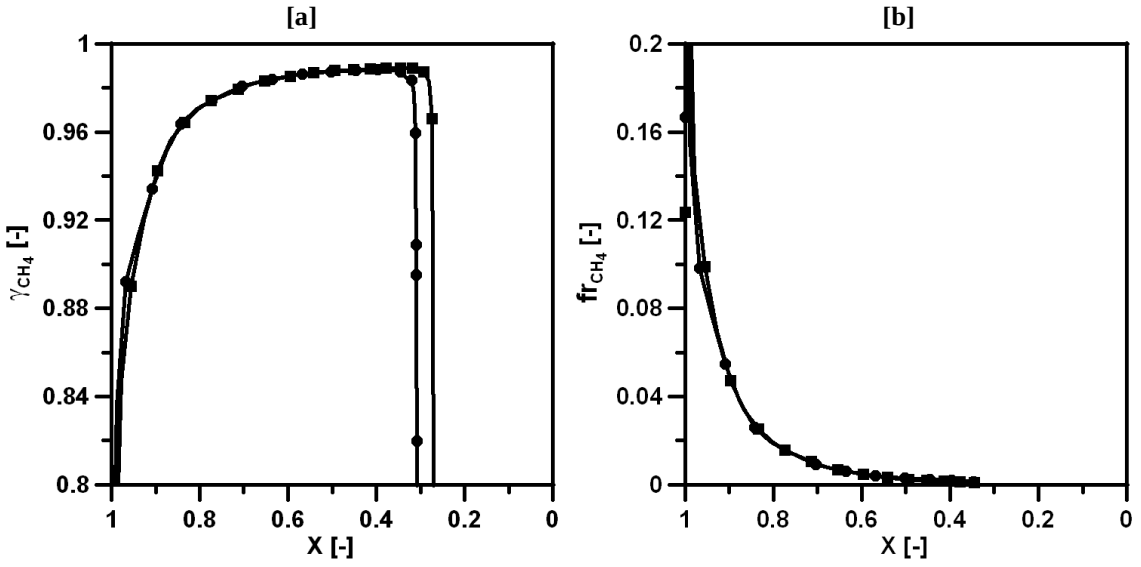

Figure 4-15. [a] gas yield, γ_{CH_4}, and [b] fraction unreacted CH_4, as a function of the conversion, X, for NOV1T1450sd (●) and NOV1T1450m30sd (■).

4.4 Defluidization

During the reactivity testing of the freeze-granulated, Ni-based, oxygen carriers, defluidization sometimes occurred, as indicated in Table 3-2. Defluidization always came about late in a reduction period or early in a subsequent inert period. To avoid this, the inert flow was increased to make fluidization recommence. However, defluidization then reoccurred during one of the subsequent reduction periods or its following inert period until it was permanent.

During the reactivity testing of the spray-dried, Ni-based, oxygen carriers, special focus was placed on investigating the defluidization behaviour. Thus, the reduction time was increased as a function of cycle until the particles defluidized or until complete oxygen carrier conversion was reached. In this manner, the conversion, X, of the oxygen carrier where defluidization occurred could be obtained. The time in reduction for each test performed can be found in Paper III. To study the phenomena of defluidization, the reduction and inert flows were varied in these experiments. However, the oxygen carrier bed mass to fuel flow ratio was kept constant to make the gas conversion comparable between different experiments.

From this investigation, it was clearly seen that the risk of defluidization could be decreased, either by increasing the inlet gas flow or by shortening the time in reduction. In all cases where defluidization occurred, only soft and easily breakable agglomerates were formed and the oxygen carriers remained spherical.

The fact that defluidization only occurred for fully or partially reduced oxygen carriers suggest that the formation of nickel affect the fluidization properties adversely. This was also confirmed by the Energy dispersive X-ray, EDX, analysis, which clearly showed accumulations of pure Ni on the oxygen carrier surface, for highly reduced particles where defluidization had occurred, as displayed in Figure 4-16. It is believed that these accumulations contribute to attaching particles together, thus causing defluidization [82]. Generally, no such accumulations were seen on oxidized particles prior to reactivity testing or on reduced particles after reactivity testing where no defluidization had occurred.

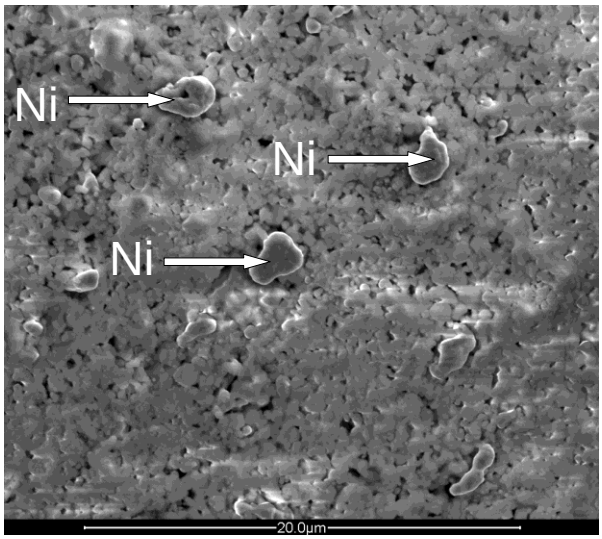

Figure 4-16. SEM-image of NOV1T1450sd, after reactivity testing.

Figure 4-17 shows the gas velocity, expressed as a ratio of incoming methane velocity, *u*, over the minimum fluidization velocity, u_{mf}, i.e., the gas velocity where the oxygen carriers would start to fluidize theoretically, for NOV1 and NOV1sd as a function of the apparent density for a number of tests. In some of the tests, the inlet gas velocity was raised to counteract the decrease in u/u_{mf}, resulting from increasing density. Clearly, this did not help and particles with higher densities also defluidized at higher u/u_{mf}.

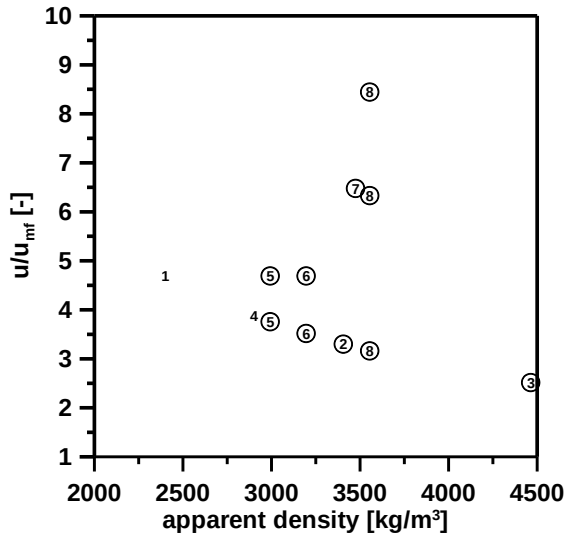

Figure 4-17. Ratio between actual velocity and minimum fluidization velocity as a function of the apparent density. Circle around number indicate defluidization. 1=NOV1T1400, 2=NOV1T1500, 3=NOV1T1600 4=NOV1T1400sd, 5=NOV1T1425sd, 6=NOV1T1450sd, 7=NOV1T1475sd and 8=NOV1T1500sd.

During the reactivity tests with oxygen carriers prepared with Mg-rich additives by spray-drying, displayed in Figure 4-7, no defluidization tendencies occurred for any of the oxygen carriers. In addition, no accumulations of pure Ni were detected on the

surface of these particles. Thus, besides increasing the CH_4 conversion, an addition of MgO also seems to improve the fluidization behaviour.

4.5 Carbon Formation

During the reduction period carbon might form on the oxygen carrier particles, most likely at low gas yields where the availability of oxygen is low [96]. With CH_4 as fuel, carbon formation should not be expected at 950ºC, as long as at least one fourth of the oxygen needed for complete methane conversion is supplied as shown in Figure 2-8a. With CO as fuel, the amount of oxygen needed to avoid carbon formation is only about 1% of the total amount needed for complete conversion of the fuel, at 950ºC and atmospheric pressure, as shown in Figure 2-8b. With Ni-based oxygen carriers, Cho et al. have concluded that formation of solid carbon occurs rapidly when the availability of oxygen is low [96]. However, for Fe-based oxygen carriers the formation of solid carbon appears to be insignificant [96].

These thermodynamic limitations and the previous experimental results agreed well with the present results as carbon formation was clearly seen on Ni-based oxygen carriers, at low degrees of conversion, while no formation of solid carbon was detected on any of the Fe-based oxygen carriers. Figure 4-18a displays the amount of carbon formed on the Ni-based oxygen carriers produced by freeze-granulation, and its correlation with the oxygen carrier conversion.

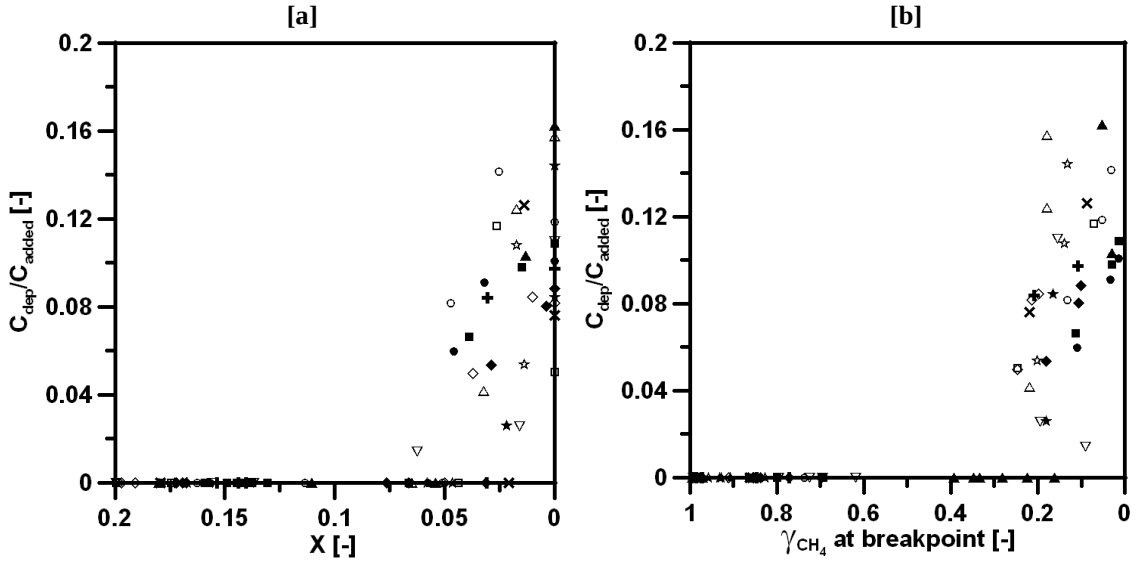

Figure 4-18. Carbon formation ratio, C_{dep}/C_{added}, [a] as a function of the conversion, X, and [b] as a function of the gas yield at breakpoint, γ_{CH_4}, i.e., at the end of the reduction period, for OMG1T1400 (●), OMG1T1500 (■), OMG3T1400 (◆), OMG3T1500 (+), NOV1T1400 (○), NOV2T1400 (□), VOG1T1400 (◇), VOG1T1500 (×), UMI1T1400 (⋆), UMI1T1500 (☆), OMG5T1500 (△), OMG6T1500 (▽) and OMG6T1600 (▲).

In general, carbon formation was only detected at low degrees of conversion, where the gas yield was low. As seen in Figure 4-18a, carbon formation was not detected until only about 5% of the oxygen in the particles remained for all materials with small differences seen between the different oxygen carriers. Figure 4-18b shows the carbon formation correlated with the gas phase composition, i.e., the carbon formation ratio as a function of the gas yield at breakpoint, here defined as the fuel conversion in the middle of the transient in the end of a reduction, i.e., where the CH_4 concentration has decreased by 50%. As is evident, the onset of carbon formation is clearly correlated with a very low fuel conversion. This indicates that significant carbon formation only occurs when the particles have lost so much oxygen that they can only achieve poor fuel conversion.

4.6 Conversion of Solid Fuels

Figure 4-19 shows the outlet gas concentration, after steam condensation, as a function of time, for the reduction of Sandvik 2 with El Correjon coal, Mexican petroleum coke and Swedish wood char. Sandvik 2 was chosen for the solid fuel experiments as it was the low-cost iron-based oxygen carrier material with the highest conversion during the gaseous fuel experiments, as shown in Figure 4-14. As seen in Figure 4-19, initial peaks of CH_4, CO and H_2 appeared with all fuels although the amount of CO and H_2 was small when Mexican petroleum coke was used. These initial peaks are associated with the pyrolysis of the fuel and reaction of volatiles with the oxygen carrier particles. The relatively long time needed for complete conversion of the fuel is caused by the slow gasification of the solid fuels, and the subsequent reactions of the intermediate gasification products with the oxygen carrier.

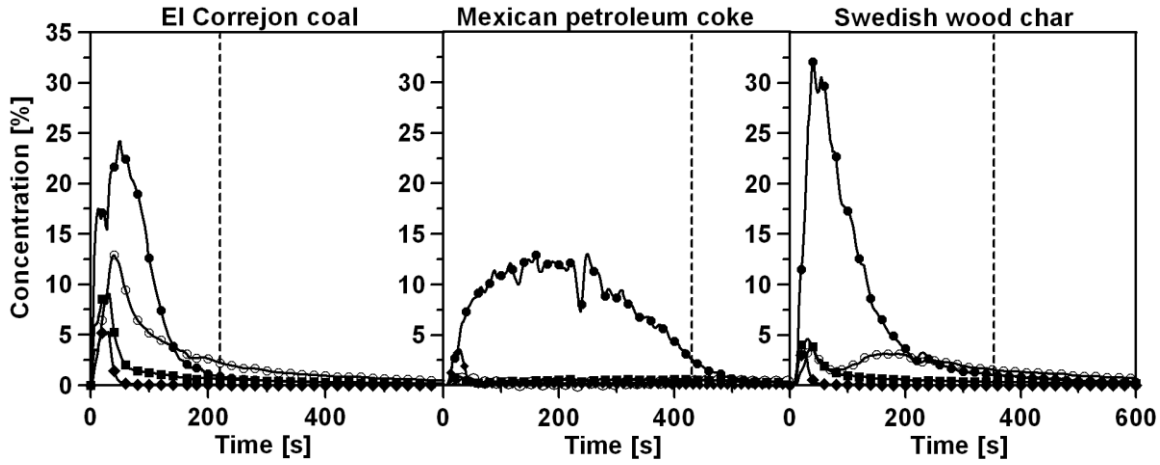

Figure 4-19. Outlet concentrations of CO_2 (●), CO (■), CH_4 (◆) and H_2 (○) during reduction of Sandvik 2 with El Correjon coal, Mexican petroleum coke and Swedish wood char. Vertical dashed lines indicate the time to reach 95% conversion of each solid fuel.

Table 4-3 displays the time needed to convert 95% of each fuel and the CO and H_2 indices, as presented in equation (31) and (32). The conversion time is based on the carbon containing gases detected in the analyzer; hence the losses of fuel during injection are not included. The values with ilmenite as oxygen carrier are obtained from Leion et al. [107] and included for comparison. However, as these experiments were performed without on-line H_2 measurements and only with Mexican Petroleum coke and Swedish wood char as fuel, results from experiments by Azimi with El Correjon coal and for calculating the $H_{2,index}$ for Swedish wood char have also been included [108].

Table 4-3. Time to reach 95% fuel conversion and CO and H_2 indices for El Correjon coal, Mexican petroleum coke and Swedish wood char with Sandvik 2 and Ilmenite as oxygen carriers.

	Sandvik 2			***Ilmenite***		
	Time to convert 95% of the fuel [min]	***$CO_{,index}$ [%]***	***$H_{2,index}$ [%]***	***Time to convert 95% of the fuel [min]***	***$CO_{,index}$ [%]***	***$H_{2,index}$ [%]***
El Correjon coal	**3.7**	**14**	**39**	**5.9***	**21***	**29***
Mexican petroleum coke	**7.2**	**4.1**	**1.8**	**10.8**	**4.6**	**-**
Swedish wood char	**5.9**	**6.1**	**7.6**	**6.3**	**15**	**20***

*-values calculated from experiments by Azimi [108].

As shown in Table 4-3, the conversion of El correjon coal and Mexican petroleum coke is significantly faster with Sandvik 2 than with ilmenite and the conversion of Swedish wood char is slightly faster with the oxide scale from Sandvik as oxygen carrier. Further, the amount of CO released is lower with Sandvik 2 as compared to with ilmenite as oxygen carrier for all fuels. The amount of H_2 released was higher with Sandvik 2 than with ilmenite as oxygen carrier when El Correjon coal was used as fuel. However, with Swedish wood char, the amount released with ilmenite was significantly higher than the amount released with Sandvik 2. The reason why the $H_{2,index}$ was higher with Sandvik 2 than with ilmenite with El Correjon coal may be attributed to the very high fraction of volatiles in this fuel. As the solid fuel conversion is faster with Sandvik 2, a large fraction of the volatiles are released in the interval where the $H_{2,index}$ is calculated, hence this index may be somewhat misleading for this fuel.

5

DISCUSSION

5.1 Ni-Based Oxygen Carriers

Oxygen carriers for gaseous fuel applications of chemical-looping combustion based on commercially available NiO and α-Al_2O_3 are generally very promising, with high reactivity for most materials independent of the supplier and sintering temperature. The two most promising oxygen carriers from the screening of the freeze-granulated particles were NOV1T1400 and NOV2T1400. These materials displayed excellent fluidization behaviour in combination with comparatively high strength. The other materials with good fluidization behaviour were rather soft, with a crushing strength below 1 N. Hence, these materials may run an increased risk of fragmentation and attrition in a large-scale circulating system. However, the harder particles that defluidized should not be entirely excluded since the higher gas velocities and lower degree of reduction in a large-scale application may improve their fluidization behaviour. Particles of lower strength may also be suitable if a small amount of $Ca(OH)_2$ is added. An addition of $Ca(OH)_2$ during particle preparation will most likely lead to the formation of the spinel $CaAl_2O_4$. However, the amounts of $Ca(OH)_2$ added in the present investigation were too small to confirm the presence of this compound by X-ray analysis, although the assumption of $CaAl_2O_4$ formation was supported by thermodynamic equilibrium calculations. Other ways of improving the strength of the oxygen carriers is to increase the time and/or the temperature during sintering of the particles.

Adding MgO to the raw material in the particle production phase will lead to the formation of the spinel $MgAl_2O_4$. Using $MgAl_2O_4$ as supporting material, for nickel-based oxygen carriers, has been shown to enhance the methane conversion compared to using $NiAl_2O_4$ [85, 87, 102, 109]. This improvement in methane conversion has been explained by the improved dispersion of active nickel, which increases the catalytic performance when CH_4 is partially oxidized to CO and H_2 [72, 103]. The reason why Ni-based oxygen carriers supported by $MgAl_2O_4$ display a lower gas yield at low degrees of oxidation, compared to Ni-based oxygen carriers supported by $NiAl_2O_4$ is not well known. However, it is believed to be caused by a decreased internal transport of oxygen

in the oxygen carriers supported by $MgAl_2O_4$. A decreased internal transport is assumed to give a higher ratio of nickel on the surface of the oxygen carrier and hence an increased catalytic effect in converting CH_4. However, the decreased internal transport seems to limit the conversion to CO_2, which results in major CO formation for these oxygen carriers at low degrees of oxidation. A possibilty may be to use a system of mixed oxides, i.e., a combination of one oxygen carrier which has a good oxygen transport capability and one oxygen carrier with good methane cracking capacity. Linderholm et al. used a combination of NOV1T1450sd and S1T1400, the latter containing MgO, in a continuous 10 kW_{th} chemical-looping combustion reactor, and found that this mixture resulted in higher methane conversion and gas yield in comparison to using only NOV1T1450sd [57]. Shulman et al. concluded that most of these particles maintained their structural integrity and chemical composition, after more than 600 h of operation with the combination of NOV1T1450sd and S1T1400 and more than 1000 h of total operation with NOV1T1450sd in the 10 kW_{th} reactor [109]. The improved fuel conversion, when mixing these oxygen carriers, has also been confirmed in the fluidized bed batch reactor and in a continuous 300 W_{th} reactor system [106].

The Rate index was calculated as a normalized conversion rate, expressed in terms of percentage mass change per minute and based on a few general assumptions. Because the Rate index is not based on detailed kinetics, it should be regarded as an indicative number used to compare different oxygen carriers and to estimate a needed mass of solids and not as a definite value to determine the solids inventory in a chemical-looping combustion unit. The high rate indices obtained here correspond to the mass of solids in the fuel reactor of less than 10 kg/MW, which is consistent with the fact that up to 95% conversion is attained in the 1 g tests, i.e., with a bed mass of 4 kg/MW.

The oxygen carrier NOV1T1450sd showed a gas yield of roughly 80-90% independent of the temperature in most of the solids conversion range and calculations in Paper V show that somewhere between 10-20 kg/MW bed material or less should be sufficient for full yield of methane depending upon reaction order and source of kinetic data, i.e., TGA or fluidized bed. This is similar to the bed masses found when utilizing the Rate index for calculating the necessary bed masses. For the fluidized bed experiments employing a 30 g bed, or 57 kg/MW of the NOV1T1450sd material there is close to complete conversion of the methane for most degrees of solid conversion, as seen in Figure 4-10.

With respect to the 10 kW_{th} circulating reactor, the mass of particles in the fuel reactor is 5 kg, corresponding to 500 kg/MW with a fuel conversion of 96-98%. In the 120 kW_{th} circulating unit in Vienna, a mass corresponding to 133 kg/MW was used in the fuel

reactor, and a gas conversion of 89% was reached. It is obvious that considering kinetics both from the fluidized bed and the TGA, the fuel conversion should be complete for both the 10 kW_{th} and 120 kW_{th} units. The reason for the discrepancy is likely that the gas and solid flows in the circulating units differ considerably from the assumptions used in the model of plug flow and no consideration of mass transfer resistance between the dilute and dense phases of a fluidized bed.

There were clear defluidization tendencies for some materials in the batch reactor, predominantly for oxygen carriers with high density, sintered at high temperatures. Defluidization of the oxygen carriers always came about late in a reduction period or early in a subsequent inert period, when the oxygen carriers were highly reduced, thus the risk of defluidization could be decreased by terminating the reduction period before the oxygen carriers were fully reduced. Kuusik et al. have found that defluidization for NOV1T1450sd is caused by adhesion of particles by bridges containing pure Ni [82], a result which is supported by the findings here. It should be pointed out that although many oxygen carriers defluidized in these experiments, it does not necessarily mean they will defluidize in a large-scale circulating chemical-looping combustion unit. The reason for this is that the gas velocities are higher and the oxygen carrier reduction is never complete in such a unit, since this would cause a major decrease in fuel reactor temperature, as shown in Paper I.

5.2 Fe-Based Oxygen Carriers

Iron-based materials are highly promising for applications of chemical-looping combustion with solid fuels. The main reasons are their low price, rich abundance and low environmental impact.

For Fe-based oxygen carriers, H_2 is converted to a higher degree than CO. This higher reactivity with H_2 at atmospheric pressure has also been observed in TGA experiments at 950°C for Fe-based oxygen carriers [104, 105] and for ilmenite [61].

All iron-based materials displayed an unstable gas conversion as a function of cycle. Generally, the materials were gradually activated as the number of reductions and oxidations increased. This activation is believed to be attributed to a changed surface texture and an increased porosity of the oxygen carriers as they undergo reduction and oxidation reactions. As determined from SEM-images, fresh Fe-based materials are generally comparatively massive, with sharp-edged surfaces for unprocessed particles. However, after reactivity experiments, cracks and a more porous and granular surface structure is generally observed. This is believed to improve the gas-solid contact, and

hence increase the reaction surface. An increase in reactivity, in combination with a change in surface texture, has been reported both for an iron ore [88] and for a natural ilmenite [60]. Adánez et al. have shown that the number of cycles needed to reach stable conversion of ilmenite clearly correlates with the degree of oxygen carrier conversion [61]. With a higher oxygen carrier conversion, a lower number of cycles are needed to activate ilmenite. This explains the higher gas conversion of ilmenite when tested at longer reduction times, as shown in Figure 4-14, as compared to the conversion in Figure 4-13 where the mass-based conversion of ilmenite is significantly lower. The fact that natural minerals and industrial iron-based by-products change in physical properties and reactivity during testing is likely associated with the absence of a supporting material, which is generally used in manufactured oxygen carriers. Therefore, these materials need to be tested during longer times and under circulating conditions to investigate their durability.

When comparing the synthetic ilmenites, it appears as if materials containing more Fe are more capable of converting CO at lower degrees of oxygen carrier conversion. However, the initial conversion seems to be independent of the Fe:Ti ratio. The conversion with the natural Norwegian ilmenite is comparable with the synthetic ilmenites with a similar Fe:Ti ratio. This fact motivates the use of Norwegian ilmenite for further work in chemical-looping combustion utilizing solid fuels. However, ilmenite displayed lower conversion than all unprocessed low-cost Fe-based oxygen carriers which also motivates further efforts in investigating such materials. EDX-analysis indicated that the amount of Fe was significantly higher than the amount of Ti on the surface of the ilmenite particles after reactivity experiments. This phenomenon was clearly seen by Adánez et al. who detected formation of an external shell of free hematite, Fe_2O_3, on ilmenite particles during reactivity experiments and an internal core containing mainly rutile, TiO_2 [61]. Hence, the lower conversion of ilmenite, as compared to materials containing mainly Fe_2O_3/Fe_3O_4, may be attributed to this separation of Fe_2O_3 and TiO_2. The separation decreases the amount of active material as TiO_2 is not contributing to the fuel conversion.

In previous work, it has been shown that gasification of solid fuels with steam is significantly faster in a bed of Fe-based oxygen carriers or ilmenite, as compared to a bed of inert quartz [43]. This is believed to be a result of the fast reaction between the oxygen carrier and the gasification products, mainly CO and H_2. The presence of H_2 during gasification of solid fuels with steam is well known to inhibit the reaction rate [110, 111]. This inhibiting effect of H_2 has also been shown to strongly affect the conversion of char in a laboratory-scale fluidized bed reactor with the presence of oxygen carrier particles

fluidized by steam [112]. Here, the direct inhibiting effect of CO on steam gasification was insignificant. The H_2 inhibition is also believed to explain the faster conversion of solid fuels with the oxide scale Sandvik 2, as compared to ilmenite. Since the conversion of H_2 was found to be higher with the oxide scale, the removal of hydrogen from the bed was more efficient. Therefore, the hydrogen inhibition on the gasification process was decreased and the overall fuel conversion increased.

6

CONCLUSIONS

In order for chemical-looping combustion to be viable for use in a power plant, the oxygen-carrier raw materials need to be accessible at a reasonable cost and the oxygen carriers need to be produced by a method suitable for large-scale production. Thus, one important purpose of this work was to investigate the use of commercially available raw materials and the use of a particle production methodology suitable for large-scale production of Ni-based oxygen carriers. The following points summarize the main findings of the investigation of the resulting Ni-based oxygen carriers:

- Commercially available raw materials can be used to produce high performing oxygen carriers for chemical-looping combustion of gaseous fuels.

- Spray-drying, a method suitable for large-scale oxygen-carrier production, can be used to produce the Ni-based oxygen carriers.

- Up-scaling of the particle production should not present any difficulties.

- To reduce the risk of fragmentation and attrition of the oxygen carriers, the strength can be improved by an addition of $Ca(OH)_2$ during preparation, by increasing the sintering time or by extending the sintering time.

- Using $MgAl_2O_4$ as supporting agent results in a considerably improved fuel conversion for highly oxidized oxygen carriers when compared to using $NiAl_2O_4$. However, oxygen carriers with $MgAl_2O_4$ in the support material display low conversion to CO_2 at low degrees of oxygen carrier oxidation.

- Carbon formation is only detected when the oxygen carriers are highly reduced and the fuel conversion is low. The implication of this is that carbon formation should not be expected in a circulating system, where the fuel conversion is high and the particles are recycled to the air reactor well before they are fully reduced.

- Defluidization is most likely to occur for highly reduced particles, i.e., at conditions not expected in a large-scale application.

- The particles produced have high reactivity, and for an ideal reactor without gas solid-phase mass transfer limitations, full conversion should be reached with a solids inventory in the fuel reactor less than 10-20 kg/MW. In practice, however, much higher inventories would be needed, highly dependent on the fluidization conditions.

When adapting chemical-looping combustion to convert solid fuels, the lifetime of the oxygen carriers is expected to be shorter than with gaseous fuels. Fe-based oxygen carriers are comparatively cheap, abundant and environmentally sound and therefore well suited in solid fuel applications. For this reason a number of low cost ores and by-products or waste materials from industry have been investigated. Moreover, to achieve a better understanding of the low-cost ore ilmenite, $FeTiO_3$, synthetic ilmenite with varying Fe:Ti ratios was produced and studied. The following points summarize the main findings of the study of these Fe-based oxygen carriers:

- Several materials, including an iron-ore and oxide scales from the steel industry, display a high conversion of syngas, the main intermediate when solid fuels are gasified by steam, in combination with a high mechanical strength.

- The syngas conversion with Norwegian ilmenite ore, $FeTiO_3$ in its reduced form, is almost as good as with synthetically produced ilmenite.

- An increased Fe:Ti ratio in synthetically produced ilmenite generally improves the total conversion of CO although the initial maximum conversion is practically unchanged.

- When compared with natural Norwegian ilmenite, all investigated low-cost Fe-based materials display a higher CO conversion and generally also a higher particle strength. Sandvik 2, an oxide scale from the steel industry, displays the highest conversion.

- The conversion rate of solid fuels is higher with Sandvik 2 than with the reference sample, Norwegian ilmenite. A reason is likely the higher conversion of H_2, which reduces the inhibitory effect of H_2 on char gasification.

7

ACKNOWLEDGEMENT

I wish to express my sincere gratitude to my supervisors, Professor Anders Lyngfelt and Associate Professor Tobias Mattisson, for giving me the opportunity to work in a highly interesting field and for all guidance, support and help with understanding and solving both experimental and theoretical problems along the way.

I am very grateful to Professor Oliver Lindqvist for providing me with the opportunity to perform my research at Environmental Inorganic Chemistry.

I am also deeply thankful to all past and present members of the "CLC group", Henrik Leion and Marcus Johansson for helping me out when this was all new to me and for all valuable discussions and Carl Linderholm for excellent collaboration along the way.

A special thank you should also be directed to Muhammad Mufti Azis and all other students choosing to complete their education with us, it has been truly inspiring.

I am also grateful to Roger Sagdahl, Esa Väänänen and Charlotte Bouveng for all help concerning technical and administrative aspects around my research.

Furthermore, I would like to express gratitude to all colleagues at the Division of Environmental Inorganic Chemistry and the Division of Energy Technology for creating a friendly and inspiring working environment.

I would also like to thank the financers of this work, performed in the EU-project "Chemical Looping Combustion CO_2-Ready Gas Power", (CLC Gas Power, EU contract: 019800) and the "Emission free Chemical-Looping Coal Combustion Process" (ECLAIR) project (contract RFCP-CT-2008-00008).

Finally, I wish to thank my family and friends for being there by my side!

8

REFERENCES

1 **Hoffert, M.I., Caldeira, K.** Climate Change and Energy, Overview. *Encyclopedia of Energy*, 2004, **1**, 359-380.

2 **IPCC**. Historical Overview of Climate Change. The Physical Science Basis. Contribution of Working Group I to the Fourth Assessment Report of the Intergovernmental Panel on Climate Change. 2007.

3 **Marriotte, E.** Traite De la Nature des Couleurs. *Ouvres de M. Mariotte, 2nd Ed.*, 1681, **2**.

4 **Fourier, J.** Remarques Générales sur les Températures du Globe Terrestre et des Espaces Planétaires. *Annales de Chemie et de Physique*, 1824, **27**, 136-167.

5 **Weart, S.** The Discovery of Global Warming. *Harvard University Press, Cambridge, MA, 240 pp*, 2003.

6 **Tyndall, J.** On the Absorption and Radiation of Heat by Gases and Vapours, and on the Physical Connection. *Philos. Mag.*, 1861 **22**, 277–302.

7 **Arrhenius, S.** On the Influence of Carbonic Acid in the Air upon the Temperature on the Ground. *Philos. Mag.*, 1896, **41**, 237-276.

8 **IPCC**. Climate Change. *Cambridge University Press*, 2007.

9 **Kiehl, J.T., Trenberth, K.E.** Earth's Annual Global Mean Energy Budget. *Bull. Am. Meteorol. Soc.*, 1997, **78**, 197–208.

10 **IPCC**. Summary for Policymakers. Mitigation. Contribution of Working Group III to the Fourth Assessment Report of the Intergovernmental Panel on Climate Change. 2007.

11 **Petit, J.R., Jouzel, J., Raynaud, D., Barkov, N.I., Barnola, J.M., Basile, I., Bender, M., Chappelaz, J., Davis, M., Delaygne, G., Delmotte, M., Kotlyakov, V.M., Legrand, M., Lipenkov, V.Y., Lorius, C., Pépin, L., Ritz, C., Saltzman, E., Stievenard, M.** Climate and Atmospheric History of the Past 420,000 Years from the Vostok Ice-Core Antarctica. *Nature*, 1999, **399**(6735), 426-436.

12 **IPCC**. Changes in Atmospheric Constituents and in Radiative Forcing. Climate Change: The Physical Science Basis. Contribution of Working Group I to the Fourth Assessment Report of the Intergovernmental Panel on Climate Change. 2007.

13 **U.S. Department of Commerce**, National Oceanic and Atmospheric Administration, Earth System Research Laboratory, Global Monitoring Division.
Available from: www.esrl.noaa.gov/gmd/infodata/faq_cat-3.html, 2008.

14 **IEA**. Key World Energy Statistics. 2006.

15 **Rosenzweig, C., Karoly, D., Vicarelli, M., Neofotis, P., Wu, Q., Cassana, G., Menzel, A., Root, T.L., Estrella, N., Seguin, B., Tryjanowski, P., Liu, C., Rawlins, S., Imeson, A.** Attributing Physical and Biological Impacts to Anthropogenic Climate Change. *Nature*, 2008, **453**(15), 353-357.

16 **Rodhe, R.A.** from data compiled by The NASA Goddard Institute for Space Studies. Available from: www.globalwarmingart.com/wiki/Temperature_Gallery. 2008.

17 **IPCC**. Special Report on Carbon Dioxide Capture and Storage. 2005.

18 **Herzog, H.J., Eliasson, B., Kaarstad, O.** Capturing Greenhouse Gases. *Scientific American*, 2000, **282** (2), 72–79.

19 **Benson, S.M., Surles, T.** Carbon Dioxide Capture and Storage: an Overview with Emphasis on Capture and Storage in Deep Geological Formations. *Proceedings of the IEEE*, 2006, **94**(10), 1795-1805.

20 **Abu-Khader, M.** Recent Progress in CO_2 Capture/Sequestration: A Review. *Energy Sources, Part A: Recovery, Utilization and Environmental Effects*, 2006, **28**(14), 1261-1279.

21 **IEA**. Putting Carbon Back Into the Ground. *International Energy Agency Greenhouse Gas R&D Program*, 2001.

22 **Möllersten, K., Yan, J., Moreira, J.R.** Promising Market Niches for Biomass Energy with CO_2 Removal and Disposal - Opportunities for Energy Supply with Negative CO_2 Emissions. *Biomass and Bioenergy*, 2003, **25**, 273–285.

23 **Azar, C., Lindgren, K., Larson, E., Möllersten, K.** Carbon Capture and Storage from Fossil Fuels and Biomass - Costs and Potential Role in Stabilizing the Atmosphere. *Climatic Change*, 2006, **74**(1-3), 47-79.

24 **Herzog, H., Golomb, D.** Carbon Capture and Storage from Fossil Fuel Use. *Encyclopedia of Energy*, 2004, 277-287.

25 **Lackner, K.S., Wendt, C.H., Butt, D.P., Joyce, E.L., Sharp, D.H.** Carbon Dioxide Disposal in Carbonate Minerals. *Energy*, 1995, **20**(11), 1153-1170.

26 **Smith, A.R., Klosek, J.** A Review of Air Separation Technologies and their Integration with Energy Conversion Processes. *Fuel Process Technology*, 2001, **70**, 115–134.

27 **Ishida, M., Jin, H.** A Novel Chemical-Looping Combustor without NO_x Formation. *Industrial & Engineering Chemistry Research*, 1996, **35**(7), 2469-2472.

28 **Lewis, W.K., Gilliland, E.R.** Production of Pure Carbon Dioxide. *U.S. Patent no: 2665972*, 1954.

29 **Richter, H.J., Knoche, K.F.** Reversibility of Combustion Processes, Efficiency and Costing, Second Law Analysis of Processes. *ACS Symposium Series 235, Washington DC*, 1983, 71-85.

30 **Ishida, M., Jin, H.** A New Advanced Power-Generation System using Chemical-Looping Combustion. *Energy (Oxford, United Kingdom)*, 1994, **19**(4), 415-422.

31 **Lyngfelt, A., Leckner, B., Mattisson, T.** A Fluidized-Bed Combustion Process with Inherent CO_2 Separation; Application of Chemical-Looping Combustion. *Chemical Engineering Science*, 2001, **56**(10), 3101-3113.

32 **Kunii, D., Levenspiel, O.** Fluidization Engineering. *Butterworth-Heinman*, 1991.

33 **Kolbitsch, P., Pröll, T., Bolhar-Nodenkampf, J., Hofbauer, H.** Design of a Chemical Looping Combustor using a Dual Circulating Fluidized Bed Reactor System. *Chemical Engineering & Technology*, 2009, **32**(3), 398-403.

34 **Anheden, M.** Analysis of Gas Turbine Systems for Sustainable Energy Conversion. *PhD Thesis, Royal Institute of Technology, Stockholm, Sweden*, 2000.

35 **Wolf, J.** CO_2 Mitigation in Advanced Power Cycles. *PhD Thesis, Royal Institute of Technology, Stockholm, Sweden*, 2004.

36 **Brandvoll, Ø.** Chemical Looping Combustion: Fuel Conversion with Inherent Carbon Dioxide Capture. *PhD thesis, Norwegian University of Science and Technology, Trondheim, Norway*, 2005.

37 **Naqvi, R.** Analysis of Natural Gas-fired Power Cycles with Chemical Looping Combustion for CO_2 Capture. *PhD thesis, Norwegian University of Science and Technology, Trondheim, Norway*, 2006.

38 **IEA**. Key World Energy Statistics. 2009.

39 **Cao, Y., Cheng, Z., Meng, L., Riley, J.T., Pan, W.-P.** Reduction of Solid Oxygen Carrier (CuO) by Solid Fuel (Coal) in Chemical Looping Combustion. *Preprints of Symposia - American Chemical Society, Division of Fuel Chemistry*, 2005, **50**(1), 99-102.

40 **Dennis, J.S., Scott, S. A., Hayhurst, A. N.** In Situ Gasification of Coal using Steam with Chemical Looping: A Technique for Isolating CO_2 from Burning a Solid Fuel. *Journal of the Energy Institute*, 2006, **79**(3), 187-190.

41 **Mattisson, T., Johansson, M., Lyngfelt, A.** CO_2 Capture from Coal Combustion using Chemical-Looping Combustion - Reactivity investigation of Fe, Ni and Mn based Oxygen Carriers using Syngas. *Clearwater Coal Conference, Clearwater, FL*, 2006.

42 **Mattisson, T., Lyngfelt, A. Leion, H.** Chemical-Looping with Oxygen Uncoupling for Combustion of Solid Fuels. *International Journal of Greenhouse Gas Control*, 2009, **3**(1), 11-19.

43 **Leion, H., Mattisson, T. and Lyngfelt, A.** Solid Fuels in Chemical-Looping Combustion. *International Journal of Greenhouse Gas Control*, 2008, **2**, 180-193.

44 **Berguerand, N., Lyngfelt, A.** The Use of Petroleum Coke as Fuel in a 10 kW_{th} Chemical-Looping Combustor. *International Journal of Greenhouse Gas Control*, 2008, **2**(2), 169-179.

45 **Lyngfelt, A., Johansson, M., Mattisson, T.** Chemical-Looping Combustion - Status of Development. *9th International Conference on Circulating Fluidized Beds May 13 -16, Hamburg, Germany*, 2008.

46 **Mattisson, T., Lyngfelt, A.** Capture of CO_2 using Chemical-Looping Combustion. *First Biennial Meeting of The Scandinavian-Nordic Section of the Combustion Institute, Göteborg, April 18-20*, 2001, 163-168

47 **Adanez, J., de Diego, L.F., Garcia-Labiano, F., Gayan, P., Abad, A., Palacios, J.M.** Selection of Oxygen Carriers for Chemical-Looping Combustion. *Energy & Fuels*, 2004, **18**(2), 371-377.

48 **Ishida, M., Jin, H.** A Novel Combustor Based on Chemical-Looping Reactions and its Reaction Kinetics. *Journal of Chemical Engineering of Japan*, 1994, **27**(3), 296-301.

49 **Johansson, M.** Screening of Oxygen-Carrier Particles based on Iron-, Manganese-, Copper- and Nickel Oxides for use in Chemical-Looping Technologies. *PhD Thesis, Dept. of Chemical and Biological Engineering, Environmental Inorganic Chemistry, Chalmers University of Technology, Göteborg, Sweden*, 2007.

50 **Johansson, E., Mattisson, T., Lyngfelt, A., Thunman, H.** A 300 W Laboratory Reactor System for Chemical-Looping Combustion with Particle Circulation. *Fuel*, 2006, **85**(10-11), 1428-1438.

51 **Lyngfelt, A., Thunman, H.** Construction and 100 h of Operational Experience of a 10-kW Chemical-Looping Combustor. *Carbon Dioxide Capture for Storage in Deep Geologic Formations-Results from the CO_2 Capture Project*. 2005, **1**, 625-645.

52 **de Diego, L.F., Garcia-Labiano, F., Gayan, P., Celaya, J., Palacios, J.M., Adanez, J.** Operation of a 10 kW_{th} Chemical-Looping Combustor during 200h with a CuO-Al_2O_3 Oxygen Carrier. *Fuel*, 2007, **86**(7-8), 1036-1045.

53 **Ryu, H.-J., Jin, G.-T., Bae, D.-H., Yi, C.-K.** Continuous Operation of a 50 kW_{th} Chemical-Looping Combustor: Long-Term Operation with Ni- and Co-Based Oxygen Carrier Particles. *Presented at the 5th China-Korea Joint Workshop on Clean Energy Technology, October 25-28, Qingdao University, China*, 2004, 221-230.

54 **Kolbitsch, P., Pröll, T., Bolhar-Nordenkampf, J. and Hofbauer, H.** Operating Experience with Chemical Looping Combustion in a 120kW Dual Circulating Fluidized Bed (DCFB) Unit. *Energy Procedia*, 2009, **1**(1), 1465-1472.

55 **Berguerand, N. and Lyngfelt, A.** Design and Operation of a 10 kW_{th} Chemical-Looping Combustor for Solid Fuels – Testing with South African Coal. *Fuel*, 2008, **87**(12), 2713-2726.

56 **Shen, L., Wu, J., Xiao, J., Song, Q., Xiao, R.** Chemical-Looping Combustion of Biomass in a 10 kW_{th} Reactor with Iron Oxide as an Oxygen Carrier. *Energy & Fuels*, 2009, **23**(5), 2498-2505.

57 **Linderholm, C., Mattisson, T., Lyngfelt, A.** Long-Term Integrity Testing of Spray-Dried Particles in a 10 kW Chemical-Looping Combustor using Natural Gas as Fuel. *Fuel*, 2009, **88**(11), 2083-2096.

58 **Lyngfelt, A.** Oxygen Carriers for Chemical-Looping Combustion – 4000 h of Operational Experience. *Submitted to Oil & Gas Science and Technology – Revue de l'IFP. To be published in a Special Issue: 1st International Conference on Chemical Looping*, 2010.

59 **Song, Q., Xiao, R., Deng, Z., Zhang, H., Shen, L., Xiao, J., Zhang, M.** Chemical-Looping Combustion of Methane with $CaSO_4$ Oxygen Carrier in a Fixed Bed Reactor. *Energy Conversion and Management*, 2008, **49**(11), 3178-3187.

60 **Leion, H., Lyngfelt, A., Johansson, M., Jerndal, E. and Mattisson, T.** The Use of Ilmenite as an Oxygen Carrier in Chemical-Looping Combustion. *Chemical Engineering Research and Design*, 2008, **86**(9), 1017-1026.

61 **Adanez, J., Cuadrat, A., Abad, A., Gayan, P., de Diego, L.F.** Ilmenite Activation during Consecutive Redox Cycles in Chemical-Looping Combustion. *Energy & Fuels*, 2010, **24**(2), 1402-1413.

62 **Leion, H., Larring, Y., Bakken, E., Bredesen, R., Mattisson, T., Lyngfelt A.** Use of $CaMn_{0.875}Ti_{0.125}O_3$ as Oxygen Carrier in Chemical-Looping with Oxygen Uncoupling. *Energy & Fuels*, 2009, **23**(10), 5276-5283.

63 **Rydén, M., Lyngfelt, A., Mattisson, T.** $CaMn_{0.875}Ti_{0.125}O_3$ as Oxygen Carrier for Chemical-Looping Combustion with Oxygen Uncoupling (CLOU)—Experiments in a Continuously Operating Fluidized-Bed Reactor System. *International Journal of Greenhouse Gas Control*, In Press, Available online 31 August 2010.

64 **Shulman, A., Cleverstam, E., Mattisson, T., Lyngfelt, A.** Manganese/Iron, Manganese/Nickel and Manganese/Silicon Oxides Used in Chemical-Looping With Oxygen Uncoupling (CLOU) for Combustion of Methane. *Energy & Fuels*, 2009, **23**(10), 5269-5275.

65 **Cho, P., Mattisson, T., Lyngfelt, A.** Comparison of Iron-, Nickel-, Copper- and Manganese-Based Oxygen Carriers for Chemical-Looping Combustion. *Fuel*, 2004, **83**(9), 1215-1225.

66 **de Diego, L.F., Gayan, P., Garcia-Labiano, F., Celaya, J., Abad, A., Adanez, J.** Impregnated CuO/Al_2O_3 Oxygen Carriers for Chemical-Looping Combustion: Avoiding Fluidized Bed Agglomeration. *Energy & Fuels*, 2005, **19**(5), 1850-1856.

67 **Adanez, J., Gayan, P., Celaya, J., de Diego, L.F., Garcia-Labiano, F., Abad, A.** Chemical Looping Combustion in a 10 kW_{th} Prototype Using a CuO/Al_2O_3 Oxygen Carrier: Effect of Operating Conditions on Methane Combustion. *Industrial & Engineering Chemistry Research*, 2006, **45**(17), 6075-6080.

68 **Hossain, M.M., de Lasa, H.I.** Chemical-Looping Combustion (CLC) for Inherent CO_2 separation – A Review. *Chemical Engineering Science*, 2008, **63**(18), 4433-4451.

69 **Johansson, M., Mattisson, T. and Lyngfelt, A.** Comparison of Oxygen Carriers for Chemical-Looping Combustion. *Thermal Science*, 2006, **10**(3), 93-107.

70 **Garcia-Labiano, F., De Diego, L.F., Adanez, J., Abad, A. and Gayan, P.** Reduction and Oxidation Kinetics of a Copper-Based Oxygen Carrier Prepared by Impregnation for Chemical-Looping Combustion. *Industrial & Engineering Chemistry Research*, 2004, **43**(26), 8168-8177.

71 **de Diego, L.F., Garcia-Labiano, F., Adanez, J., Gayan, P., Abad, A., Corbella, B.M. and Palacios, J.M.** Development of Cu-Based Oxygen Carriers for Chemical-Looping Combustion. *Fuel*, 2004, **83**(13), 1749-1757.

72 **Villa, R., Cristiani, C., Groppi, G., Lietti, L., Forzatti, P., Cornaro, U. and Rossini, S.** Ni Based Mixed Oxide Materials for CH_4 Oxidation under Redox Cycle Conditions. *Journal Of Molecular Catalysis A: Chemical*, 2003, **204-205**, 637-646.

73 **Ishida, M., Yamamoto, M., Ohba, T.** Experimental Results of Chemical-Looping Combustion with $NiO/NiAl_2O_4$ Particle Circulation at 1200°C. *Energy Conversion and Management*, 2002, **43**(9-12), 1469-1478.

74 **Linderholm, C., Abad, A., Mattisson, T., Lyngfelt, A.** 160 Hours of Chemical-Looping Combustion in a 10 kW Reactor System with a NiO-Based Oxygen Carrier. *International Journal of Greenhouse Gas Control*, 2008, **2**(4), 520-530.

75 **Johansson, M., Mattisson, T., Lyngfelt, A.** Comparison of Oxygen Carriers for Chemical-Looping Combustion of Methane-Rich Fuels. *19th FBC Conference, May 21-24, Vienna*, 2006.

76 **Abad, A., Adanez, J., Garcia-Labiano, F., de Diego, L.F., Gayan, P., Celaya, J.** Mapping of the Range of Operational Conditions for Cu-, Fe-, and Ni-Based Oxygen Carriers in Chemical-Looping Combustion. *Chemical Engineering Science*, 2007, **62**(1-2), 533-549.

77 **Ishida, M., Jin, H., Okamoto, T.** Kinetic Behavior of Solid Particle in Chemical-Looping Combustion: Suppressing Carbon Deposition in Reduction. *Energy & Fuels*, 1998, **12**(2), 223-229.

78 **Jin, H., Okamoto, T., Ishida, M.** Development of a Novel Chemical-Looping Combustion: Synthesis of a Solid Looping Material of $NiO/NiAl_2O_4$. *Industrial & Engineering Chemistry Research*, 1999, **38**(1), 126-132.

79 **Readman, J.E., Olafsen, A., Smith, J.B., Blom, R.** Chemical Looping Combustion Using $NiO/NiAl_2O_4$: Mechanisms and Kinetics of Reduction-Oxidation (Red-Ox) Reactions from In Situ Powder X-ray Diffraction and Thermogravimetry Experiments. *Energy & Fuels*, 2006, **20**(4), 1382-1387.

80 **Jin, H., Ishida, M.** A New Type of Coal Gas Fueled Chemical-Looping Combustion. *Fuel*, 2004, **83**(17-18), 2411-2417.

81 **Johansson, M., Mattisson, T., Lyngfelt, A.** Use of $NiO/NiAl_2O_4$ Particles in a 10 kW Chemical-Looping Combustor. *Industrial & Engineering Chemistry Research*, 2006, **45**(17), 5911-5919.

82 **Kuusik, R., Trikkel, A., Lyngfelt, A., Mattisson, T.** High Temperature Behavior of NiO-Based Oxygen Carriers for Chemical Looping Combustion. *9th International Conference on Greenhouse Gas Control Technologies, Washington D.C., November 16-20*, 2008.

83 **Gayan, P., de Diego, L.F., Garcia-Labiano F., Adanez, J., Abad, A., Dueso C.** Effect of Support on Reactivity and Selectivity of Ni-based Oxygen Carriers for Chemical-Looping Combustion. *Fuel*, 2008, **87**(12), 2641-2650.

84 **Mattisson, T., Johansson, M., Jerndal, E., Lyngfelt, A.** The Reaction of $NiO/NiAl_2O_4$ Particles with Alternating Methane and Oxygen. *Canadian Journal of Chemical Engineering*, 2008, **86**(4), 756-767.

85 **Johansson, M., Mattisson, T., Lyngfelt, A., Abad, A.** Using Continuous and Pulse Experiments to Compare two Promising Nickel-Based Oxygen Carriers for use in Chemical-Looping Technologies. *Fuel*, 2008, **87**(6), 988-1001.

86 **Rydén, M., Lyngfelt, A., Mattisson, T.** Synthesis Gas Generation by Chemical-Looping Reforming in a Continuously Operating Laboratory Reactor. *Fuel*, 2006, **85**(12-13), 1631-1641.

87 **Johansson, E., Mattisson, T., Lyngfelt, A., Thunman, H.** Combustion of Syngas and Natural Gas in a 300 W Chemical-Looping Combustor. *Chemical Engineering Research and Design*, 2006, **84**(A9), 819-827.

88 **Mattisson, T., Lyngfelt, A. and Cho, P.** The Use of Iron Oxide as an Oxygen Carrier in Chemical-Looping Combustion of Methane with Inherent Separation of CO_2. *Fuel*, 2001, **80**(13), 1953-1962.

89 **Xiao, R., Song, Q., Zhang, S., Zheng, W., Yang, Y.** Pressurized Chemical-Looping Combustion of Chinese Bituminous Coal: Cyclic Performance and Characterization of Iron Ore-Based Oxygen Carrier. *Energy & Fuels*, 2010, **24**(2), 1449-1463.

90 **Abad, A., Mattisson, T., Lyngfelt, A., Johansson, M.** The Use of Iron Oxide as Oxygen Carrier in a Chemical-Looping Reactor. *Fuel*, 2007, **86**(7-8), 1021-1035.

91 **Leion, H., Mattisson, T. and Lyngfelt, A.** Use of Ores and Industrial Products As Oxygen Carriers in Chemical-Looping Combustion. *Energy & Fuels*, 2009, **23**(4), 2307-2315.

92 **He, F., Wang, H., Dai, Y.** Application of Fe_2O_3/Al_2O_3 Composite Particles as Oxygen Carrier of Chemical Looping Combustion. *Journal of Natural Gas Chemistry*, 2007, **16**(2), 155-161.

93 **Xiao, R., Song, Q., Song, M., Lu, Z., Zhang, S., Shen, L.** Pressurized Chemical-Looping Combustion of Coal with an Iron Ore-Based Oxygen Carrier. *Combustion and Flame*, 2010, **157**(6), 1140-1153.

94 **Leion, H., Jerndal, E., Steenari, B.-M., Hermansson, S., Israelsson, M., Jansson, E., Johnsson, M., Thunberg, R., Vadenbo, A., Mattisson, T. and Lyngfelt, A.** Solid Fuels in Chemical-Looping Combustion using Oxide Scale and Unprocessed Iron Ore as Oxygen Carriers. *Fuel*, 2009, **88**(10), 1945-1954.

95 **Moldenhauer, P.** Testing of Minerals and Industrial By-Products as Oxygen Carriers for Chemical-Looping Combustion in a 300 W Test Reactor. *MSc Thesis, Chalmers University of Technology, T2009-325*, 2009.

96 **Cho, P., Mattisson, T., Lyngfelt, A.** Carbon Formation on Nickel and Iron Oxide-Containing Oxygen Carriers for Chemical-Looping Combustion. *Industrial & Engineering Chemistry Research*, 2005, **44**(4), 668-676.

97 **Vehring, R., Foss, W.R., Lechuga-Ballesteros, D.** Particle Formation in Spray Drying. *Journal of Aerosol Science*, 2007, **38**(7), 728-746.

98 **Bemrose, C.R., Bridgwater, J.** A Review of Attrition and Attrition Test Methods. *Powder Technology*, 1987, **49**(2), 97-126.

99 **Levenspiel, O.** *Chemical Reaction Engineering*. (New York: John Willey and Sons, 1981).

100 **Cho, P.** Development and Characterisation of Oxygen-Carrier Materials for Chemical-Looping Combustion. *PhD Thesis, Dept. of Chemical and Biological Engineering, Environmental Inorganic Chemistry, Chalmers University of Technology, Göteborg, Sweden*, 2005.

101 **Mattisson, T., Johansson, M., Lyngfelt, A.** Multicycle Reduction and Oxidation of Different Types of Iron Oxide Particles-Application to Chemical-Looping Combustion. *Energy & Fuels*, 2004, **18**(3), 628-637.

102 **Mattisson, T., Johansson, M., Lyngfelt, A.** The Use of NiO as an Oxygen Carrier in Chemical-Looping Combustion. *Fuel*, 2006, **85**(5-6), 736-747.

103 **Qiu, Y.-J., Chen, J.-X., Zhang, J.-Y.** Effects of MgO Promoter on Properties of Ni/Al_2O_3 Catalysts for Partial Oxidation of Methane to Syngas. *Journal of Fuel Chemistry and Technology*, 2006, **34**(4), 450-455.

104 **Mattisson, T., García-Labiano, F., Kronberger, B., Lyngfelt, A., Adánez, J., Hofbauer, H.** Chemical-Looping Combustion using Syngas as Fuel. *International Journal of Greenhouse Gas Control*, 2007, **1**(2), 158-169.

105 **Abad, A., Garcia-Labiano, F., de Diego, L. F., Gayan, P., Adanez, J.** Reduction Kinetics of Cu-, Ni-, and Fe-Based Oxygen Carriers Using Syngas (CO + H2) for Chemical-Looping Combustion. *Energy & Fuels*, 2007, **21**(4), 1853-2843.

106 **Linderholm, C., Jerndal E., Mattisson, T., Lyngfelt, A.** Investigation of Ni-Based Mixed Oxides in a 300 W Chemical-Looping Combustor. *Chemical Engineering Research and Design*, 2010, **88**(5-6), 661-672.

107 **Leion, H., Mattisson, T., Lyngfelt, A.** CO_2 Capture from Direct Combustion of Solid Fuels with Chemical-Looping Combustion. *Proceedings of the 33rd International Technical Conference on Coal Utilization & Fuel Systems*, 2008, **1**, 221-232.

108 **Azimi, G.** Experimental Evaluation and Modelling of Steam Gasification and Hydrogen Inhibition in CLC with Solid Fuel. *MSc Thesis, Chalmers University of Technology*, 2010.

109 **Shulman, A., Linderholm, C., Mattisson, T., Lyngfelt, A.** High Reactivity and Mechanical Durability of $NiO/NiAl_2O_4$ and $NiO/NiAl_2O_4/MgAl_2O_4$ Oxygen Carrier Particles Used for more than 1000 h in a 10 kW CLC Reactor. *Industrial & Engineering Chemistry Research*, 2009, **48**(15), 7400-7405.

110 **Lussier, M.G., Zhang, Z., Miller, D.J.** Characterizing Rate Inhibition in Steam/Hydrogen Gasification via Analysis of Adsorbed Hydrogen. *Carbon*, 1998, **36**(9), 1361-1369.

111 **Huang, Z., Zhang, J., Zhao, Y., Zhang, H., Yue, G., Suda, T., Narukawa, M.** Kinetic Studies of Char Gasification by Steam and CO_2 in the Presence of H_2 and CO. *Fuel Processing Technology*, 2010, **91**(8), 843-847.

112 **Keller, M., Leion, H., Mattisson, T., Lyngfelt A.** Gasification Inhibition in Chemical Looping Combustion with Solid Fuels. *submitted for publication*, 2010.